

C.4



Effects of Test Cell Recirculation on High-Bypass Turbofan Engines During Simulated Altitude Tests

**R. M. Dugas
Sverdrup Technology, Inc.**

PROPERTY OF U.S. AIR FORCE
AEDC TECHNICAL LIBRARY

August 1986

Final Report for Period October 1980 – May 1985

**TECHNICAL REPORTS
FILE COPY**

Approved for public release; distribution unlimited.

**ARNOLD ENGINEERING DEVELOPMENT CENTER
ARNOLD AIR FORCE STATION, TENNESSEE
AIR FORCE SYSTEMS COMMAND
UNITED STATES AIR FORCE**

NOTICES

When U. S. Government drawings, specifications, or other data are used for any purpose other than a definitely related Government procurement operation, the Government thereby incurs no responsibility nor any obligation whatsoever, and the fact that the Government may have formulated, furnished, or in any way supplied the said drawings, specifications, or other data, is not to be regarded by implication or otherwise, or in any manner licensing the holder or any other person or corporation, or conveying any rights or permission to manufacture, use, or sell any patented invention that may in any way be related thereto.

Qualified users may obtain copies of this report from the Defense Technical Information Center.

References to named commercial products in this report are not to be considered in any sense as an endorsement of the product by the United States Air Force or the Government.

This report has been reviewed by the Office of Public Affairs (PA) and is releasable to the National Technical Information Service (NTIS). At NTIS, it will be available to the general public, including foreign nations.

APPROVAL STATEMENT

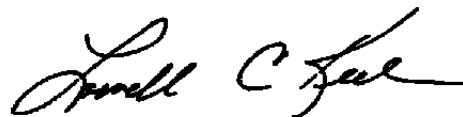
This report has been reviewed and approved.



DAVID A. DUESTERHAUS
Directorate of Technology
Deputy for Operations

Approved for publication:

FOR THE COMMANDER



LOWELL C. KEEL, Lt Colonel, USAF
Director of Technology
Deputy for Operations

UNCLASSIFIED

SECURITY CLASSIFICATION OF THIS PAGE

REPORT DOCUMENTATION PAGE

1a. REPORT SECURITY CLASSIFICATION UNCLASSIFIED		1b. RESTRICTIVE MARKINGS	
2a. SECURITY CLASSIFICATION AUTHORITY		3. DISTRIBUTION/AVAILABILITY OF REPORT	
2b. DECLASSIFICATION/DOWNGRADING SCHEDULE		SEE REVERSE OF THIS PAGE	
4. PERFORMING ORGANIZATION REPORT NUMBER(S) AEDC-TR-85-55		5. MONITORING ORGANIZATION REPORT NUMBER(S)	
6a. NAME OF PERFORMING ORGANIZATION Arnold Engineering Development Center	6b. OFFICE SYMBOL (If applicable) DOT	7a. NAME OF MONITORING ORGANIZATION	
6c. ADDRESS (City, State and ZIP Code) Air Force Systems Command Arnold Air Force Station, TN 37389-5000		7b. ADDRESS (City, State and ZIP Code)	
8a. NAME OF FUNDING/SPONSORING ORGANIZATION Arnold Engineering Development Center	8b. OFFICE SYMBOL (If applicable) DO	9. PROCUREMENT INSTRUMENT IDENTIFICATION NUMBER	
8c. ADDRESS (City, State and ZIP Code) Air Force Systems Command Arnold Air Force Station, TN 37389-5000		10. SOURCE OF FUNDING NOS.	
11. TITLE (Include Security Classification) SEE REVERSE OF THIS PAGE		PROGRAM ELEMENT NO 65807F	PROJECT NO -
		TASK NO. -	WORK UNIT NO -
12. PERSONAL AUTHOR(S) Dugas, R. M., Sverdrup Technology, Inc., AEDC Group			
13a. TYPE OF REPORT Final	13b. TIME COVERED FROM 10/80 TO 5/85	14. DATE OF REPORT (Yr., Mo., Day) August 1986	15. PAGE COUNT 91
16. SUPPLEMENTARY NOTATION Available in Defense Technical Information Center (DTIC)			
17. COSATI CODES		18. SUBJECT TERMS (Continue on reverse if necessary and identify by block number)	
FIELD	GROUP	SUB GR.	
21	05		
		recirculation	
		test cell	
		high-bypass turbofan engine	
		laser velocimeter	
		pressure gradient	
19. ABSTRACT (Continue on reverse if necessary and identify by block number) An experimental and analytical program was conducted to determine the nature of the flow field around a subscale model of a high-bypass turbofan engine installed in a representatively scaled altitude test cell. The engine model employed variable geometry and flow conditions in order to determine their effects on test cell recirculating flows, which can affect engine performance during altitude testing. Flow-field data were obtained from both two-axis laser Doppler velocimeters, as well as from pressure and temperature instrumentation installed on the model and test cell. Review of full- and 1/10-scale test data and the results of AEDC subscale tests indicate that test cell recirculation effects are a function of cell geometry. Measurement of test cell effects is dependent on a baseline test configuration, such as an outdoor test, where the effects are not present.			
20. DISTRIBUTION/AVAILABILITY OF ABSTRACT UNCLASSIFIED/UNLIMITED <input type="checkbox"/> SAME AS RPT <input checked="" type="checkbox"/> DTIC USERS <input type="checkbox"/>		21. ABSTRACT SECURITY CLASSIFICATION UNCLASSIFIED	
22a. NAME OF RESPONSIBLE INDIVIDUAL W. O. Cole		22b. TELEPHONE NUMBER (include Area Code) (615) 454-7813	22c. OFFICE SYMBOL DOS

UNCLASSIFIED

SECURITY CLASSIFICATION OF THIS PAGE

UNCLASSIFIED

SECURITY CLASSIFICATION OF THIS PAGE

3. DISTRIBUTION/AVAILABILITY OF REPORT

Approved for public release; distribution is unlimited.

11. TITLE

Effects of Test Cell Recirculation on High-Bypass Turbofan Engines During Simulated Tests

UNCLASSIFIED

SECURITY CLASSIFICATION OF THIS PAGE

PREFACE

The work reported herein was performed by the Arnold Engineering Development Center (AEDC), Air Force Systems Command (AFSC). The results of the test were obtained by Sverdrup Technology, Inc., AEDC Group, operating contractor for the propulsion test facilities at AEDC, AFSC, Arnold Air Force Station, Tennessee, under Project No. D184EW. The Air Force Project Manager was Mr. D. A. Duesterhaus. The data analysis was completed on September 28, 1984, and the manuscript was submitted for publication on July 5, 1985.

CONTENTS

	<u>Page</u>
1.0 INTRODUCTION	7
2.0 LITERATURE SURVEY	8
3.0 TEST APPARATUS AND PROCEDURES	
3.1 Test Facility	10
3.2 Flow Model	10
3.3 Instrumentation	11
3.4 Laser Velocimetry System	12
3.5 Test Matrix	13
3.6 Test Procedures	14
3.7 Data Systems	14
3.8 Data Uncertainties	16
4.0 TEST RESULTS	17
4.1 Subscale Engine Test Data	18
4.2 Full-Scale Engine Test Data	19
4.3 Subscale Flow Tests at AEDC	22
5.0 CONCLUSIONS AND RECOMMENDATIONS	25
REFERENCES	27

ILLUSTRATIONS

1. Engine/Cell Configuration and Observed Recirculation Patterns	
-CF6-50 Engine Installed in J-2	29
2. Recirculation Model-Expansion Cone Off	30
3. R1A1 Recirculation Model-Expansion Cone On	31
4. R1A1 Laser Velocimetry System and Test Cell	32
5. R1A1 Model Dimensions	33
6. Instrumentation Schematic	34
7. Fringe Orientation and LV Measurement Axis within	
Probe Volume	35
8. 3-Axis Laser Velocimetry Schematic	36
9. Velocity Scatter Plot with Processor "Beating"	37
10. Skewed Histogram	38
11. Typical Turbofan Engine Schematic	39
12. External Static Pressure Distributions-Core Engine Cowl and	
Plug-1/10-Scale TF39	40
13. External Static Pressure Distributions	41

<u>Figure</u>	<u>Page</u>
14. External Pressure Area Force on Primary Nozzle Plug-1/10-Scale-TF39 Exhaust Model-Atmosphere	42
15. External Pressure Area Force on Primary Nozzle Plug-1/10-Scale-TF39 Exhaust Model-J-1	42
16. External Pressure Area Force on Core Engine Cowl-1/10-Scale-TF39 Model-Atmosphere	43
17. External Pressure Area Force on Core Engine Cowl-1/10-Scale-TF39 Model-J-1	43
18. Primary Nozzle Flow Coefficient, C_{FB} versus Fan Nozzle Pressure Ratio, $P_{T2.8}/P_{\infty}$	44
19. Fan Nozzle Flow Coefficient $C_{F2.8}$ versus Fan Nozzle Pressure Ratio, $P_{T2.8}/P_{\infty}$	44
20. TF39 Engine Nacelle Static Pressure Axial Distribution	45
21. TF39 Cell Wall Axial Pressure Gradient Variation	46
22. TF39 Cell Pressure Radial Gradient-Core Nozzle Plane	47
23. TF39 Engine in J-1-Net Cell Wall Axial Static Pressure Variation	48
24. TF39 Thrust Correction for Cell Effects	49
25. CF6-50 Core Nozzle Pressure Profiles	50
26. CF6-50 Core and Fan Cowl Pressure Profiles	51
27. CF6-J-2 Plume Tube Static Pressure Profiles	52
28. CF6-50 Pressure Profile-Altitude to Sea-Level Comparison	53
29. Comparison of Recirculation Induced Net Thrust Corrections for TF39 and CF6-50 Engines at AEDC	54
30. CF6-50 Fan Cowl Net Thrust Correction versus Fan Pressure Ratio	56
31. CF6-50 Core Plug Net Thrust Correction versus Core Nozzle Pressure Ratio	56
32. AEDC Subscale Model-Axisymmetric (No Expansion Cone) Flow-field Velocity Vectors	57
33. AEDC Subscale Model-Axisymmetric Case, $P_t = 10.2$ Flow-field Velocity Vectors	60
34. AEDC Subscale Model-Axisymmetric Case, $P_t = 19.2$, Flow-field Velocity Vectors	67
35. AEDC Subscale Model-Pylon On Case, PTP 10.2 Flow-field Velocity Vectors	73
36. AEDC Subscale Model-Pylon On, Entrance Cone Off, Flow-field Velocity Vectors	80

TABLES

1. Instrumentation	81
a. Summary	81
b. Uncertainties	83
2. Configurations	84
3. Test Conditions	85
4. R1A1 Test Conditions and Configurations	86
APPENDIX	87

1.0 INTRODUCTION

Accurate determination of the performance of high-bypass turbofan engines requires that they be operated in a realistic, controlled environment. For this reason, these engines are typically tested in enclosed test chambers in which engine inflow and altitude conditions can be accurately controlled. This control allows measurement of engine performance characteristics, such as net thrust and fuel consumption. The accuracy of performance measurements is very dependent on the ability of the test chamber (or test cell) to accurately reproduce the flow and altitude conditions the engine is expected to encounter.

Testing of high-bypass turbofan engines in AEDC test cells, and at other test facilities, has been complicated by the presence of recirculating flow regions within the test cell (Fig. 1) that are not present in an unconfined test environment. The recirculating flow regions are the result of a coupled flow process occurring between the fan flow mixing region and the diffuser inlet. The fan flow impinges on the diffuser wall and is partially redirected back into the test cell. The flow is then entrained by the fan flow and evacuated from the test cell. The reflected flow manifests itself within the test cell as a recirculation torus surrounding the engine, with three-dimensional (3-D) variations induced by flow nonuniformities, irregular cell walls, and the engine pylon. The velocity gradients and nonuniformities, in turn, induce axial and radial static pressure gradients within the test cell. The resulting nonuniform static pressure field within the test cell differs significantly from the essentially uniform pressure conditions existing during outdoor tests. The nonuniform static pressure can have undesirable effects on engine performance evaluation. For instance, a recirculation-imposed axial static pressure gradient can alter the fan and core nozzle exit conditions, thus altering the speed match on the fan and core spools. Also, the gradient can change the pressure distribution along the engine surface. Both of these conditions affect the measured engine thrust for a given engine operating condition, because the engine operates at a point different from that of a comparable unconfined environment. Further, pressure field nonuniformities produce an uncertain relationship between measured test cell pressure at a selected station and the equivalent ambient static pressure for operation of the engine outside the closed environment. The net result of these effects is an increase in the uncertainty of measured engine thrust and specific fuel consumption on the order of one percent of measurement.

Past efforts to treat this problem have focused in two areas. One-tenth-scale model flow studies of high-bypass engine exhaust systems are generally performed during engine development to ascertain engine nozzle velocity and flow coefficients. These models have also been operated in altitude test chambers to determine their altitude performance. The effects of recirculation on engine static pressure can then be determined by comparing performance in and out of the test chamber. Attempts have also been made to determine

recirculation effects during full-scale engine tests by placement of static pressure measurement tubes and rings near the plume and cell wall to determine the level of cell pressure gradients and estimate corrections to engine thrust.

The objectives of this study in conjunction with other ongoing efforts at AEDC are threefold:

1. Establish and evaluate the effects of altitude cell flow fields on high-bypass engine performance.
2. Establish a baseline data set of pressure and velocity measurements of the flow field surrounding a subscale model of a turbofan engine exhaust. The data set will be used to validate a 3-D Navier Stokes finite difference model of internal cell flows. This model is currently under development.
3. Establish methods for reducing or correcting for the effects of test cell recirculation on high-bypass turbofan engine performance.

To meet these objectives, an experiment was designed to characterize the flow field around a subscale model of a turbofan engine in an altitude test cell. This subscale model test was conducted in Research Test Cell R1A1 using a specially designed model shown in Fig. 2. The model consists of a flow nozzle discharging through a test volume into a flow diffuser/collector. The nozzle and diffuser are connected and separated by a center pipe. The model has variable geometry and flow capabilities which allow testing of different engine/cell configurations and test conditions.

2.0 LITERATURE SURVEY

The prior work surveyed in this review of test cell recirculation effects can be divided into three categories: (1) ducted coaxial flow mixing, (2) turbofan exhaust system performance, and (3) subscale exhaust nozzle performance testing. Also, work describing the principles and characteristics of laser Doppler velocimetry was surveyed to determine its applicability for this experiment.

Schulz (Ref. 1), Smith and Giel (Ref. 2), and Chriss (Ref. 3) have experimentally and analytically investigated ducted coaxial jet flows with attached recirculation. None of the experiments described used a collector/diffuser but instead allowed the flow to attach to the outer wall so that their results are not directly applicable. However, the features of

recirculation are the same. The mass and energy transport mechanism dissipates primary jet flow energy through the shear layer between the high-speed primary flow and a low-speed coannular secondary flow, which entrains the secondary flow into the primary flow. The long mixing region and its resulting energy dissipation/flow entrainment process couples with the jet and the secondary flow to produce a recirculation mass flow that is balanced by the capacity of the jet to entrain flow.

Kimzey and Rakowski investigated the effects of cell recirculating flows on a full-scale turbofan engine (TF39) undergoing altitude testing at AEDC. They determined that a cell pressure gradient existed and was a function of fan discharge pressure ratio. Comparison of measured thrust levels within the cell to those measured at sea level revealed that the thrust differences between the two conditions were minor. The magnitude of the correction was found to be on the order of 0.02 percent of net thrust at cruise conditions. Further investigation by German and Beach at AEDC indicated that the gradients induced by cell recirculation were more significant than previously thought; that is, they were a function of corrected engine weight flow and radial as well as axial gradients were present. Kimzey determined that the fan nozzle velocity and flow coefficients for the TF39 high-bypass turbofan are a function of fan nozzle pressure ratio and flight condition. Close examination of the flow and velocity coefficient expressions reveals that these coefficients may be affected by flow-induced pressure gradients and by the uncertainty they produce in the measurement of reference cell pressure.

McIlveen and Matkins examined data from an altitude test of CF6-50 at AEDC in March 1981 and found comparable results (unpublished), although the fan nozzle coefficients were not as strong a function of fan nozzle pressure ratio as those determined during TF39 testing. In this test program a different technique was utilized to measure cell pressure gradients. Static pressure measurement pipes or "plume" tubes were placed adjacent to the fan nozzle flow boundary. Significant axial static pressure gradients were measured on the tubes during engine operation. The corrections to net thrust resulting from the measured plume tube gradients were on the order of 0.3 percent to 0.6 percent, which is a significant factor. The static pressure profile measurements made at the cell wall were inconclusive in that no determination of cell gradients could be made because of inadequate number and location of pressure measurements.

General Electric Co. (Ref. 4) and AEDC (Ref. 5) have conducted investigations at Fluidyne, Inc. and AEDC of 1/10-scale turbofan exhaust systems in altitude test cells and have found net thrust decrements on the order of 0.5 percent when installed in an AEDC Propulsion Test Cell J-1 Simulator. The effect was attributed to fan-exhaust-induced cell recirculation.

Inconsistencies in the methods used to describe and correct for test cell recirculation have led to this investigation, which is in line with the objectives previously stated. Flow-field velocity data for a nozzle flowing into a plenum with flow evacuated by a diffuser are nonexistent. Accurate three-axis flow-field velocity data to compare and correct computational model results are not available in the literature. This lack has mandated a requirement for a subscale experiment at AEDC using laser velocimetry to map the flow field around a simulated turbofan exhausting into a test cell.

3.0 TEST APPARATUS AND PROCEDURES

3.1 TEST FACILITY

The test facility used for this series of experiments was Propulsion Research Test Cell R1A1. A schematic of the facility, as it was configured for this series of tests, is shown in Figs. 2 and 3. The basic test cell consists of a 12-ft-long stainless-steel pipe of approximately 5.24 in. internal diameter. The aft end of the test cell is connected to a pumped exhaust header and the cell is suspended off the floor for accessibility. Subsystems for the cell used during these experiments include: high- and low-pressure air supply, hydraulics, optical viewing, instrumentation, and electrical controls.

The primary (high-pressure) and secondary (low-pressure) air supplies are drawn from a high-pressure ($\sim 4,000$ -psia) reservoir, throttled, filtered, and regulated to the required pressure and mass flow, then injected into the upstream end of the model. The facility hydraulics are used to drive and position the model axially in the test cell and to drive the pitot probe. The model (Figs. 2 and 3) is constructed such that it fits inside and moves axially along the internal diameter of the test cell. The optical viewing system consists of a series of four flat optical quality windows on the test cell circumference that surround a 1/4-in.-wide slit in the test cell wall (Fig. 4). A laser Doppler velocimetry (LDV) system is used to focus a three-component set of laser beams through the windows and then through the slit onto a preselected point in space within the test cell known as the probe volume. Flow measurements are made about the model by moving the model axially with the facility hydraulic system until the flow region of interest coincides with the LDV probe volume. Facility instrumentation consists of pressure and temperature channels with suitable signal conditioning, amplification and recording media.

3.2 FLOW MODEL

The flow model is a 43:1 subscale version of the fan exhaust of a General Electric CF6-50 high-bypass turbofan engine. It includes provisions for a pylon, simulated fan nozzle exhaust, expansion cone, and diffuser. The nozzle is connected to the exhaust diffuser by a

centertube as shown in Fig. 2. Air to the model is supplied by a high- and low-pressure supply system and is injected at the forward bulkhead, shown on the left of Fig. 2. The high-pressure or primary air flows into a stilling chamber and then through the primary airflow nozzle into the test volume. The primary nozzle is an ASME flow nozzle with an extended exit section. Low-pressure or secondary air passes through the forward bulkhead around the model and is injected into the test volume through a series of circumferential holes in the nozzle bulkhead. The primary and secondary air is entrained by the primary air and captured by the collector/diffuser. The diffuser ducts the captured air into the facility exhaust header where it is pumped out by exhaust machinery.

The model has capability for variable geometry. The spacing between the nozzle and diffuser can be varied with a screw adjustment mechanism in the center tube assembly which connects the main body of the model to the diffuser and diffuser bulkhead. The center tube fixes the spacing between the model and diffuser and allows the model to be moved axially as a unit within the test cell by the facility hydraulics system. Two diffuser sizes were used. The smaller size was scaled to the diffuser used in the CF6 altitude test of McIlveen and Matkins in J-2. The larger diffuser has a 10-percent larger inlet area. The inlet cone to the diffuser is similar to that used on the CF6/J-2 test and is removable. Two separate nozzle diameters were used. The smaller nozzle was used in axisymmetric tests, and the large nozzle was used when the pylon was installed to compensate for pylon flow blockage effects. The pylon and center plug (Fig. 3) were installed to more accurately simulate the exhaust system of a turbofan. The dimensions of the model are shown in Fig. 5.

3.3 INSTRUMENTATION

Instrumentation was provided to measure model and test facility pressures, temperatures, mass flows, and model and pitot probe position. Table 1a lists the instrumentation used, and Fig. 6 shows the location of each measurement. Pressures were measured with calibrated strain-gage-type pressure transducers with traceability to the National Bureau of Standards. The transducers were also electrically calibrated prior to each test period. Certain parameters were sampled using an AMPS-type scanning valve system, which uses one transducer to scan several pressure taps. In addition, a pitot probe was used to scan the model nozzle flow. The probe was hydraulically driven, and probe position was measured by an electrical potentiohmeter. Total pressure measurements were made immediately behind the LDV probe volume at selected locations along the model. Static pressure measurements were made at the cell wall and on a static pipe on the model centerline. Model and test facility temperatures were measured with iron-constantan thermocouples at the positions shown in Fig. 6. Temperature recording channels were electrically calibrated before every test period.

3.4 LASER VELOCIMETRY SYSTEM

A laser Doppler velocimeter (LDV) system was used to axially and radially scan the flow field from the nozzle exit to the diffuser entrance. The LDV scans were performed by moving the entire nozzle-diffuser assembly fore-to-aft while moving the LDV instrument fixture up and down. The LDV beams were projected through a 1/4-in. sealed slot in the test cell wall, as shown in Fig. 2. Flow-field velocity measurements were made with a three-component Bragg defracted laser Doppler velocimeter (LDV). The optical components of the LDV were mounted on a vertical platform which in turn was mounted on a three-axis hydraulically actuated table. The system surrounds the test cell as shown in Fig. 4. The laser beam is optically separated into three of its constituent colors (488.0, 514.5, and 476.5 nm) and then passed through a series of mirrors and lens which reorient and focus the beams into individual Bragg cells. Bragg cells are water-filled enclosures which use 15-MHz piezoelectric oscillators to set up traveling ultrasonic waves within the cell enclosure. A laser beam is transmitted through the enclosure at near normal incidence to the ultrasonic waves and is diffracted into several nearly equal intensity beams, each at a frequency that varies by an integral order of the Bragg cell frequency. The 0- and 15-MHz frequency-shifted beams are transmitted through an aperture which blocks the unwanted beams. The beams are then transmitted through a series of lens and mirrors and are focused into a point in the flow known as the probe volume. The crossing of the frequency-shifted beam and the unshifted beam at a point in space produces a series of interference fringes similar to that shown in Fig. 7. Further, the frequency shift imparted by the Bragg cells produces fringes that are moving with respect to the probe volume. The crossover of three pairs of beams produces a probe volume in the shape of the intersection of two ellipsoids, with the approximate dimensions shown. By proper placement of the focusing lens, shown in Fig. 8, the 'waist' or narrowest portion of the beam can be made to coincide with the crossover point, hence reducing the size of the crossover region and assuring planar parallel fringes.

Three pairs of interference fringes are generated within the probe volume. The fringe pair associated with $V_{x'}$ and $V_{z'}$ velocity components are oriented as shown in Fig. 8. The $V_{x'}$ and $V_{z'}$ fringes are not aligned with the flow axis but are tilted at 45 deg. Since the dominant velocity is aligned with the X axis or cell centerline and the expected velocities with respect to the vertical or Z axis are small, tilting the $V_{x'}$ and $V_{z'}$ fringes 45 deg permits both the $V_{x'}$ and $V_{z'}$ velocity measurement to be approximately equal. This alignment permits a more accurate measurement of the Z axis velocity, since the $V_{x'}$ and $V_{z'}$ velocities can be resolved to test facility coordinates. The orientation of each velocity is shown in Fig. 7.

A particle passing through the probe volume at some velocity crosses the fringes and scatters light. Particles are injected into the stream with a fluidized bed particle seeder. Nominal one micron diameter aluminum oxide powder was used for seed material. The scattered light from the individual particles is collected and focused into a photomultiplier tube (PMT). The collection lens is located 15 deg off-axis in the forward-scatter mode for both the V_x' and V_z' components to take advantage of high Mie scattering intensities (Ref. 6) at that angle. The cross-component or Y-component collection optics are located at 90 deg off-axis, which is not an optimum angle for viewing based on Mie scattering theory, but was necessitated by model blockage of the beams. The low scattering intensities were compensated for by using the highest power laser line (514.5 nm) for this component.

The light passing through the collector aperture is converted to an electrical signal by the PMT. This signal is amplified and routed to a Teletronix oscilloscope which serves as a 'trigger' for the data processors by allowing only those signals which exceed a preset base voltage rise to be processed. The triggering of the primary oscilloscope generates a signal which is passed to the AEDC Model 8 Doppler Data Processors (DDP) and instructs the DDP's to begin processing the data signal. A detailed description of the Model 8 processors and their operation, as well as the associated data reduction systems is given in Ref. 7.

3.5 TEST MATRIX

The test matrix consists of a selected set of model configurations and flow conditions that were used as the basis of this experiment. The model configurations used for this experiment are summarized in Table 2. They represent an attempt to characterize the effects of geometry on cell recirculation and its resultant effects. As a baseline and for comparative purposes, the primary geometry of the model is scaled from the CF6-50 high-bypass turbofan engine that was tested in AEDC's Propulsion Test Cell J-2. The test flow conditions selected for this set of experiments represent a typical profile of tests used by the CF6 and are summarized in Table 3. The first condition represents a high altitude cruise condition, whereas the second and third represent intermediate power conditions. No other full-scale CF6 test data were available for comparative purposes. The test matrix of flow and geometry conditions tested are shown in Table 4. Configuration numbers 2 through 13 represent tests run with the expansion cone off, referred to as Phase I of this experiment, in an attempt to determine which geometry conditions were most important to recirculation effects. Configuration Numbers 14 through 18 represent geometry and flow conditions that most accurately model full-scale conditions and will be referred to as Phase II. The emphasis of this report will be on the Phase II test configurations.

3.6 TEST PROCEDURES

Test operations for R1A1 began with the selection, buildup, and installation of the required model geometry configuration. Instrumentation calibrations were performed, and reference data points were obtained. The primary exhaust machinery was then brought online and the exhaust header, to which the test cell was connected, was pumped to the required pressure. The proper flow conditions were set in the test cell, and the model was moved to a location in the test cell where the flow region of interest coincided with the cell wall slit. Laser scans of that particular axial position were then made. The laser was moved vertically and horizontally to scan that axial location. On completion of a scan, the model would be moved axially to a new position or rotated about its centerline to scan a different region that was otherwise blocked from view by the model. On completion of a set of scans, new test conditions would be set and scanning continued.

The pretest sequence for the LV began with operational checks of the laser followed by a stabilization period. The system optics were then aligned such that the three probe volumes formed by the three separate components were aligned, as shown in Fig. 7. The point where the model centerline crosses the nozzle exit plane was then optically located and the system position readouts adjusted accordingly. The data acquisition phase was initiated when the flow conditions in the model were stabilized and a sufficient seed rate was obtained from the seeders. After establishment of test conditions, three-axis simultaneous velocity data were obtained with the LV instrumentation.

The pretest sequence for the Technology Data Acquisition and Control System (TDACS) began with a verification of system/facility instrumentation interconnections followed by resistance calibration of all measurement systems. Steady-state data points consisting of multiple high-speed scans of each instrument by the TDACS are obtained and processed to obtain readings of pressure and temperature instruments. During facility operation, steady-state data points were obtained periodically to ascertain that required flow conditions were maintained and to provide a record of facility flow conditions.

3.7 DATA SYSTEMS

3.7.1 Data Acquisition Systems

Two digital data acquisition and recording systems were used to acquire data for this series of experiments. One system was used to acquire and record data from the laser velocimeter and consisted of a minicomputer controlled digital data processor (DDP) for each channel, a digital data tape recorder, and a printer. The minicomputer was linked to

the LV data processors through a control-comparator unit. The other system consisted of a technology data acquisition and control system (TDACS) which acquired, digitized, and transmitted data obtained from pressure and temperature instrumentation during facility test operations.

The LV data acquisition system used a Computer Automation LSI-2 Series minicomputer to act as a buffer storage and logic control unit. The computer was programmed to store 1000 LV Doppler burst samples from each of the DDP's. The data set was then recorded on 8-track magnetic tape, and the results of the statistical checks were printed out.

The measurement for higher order velocity statistics for use in flow-field modeling (that is, turbulence intensities, Reynolds' shear stresses) necessitated simultaneous acquisition of the three components of velocity data. The higher data statistics are described in Ref. 7. To sample random high rate particle throughputs, the data acquisition system must not restrict the data rate. The LSI-2 system is capable of data rates in excess of 1000 three-component samples per second, which permitted acquisition of all data rates encountered during the test.

The TDACS is an automated acquisition system which converts, records, and transmits data from test cell pressure and temperature instrumentation. Analog signals from transducers and thermocouples were converted to digital signals and fed to the system computer. The data were then ready for off-line processing.

3.7.2 Data Reduction

The LDV and facility pressure and temperature test data were reduced using computer codes written for an Amdahl 5640 digital computer. In both cases the final statistical and performance averages were computed by intermediate data handling. The LDV data required broadband filtering to remove noise from the data, whereas the pressure and temperature data had to be averaged over a time period prior to calculation of model and facility performance.

The period data acquired for each of the three laser velocimeter components was recorded on magnetic tape. The data were reduced to velocity data sets for each data point and recorded on tape. Statistical averages were computed from the data thus recorded.

The pressure and temperature data were read from the data tape onto the computer and reduced to engineering units data (EUD) form. After the EUD was manually checked, a program was run to calculate performance parameters that used the EUD as inputs. Plots and printouts of the data could then be obtained.

3.8 DATA UNCERTAINTIES

The uncertainties of the steady-state data obtained during this series of experiments is summarized in Table 1b. The method used to establish the uncertainties of the data is outlined in Abernethy and Thompson (Ref. 8). A number of uncertainties exist in LDV measurements and are subsequently discussed.

A Bragg-diffracted LDV determines the velocity of flow entrained particles by measuring its periodicity, that is, by counting the number of fringe spacings crossed by a particle during a time period. Several system parameters involved in making this measurement, such as fringe spacing, Bragg-diffracted frequency, and measured time period, are subject to experimental error. The error in velocity can be related to errors in the measurement of these parameters measurement by

$$\Delta V_i = V_i \left(\frac{\Delta K}{K} + \frac{\Delta t_i}{t_i} \right) + Kf \left(\frac{\Delta f}{f} + \frac{\Delta t_i}{t_i} \right)$$

where V_i is error in the measurement of an individual velocity, K is the Bragg-diffracted frequency, and t_i is the time period over which the DDP measures the Doppler 'burst' of scattered light (Ref. 7). A Bragg-diffracted system, therefore, includes an error term derived from the frequency shift imparted by the Bragg cell, and this error term is a function of the frequency shift. The magnitude of the errors are then related to the accuracy of the DDP, the Bragg cell oscillator stability, and fringe spacing measurement. For clean signals, the DDP's typically are capable of period measurement accuracies on the order of 2.5 percent of the period. The oscillators used to drive the Bragg cells are very stable and are not believed to be a significant source of error. The dominant error term can be measurement of the fringe spacing because of the difficulty and indeterminacy of the method of measuring it.

The errors estimated from the previous equation represent an upper bound on individual velocity measurements. The actual velocity error will be smaller if the measurements will be distributed about the nominal value (Ref. 7). However, these small errors in individual measurements can lead to erroneous estimates of variance and higher order statistics but will not affect the mean velocity measurement. To minimize this type of error, it is necessary to minimize sources of error within the LV data acquisition system that cause them. Such sources include PM tube noise, radio frequency noise, and simultaneous particles in the probe volume. Therefore, the data acquisition system includes (1) circuitry to limit processed data to a specified frequency band to eliminate obviously spurious signals (2) trigger level to eliminate low-level signals, and (3) error detection logic to eliminate poor quality signals. The frequency band limitations require an accurate estimate of the range of individual

velocity measurements to avoid truncation and biasing of the data. For highly turbulent, oscillating data, it is possible to eliminate useful data by setting filter limits too narrowly, thus biasing the data by eliminating data at one end of the velocity spectrum. In setting frequency filtration limits on DDP outputs, it is necessary to consider and account for the expected flow velocity range. If a velocity falls outside this limit, it is rejected by the processor. Although no *mean* velocities outside the limits occurred, individual velocity measurements outside the limits occurred and were rejected. An example of this type of statistical truncation is shown in Fig. 9. This truncation biases the lower velocity data and skews the resultant velocity histogram. If a velocity is rejected, then another velocity is accepted to replace it because of the requirement for 1000 measurements per data point. The replacement velocity is higher than the truncation velocity and biases the data upward. This biasing shows itself on the unedited histograms (Fig. 10) and requires manual editing to eliminate it. This editing can be done by imposing convenient models of the Gaussian or Chisquare distributions on the histogram and recalculating the histogram limits and statistics. A number of instances of this sort of truncation occurred during this series of experiments. Useful data can still be recovered, but laborious hand editing and calculation are required to do so. A detailed analysis of LDV signal error analysis is presented in Ref. 7.

Two sources of erroneous period data were noted when forming the LDV data into histograms. The first of these sources was represented by velocity samples lying outside three standard deviations from the mean. These samples are generally considered to be bad points and were eliminated from the edited data during processing. A second error source was a statistical 'beating' or fundamental biasing frequency in velocity occurrences that can be clearly seen on the velocity scatter plots (Fig. 9). This biasing appears to be a characteristic of the Model 8 DDP caused by the error control logic used by the processor. The periods of the signal rejection (or preference) frequencies seen on the scatter plots are multiples of 4, 5, and 8, and appear to be functions of the error control logic. How this may be affecting the data is still under investigation.

4.0 TEST RESULTS

Inconsistencies have occurred in the application of test cell recirculation-induced corrections to turbofan engine performance. The differences are the result of a lack of uniformity in the methods used by industry to acquire and analyze engine test data. This inconsistency has led to a systematic effort at AEDC to examine and isolate the causes of test cell recirculation.

Studies were conducted of methods used by AEDC and the General Electric Company to correct for the effects of test cell recirculation. Full-scale engine and 1/10-scale engine flow

model data for the General Electric TF39 and CF6-50 engines were examined in an attempt to isolate the test cell recirculation effects on engine performance (Fig. 11). The results of these studies are discussed in Sections 4.1 and 4.2, and selected data are plotted in Figs. 12 through 31.

An experimental test program was conducted of a subscale model of a CF6-50 fan exhaust discharging into a simulated subsonic J-2 test cell. The objectives of the experiment were to: (1) evaluate the effect of cell recirculation on the model flow field, (2) establish baseline data on the pressure and velocity field around the engine that could be used to validate computational models of the flow, and (3) establish methods of reducing or correcting for the effects of recirculation on engine performance. The experimental results are discussed in Section 4.3, and selected data are plotted in Figs. 32 through 36.

4.1 SUBSCALE ENGINE TEST DATA

Static performance tests of a 1/10-scale TF39 engine model similar to that shown in Fig. 11 were conducted by GE at Fluidyne, Inc. test facilities (Ref. 4) and at AEDC (Ref. 5). The Fluidyne tests were conducted both under atmospheric discharge conditions and within a subscale AEDC Propulsion Test Cell J-1 simulator. Comparisons of axial pressure distributions on the model surface under both conditions are shown in Fig. 12. A definite effect of test cell recirculation can be noted since the static pressure profiles on the engine core cowl and plug are significantly different. Figure 13 presents the test cell static pressure axial distributions in percent deviation from test cell reference static pressures for static taps at $\theta = 135$ deg on the test cell wall at a typical nozzle pressure ratio. The variability of the axial static pressure distributions around the model circumference can be noted. Also note that the distributions at the cell wall from Fluidyne data (Ref. 4) and AEDC data (Ref. 5) have opposite gradients.

Nonuniform axial static pressure distributions, noted in Fig. 12, produce a pressure-area thrust decrement on the model support. These static pressure gradients create uncertain pressure forces on the model since their effects are not uniformly known over the model. A comparison between the in-cell and out-of-cell performance was made to consider nozzle internal performance, based on flow coefficient, and the external pressure-area forces. The combined effects comparison should yield the total performance change induced by the test cell. Figures 14 through 17 show the external forces on the core plug and core engine nacelle with the engine model installed in and out of the cell. Comparisons of Fig. 14 with Fig. 15 and of Fig. 16 with Fig. 17 show a decrease in cowl and core engine nacelle static pressure-area forces. Pressure-area force differences of approximately one percent of force can be noted. The nozzle pressure ratios are such that the nozzles are choked. Fan and primary nozzle flow coefficients computed from in-cell and out-of-cell conditions are presented in

Figs. 18 and 19. The agreement between in-cell and out-of-cell data indicated in these curves suggests that there is no significant difference in nozzle internal performance because of cell recirculation.

The subscale engine flow model tests have thus shown that there is a difference between model surface pressure profiles obtained in the test cell and in open air. The changes in profiles affect the overall forces being applied to the model but not model nozzle performance since the nozzles are generally choked. The applicability of these results will be established in the subsequent section.

4.2 FULL-SCALE ENGINE TEST DATA

Data from altitude and sea-level performance verification tests of the GE-CF6 and TF39 engines were examined to determine if cell recirculation induced pressure gradients were present and to compare the methods used to correct engine performance for those gradients. The altitude data were taken in AEDC Propulsion Test Cell J-2 for the CF6-50 by McIlveen and Matkins and in J-1 for the TF39. Sea-level data were taken at GE's Peebles facility.

For the TF39 engine, as with the subscale model data previously discussed, the static pressure profiles along the engine's cowl are plotted on Fig. 20. The static pressure profiles give an indication of the variation of engine cowl pressure profiles between enclosed and open test environments. This particular operating condition is for a fan nozzle pressure ratio of 1.43, which is not a worst case from a cell effects aspect. However, a difference can be noted between the in-cell and out-of-cell pressure profiles. The difference is most distinct near the fan nozzle exit and decreases toward the primary nozzle exit. It was also discovered that the axial pressure gradient on the cell wall can be correlated with engine-corrected airflow, as shown in Fig. 21. Corrected airflow, in turn, correlates closely with fan discharge pressure ratio at a given Mach number and altitude. That is, a change in fan pressure ratio produces a near linear change in corrected airflow. This second correlation implies that fan pressure ratio and cell wall axial static pressure gradients are also correlated in a manner similar to that shown in Fig. 21. Having thus noted a correlation between fan discharge pressure ratio and cell wall pressure gradients for the full-scale engine, now note that the same correlation was observed on the 1/10-scale profile data plotted in Figs. 16 and 17 and with the nozzle coefficients plotted in Figs. 18 and 19. Also note in Figs. 18 and 19 that there is no difference between the coefficients obtained from data taken either in or out of the J-1 simulator. The lack of any effect of cell wall pressure gradients on nozzle flow coefficients and the correlations between mass flow, pressure ratio, and axial gradients noted above imply that axial pressure gradients do not affect nozzle internal performance, and axial pressure gradient levels are dependent on nozzle pressure ratio.

Radial pressure gradients were also noted during altitude and outdoor tests; an example is plotted in Fig. 22. The existence of radial gradients implies that the axial pressure gradients measured at the cell wall are different from those that exist at the engine cowl surface. It also implies that cell internal flows are being entrained by the primary flow and that radial flow accelerations are present. This negates any correlation between measured cell wall pressure gradients and corrections to thrust since the axial gradients are not directly imposed on the engine surface.

Figures 23 and 24 indicate that, for the TF39 in J-1, the axial gradient effects cancel because of the location of the reference pressure measurement (see the Appendix). The choice of the core nozzle exhaust plane for the reference static pressure eliminated the force correction to thrust. This is the reason that TF39 thrust correction was nearly zero for the axial gradient that was imposed on the engine. However, the effects, as seen on the engine surface, do not necessarily disappear since the engine may be encountering a pressure field on its external surfaces different from that seen at the test cell wall. Thus, cell effects may be present even if there is no measureable cell wall pressure gradient.

Full-scale CF6-50 engine core plug and cowl surface static pressure profiles are shown in Figs. 25 and 26 for both altitude test cell and outdoor tests. Differences in the pressure profiles can be noted from these figures and are attributed to cell effects. The CF6-50, as installed in J-2, used plume tubes adjacent to the fan flow and parallel to the engine axis, for measurement of axial static pressures, as shown in Fig. 1. A range of these plume tube pressures, is plotted in Fig. 27 against engine station number. The static pressure gradients at each individual test condition were applied to the aft or downstream projected areas of the engine's external surfaces. The resultant forces were used to correct net thrust to account for cell effects. The reference static pressure used for this correction is taken from a special tap located at the fan exhaust nozzle lip.

It is worthwhile to note here the effect of measurement uncertainty on the cell static pressure. In Fig. 27, a 0.25-percent assumed uncertainty band has been included for reference. Most static pressure measurements have a 0.25- to 1.9-percent uncertainty (Ref. 9), which would include most of the data shown in this figure. This uncertainty would account for as much as 50 percent of the scatter and would significantly affect the level of the gradient force corrections applied from the data in Fig. 27. This method of pressure gradient measurement results in flow measurement uncertainties and data scatter. The plume tubes are close to the fan jet, subjected to mixing flow oscillations induced by the jet, and immersed in the recirculating flows entrained by the jet since the reference cell static pressure, located at the fan nozzle lip, is also subjected to the same flow oscillations. Calculations made in evaluating measurement accuracies at AEDC (Ref. 5) have indicated that a 1.0-percent error

in cell ambient pressure measurement produces a 0.7-percent error in net thrust measurement and specific fuel consumption at engine cruise conditions. The need for accurate cell static pressure measurement is apparent. Hence, a careful choice of the location of the cell static pressure that both minimizes the effect of cell pressure gradients and best represents the environmental pressure on the engine is necessary.

A comparison of the measured plume tube pressure gradients for the CF6 in and out of the test cell is shown on Fig. 28. The location of the reference static pressure measurement plane is also shown. The resulting corrections applied to net thrust for each case are shown in Fig. 29. The high levels of CF6 thrust corrections were a result of the location selected for cell reference static pressure (see Appendix) and the method of pressure gradient measurement previously discussed. Note in Fig. 28 that the CF6 reference pressure is located at the fan nozzle exit and that the gradient downstream of this measurement is negative. The pressure-area terms in the thrust equation are referenced to this pressure measurement. The pressure gradient, applied to the aft-projected area of the engine surfaces, results in a negative (suction) pressure force being applied to the engine. The corrections to thrust that result are shown in Fig. 29 and are compared to TF39 corrections (solid line). The low level of thrust corrections experienced by the TF39 engine resulted from the selection of a reference pressure on the test cell wall at the engine core flow exit plane which was nearer to 'balance' point between positive and negative axial pressure forces (Appendix). Wall statics were used to determine the pressure gradients, reducing the uncertainties associated with the plume tube flow immersion. However, this method does require the assumption that wall pressure gradients are transmitted directly to the engine's surfaces. The presence of radial pressure gradients should negate such assumptions.

An attempt was made to determine the CF6 gradient-induced thrust correction by axial integration of the engine cowl and core plug surface pressures over the surface aft-projected areas as shown in Figs. 25 and 26. The integrations were performed for both the GE-Peebles open-air tests and the AEDC/J-2 tests at comparable test conditions. A force correction was calculated and is plotted in Figs. 30 and 31 along with the corrections determined from plume-tube-measured gradients. The force correction is the net difference between the open-air and test cell engine surface pressure-area force terms and was assumed to result entirely from cell-induced axial pressure gradients. The figures show comparisons on both the core/waist cowl and the core plug. Both methods show a rough similarity in results and indicate that force correction peaks at a fan nozzle pressure ratio of 1.6. The analysis is limited by a lack of availability of data at other test conditions.

In summary, the presence of an effect of test cell engine operation has been established. The effect manifests itself as a pressure profile on the engine surface that is different from that obtained in open-air tests. Pressure gradients measured at that cell wall are dependent

on fan nozzle pressure ratio and do not affect nozzle performance as previously thought. However, the presence of radial pressure gradients clouds any relationship that may exist between cell wall or other cell pressure gradients and changes in engine surface pressure profiles. The best method of determining cell effects is comparison between larger surface pressure profiles obtained in the test cell and in open air.

4.3 SUBSCALE FLOW TESTS AT AEDC

Subscale flow experiments were performed at AEDC in order to characterize the effects of test cell recirculation and to provide an adequate data base for verification of 3-D Navier Stokes computational models currently under development. This experimental series used the previously described variable-geometry flow model of scale 43:1 (Figs. 2 through 4) to characterize a simulated high-bypass turbofan exhaust discharging through a test cell into a flow collector/diffuser. The velocity and pressure field around the model was mapped with 2- and 3-axis laser velocimeters and a radially adjustable total-pressure probe. Static pressure and temperature measurements were made at the model's surfaces to further describe flow-field boundary conditions.

The tests were performed in Research Test Cell R1A1 at AEDC in two phases. Phase I defined the significant geometric and flow variables in the axisymmetric flow-field case. The results were used to specify the geometry for the Phase II experiments. A summary of the tests performed is given in Table 4. The test conditions were selected from typical flow conditions used during CF6-50 testing in J-2. Test condition 1 represents an altitude cruise condition, whereas 2 and 3 are intermediate conditions. Related pressure and velocity data were plotted and compared for each relevant test matrix point.

In Phase I (see Section 3.5 and Table 4), the geometry and flow variables identified as most significantly affecting test cell recirculation were the spacing between the nozzle and the diffuser and the diffuser size (Fig. 2) as well as nozzle flow rate. Secondary flow rate, bulkhead axial position, and the entrance cone had minimal effect on the recirculating flow rates within the limits tested.

Comparison of flow-field velocity vectors in Figs. 32a and b shows that increasing the diffuser size reduces the recirculation region size and velocities. Note that the line of estimated 'zero' velocity vectors within the recirculation region is longer for Fig. 32a than for 32b. Likewise comparison of Figs. 32a and c shows that reducing the spacing between the nozzle and diffuser reduces the recirculation region size and velocities even more. The cell pressure profiles on the model and measurements on the cell wall or with full-scale or 1/10-scale measurements. This result was consistent with observations noted in Phase II and will be illustrated in the discussion of Phase II data.

Plotted in Fig. 33 are, for the Phase II axisymmetric model configuration (expansion cone on), the flow velocity vectors in the X-Z or vertical plane where X parallels the model centerline and Z is the vertical axis. The flow total pressure (PTP) is equal to 10.2 lbf/in.² (psia), and the nozzle pressure ratio is equal to 3.0. Other conditions are specified on the plot. A zone of low-speed recirculating flow is evident in the aft (right-hand) portion of the test cell. The flow velocity vectors outside the nozzle flow stream are reversed at the middle ($X = 1.95$) scan and are being sharply turned at the right ($X = 3.63$) scan location. Some of the flow within the shear layer is being deflected back into the test cell by the diffuser. Entrainment of the reflected flow can be seen at the left ($X = 2.5$) and middle scan locations. Note the development of the shear layer, especially at the right station scan. The velocity profile is approaching that seen in fully developed pipe flow at this point. Figure 33b shows the velocity vectors for the same set of test conditions with the model rotated 90 deg to the X-Y (horizontal) plane. The same features can be noted as those seen in the X-Z plane except for some small vector differences in the recirculation zones. The existence of differences from one side of the plane to the other and from one plane to the other indicates that the flow is three dimensional in nature. This can be confirmed by plotting the vectors in the Y-Z plane looking upstream, as shown in Figs. 33c, d, and e, which are the vectors at the left, middle, and right stations, respectively. It can be immediately seen in Fig. 33c that the flow is swirling clockwise as it exits the flow nozzle and that there is a fairly large (approximately 150 ft/sec) radial in-flow component as the flow turns to follow the expansion cone. The shear layer mixing and deflection of the flow by the diffuser are shown in Fig. 33e.

Total-pressure profiles were obtained in the same flow region with a radial scanning total-pressure probe. A typical profile is shown in Fig. 33f. Two profiles are shown at each station with a separate scale for each. The profile indicated by the circular symbols is the ratio of the scanning probe total pressure to the supply total pressure, and the profile indicated by the triangular symbols is obtained from a limited range differential pressure transducer. This special transducer was referenced to the cell static pressure (PSFNL) and allowed determination of the location of the shear layer boundary by indicating the point in the flow at which the pressure profile begins to change. This point is shown as a dashed line. The profiles obtained serve as a check on the laser velocimeter data and agree well in trend with the velocity profiles obtained from the LDV.

The cell and model wall axial static pressure profiles were obtained to compare pressures obtained on the model surface to those obtained on the cell wall surface. The respective profiles are shown in Figs. 33g and h. No direct correlation between the profiles on the two surfaces can be noted. Note that the diffuser entrance static pressure rise that would typically be expected in this sort of configuration occurs before the diffuser entrance is reached. The diffuser's influence thus extends upstream of the diffuser flow entry plane.

The effect of changing flow conditions was examined to determine if cell recirculation is affected. The model flow field was mapped at $PTP = 10.2$ psia previously discussed (Fig. 33) and at 19.2 psia (Fig. 34). Shown in Fig. 34 are the velocity vectors in the X-Z plane obtained at a total pressure (PTP) of 19.2 psia and a nozzle pressure ratio of 1.9. Other conditions are identical to those in Fig. 33a. However, a more pronounced recirculation zone is evident when compared to Fig. 33a. The recirculating velocities are higher, particularly near the wall, and are less uniform from one side of the cell to the other. We have seen previously that cell recirculation (that is, cell pressure gradients) is a function of nozzle mass flow, which is consistent with these data.

Since the primary nozzle pressure ratio is sufficiently high to choke the nozzle in both cases, nozzle mass flow is the only other significant parameter that could be affecting cell recirculation velocities. Increases in nozzle mass flow cause increases in recirculating flow velocities. Other features of the flow are the same as previously noted. The velocity vectors in the Y-Z plane are shown in Figs. 34b through d and are similar to those in Figs. 33c through e, except that the swirl and inflow velocities are higher, in line with observed velocities in Fig. 34a.

The pressure profiles are plotted on Fig. 34e and are similar to those plotted in Fig. 33f. The effects of higher recirculation velocity can be seen in the higher differential pressure readings obtained on the upper-right region which corresponds to the right ($x = 3.63$) station LV scan. This area is outside the shear layer; therefore, the reversed higher pressures are evidence of stronger 3-D recirculation. The wall and model surface profiles in Figs. 34f and g, respectively, again shown no correlation.

Installation of a pylon on the model significantly altered the cell and model flows. The velocity vectors for this case are shown in Fig. 35a for the X-Z plane and 35b for the X-Y plane. The vectors in the upper half of Fig. 35a were taken at 45 deg off vertical and projected to the vertical plane. In the radial (Y-Z) planes, shown in Figs. 35c through e, the 3-D nature of the flow is evident. Comparison to the axisymmetric configuration (Fig. 34) reveals the significant effect of the pylon on recirculation velocities and direction and on the swirl velocities. The pylon induced higher recirculation and swirl velocities and reversed the direction of the recirculation vortex in one quadrant, but not in the other three. The result is a highly 3-D flow pattern similar to that observed during the CF6 test in J-2 (see Fig. 1).

The total-pressure profiles for the pylon-installed case are shown in Fig. 35f and reveal no significant deviation from the laser velocimeter data in Fig. 35a, as expected. The wall pressure profiles in Fig. 35h reveal significantly higher variation (one percent) in cell wall pressure than was exhibited in the axisymmetric case. This resulted from the large variations in internal cell flow velocity and the suspected impingement of flow on the cell walls. No

correlation could be noted between pressure profiles on the cell wall and those on the model surfaces, which is in line with previous observations.

Removal of the diffuser entrance cone with or without the pylon installed also significantly affects the recirculation in the cell, as shown in Fig. 36. The recirculation velocities are increased over the pylon-on/entrance cone-on case (Fig. 33a), and the vortex is moved slightly forward. The diffuser, in either case, cannot capture all of the flow and deflects some of it back into the test cell. The velocity increase is most likely attributable to the bluntness of the diffuser entrance.

In summary, it was found during AEDC's subscale flow experiments that cell recirculation is highly dependent on diffuser geometry and nozzle mass flow rate. Reductions in recirculating velocities were noted with increases in diffuser size and reductions in nozzle mass flow. No correlations were obtained between static pressure gradients obtained at the cell wall and the model surface. This indicates that radial pressure gradients are present that are affecting the model surface profiles. Installing a pylon on the model produced recirculation "cells" within the test cell, as opposed to the recirculation flows observed during axisymmetric tests. The result is a significantly 3-D flow pattern consistent with those observed during full-scale engine tests.

5.0 CONCLUSIONS AND RECOMMENDATIONS

The effects of test cell recirculation on high-bypass turbofan engine performance has been established in both 1/10-scale model and full-scale engine operation. Performance differences can be anticipated and corrected if engine performance is known at the same operating conditions in and out of the test cell environment. This is impractical except at sea-level-static conditions. Hence, requirements have evolved for model and computational studies to characterize the internal cell flows and their effect on performance. This study of cell recirculation has focused on (1) a review of past efforts to characterize recirculation (or test cell) effects and (2) a subscale model study to map the internal cell flows and relate variations in model pressure profiles to the effects of recirculation.

The existence of a test cell effect was established during 1/10 scale engine experiments at Fluidyne. This effect is a decrement on net thrust in the test cell on the order of 0.5 percent. The effect can be "tuned out" or eliminated by variation of cell geometry or by judicious selection of the reference cell static pressure location (Ref. 4). However, this 'tuning out' process is only apparent because recirculation may still be affecting model surface pressures. The CF6-50 full-scale engine data indicated no clearcut test cell effect on engine performance based on engine surface pressure profiles. Pressure measurements near the jet

shear layer made with the plume tubes and resultant corrections to engine performance yielded thrust increases of approximately one percent, but there is no certain relationship between differences in plume tube or cell wall pressure measurements and pressure variations on the engine cowlings, which are the real indicator of cell effects. The measurement of radial pressure gradients in the jet shear layer during TF39 testing disproves any linear relationship between cell wall or near-field axial pressure gradients and engine cowl axial pressure profiles.

Mapping the subscale AEDC model flow field with the laser velocimeter established the existence of the recirculation zones. The recirculating mass flow is a function of primary mass flow, diffuser size, and nozzle-diffuser spacing. Increasing diffuser area by 10 percent and reducing nozzle diffuser spacing by 25 percent (see Table 4, test matrix No. 8 for baseline) improves flow capture and appears to have minimum effect on model surface pressures. A further increase of 15 percent in diffuser area would permit capturing all of the expanding nozzle flow and eliminate reflection of flow from the entrance cone or lip of the diffuser. The installation of the expansion cone dramatically improved model flow control and the geometric reality of the simulation by restricting the nozzle flow area and eliminating choking of the diffuser. No consistent correlation could be established between axial static pressure gradients on the cell wall and model pressure profiles regardless of the geometry or flow variations attempted. It must be recognized that this is a 43 to 1 scale cold-flow model with attendant Reynolds number and thermal effects, so the simulation is not exact. However, true dynamic similarity is impossible with any cold-flow model, also not essential, since cold-flow models are designed for establishing the basic features of the modeled flow device and estimating performance.

Planning for future high-bypass turbofan engine tests at AEDC should include the following considerations:

1. Corrections to engine performance because of cell effects should be based on pressure profiles measured on the engine's surface obtained from comparable in-cell and out-of-cell tests. Pressure profiles measured on the cell wall in the presence of radial pressure gradients are not reliable indicators of cell effects on the engine's surface pressure profiles.
2. The reference cell static pressure should be located in a position where it is not affected by cell recirculation. The method outlined in the Appendix can serve as a useful guide to selection of a location, bearing in mind that the location of the cell reference pressure should not be used as a means of correcting for cell gradients.

3. Engine manufacturers generally perform 1/10-scale model tests of their turbofan engine exhaust systems at altitude conditions during development and should take advantage of this opportunity to optimize their cell configurations to minimize cell effects. This subscale data should be made available to AEDC to do the same.
4. The primary diffuser function should be flow capture rather than pressure recovery to ensure minimization of cell effects. The primary means of ensuring this flow capture is to increase the diffuser size such that the fan nozzle flow and shear layer are essentially contained by the diffuser at the test condition of highest expansion ratio/mass flow. This method would necessitate a diffuser-to-fan-nozzle-area ratio of approximately 1.2 to 1.3. The exact ratio should be determined from model flow tests and computational studies.
5. Model tests using the recirculation model can be easily performed to verify configuration choices. The computational models currently under development should also be a primary source of information for configuration choices and optimization at AEDC.
6. An entrance cone should not be necessary if the diffuser is sized properly and the spacing between the fan exhaust and diffuser entrance is minimized. The diffuser sizing ratio should be on the order of 1.2 to 1.3. Based on model studies of the desired configuration, the spacing should preclude pressure effects on the engine from the diffuser. Optimization of these parameters should be based on model experiments and computational studies that relate to the specific engine of interest.

REFERENCES

1. Schulz, R. J. "An Investigation of Ducted, Two-Stream, Variable-Density, Turbulent Jet Mixing with Recirculation." AEDC-TR-76-152 (AD-A034537), January 1977.
2. Smith, G. D. and Giel, T. V. "An Experimental Investigation of Reactive, Turbulent Recirculating Jet Mixing." AEDC-TR-79-79 (AD-A084456), May 1980.
3. Chriss, D. E. "An Experimental Investigation of Ducted, Reactive, Turbulent Jet Mixing with Recirculation." AEDC-TR-77-56 (AD-A044110), September 1977.
4. General Electric Co. "Aerodynamic Model Test Report-1/10 Scale TF39 Model Exhaust System Static Performance." GE DMR-6DT006A03, February 1968.

5. Taylor, D., Simmons, M., and Lee, F. T. "Experimental Study of the Effect of Subsonic Exhaust Gas Diffusers on the Test Cell Wall and TF39 Cold-flow Model Engine Exhaust Nozzle Plug and Core Engine Cowl Surface Pressures." AEDC-TR-73-13 (AD-759177), April 1973.
6. Barnett, D. O. "Seeding Requirements for Laser Velocimeter Utilization in Fluid Dynamics Facilities." AEDC-TR-84-27 (AD-B085361), August 1984.
7. Barnett, D. O. "Design Considerations for a Laser Velocimeter for Engine Testing and Propulsion Diagnostics." AEDC-TR-83-39 (AD-B078727L), December 1983.
8. Abernethy, R. B. and Thompson, J. W., Jr. "Handbook Uncertainty in Gas Turbine Measurements." AEDC-TR-73-5 (AD-755356), February 1973.
9. Bendat, J. S. and Piersol, A. G. *Measurement and Analysis of Random Data*. John Wiley and Sons, Inc., New York, 1966.

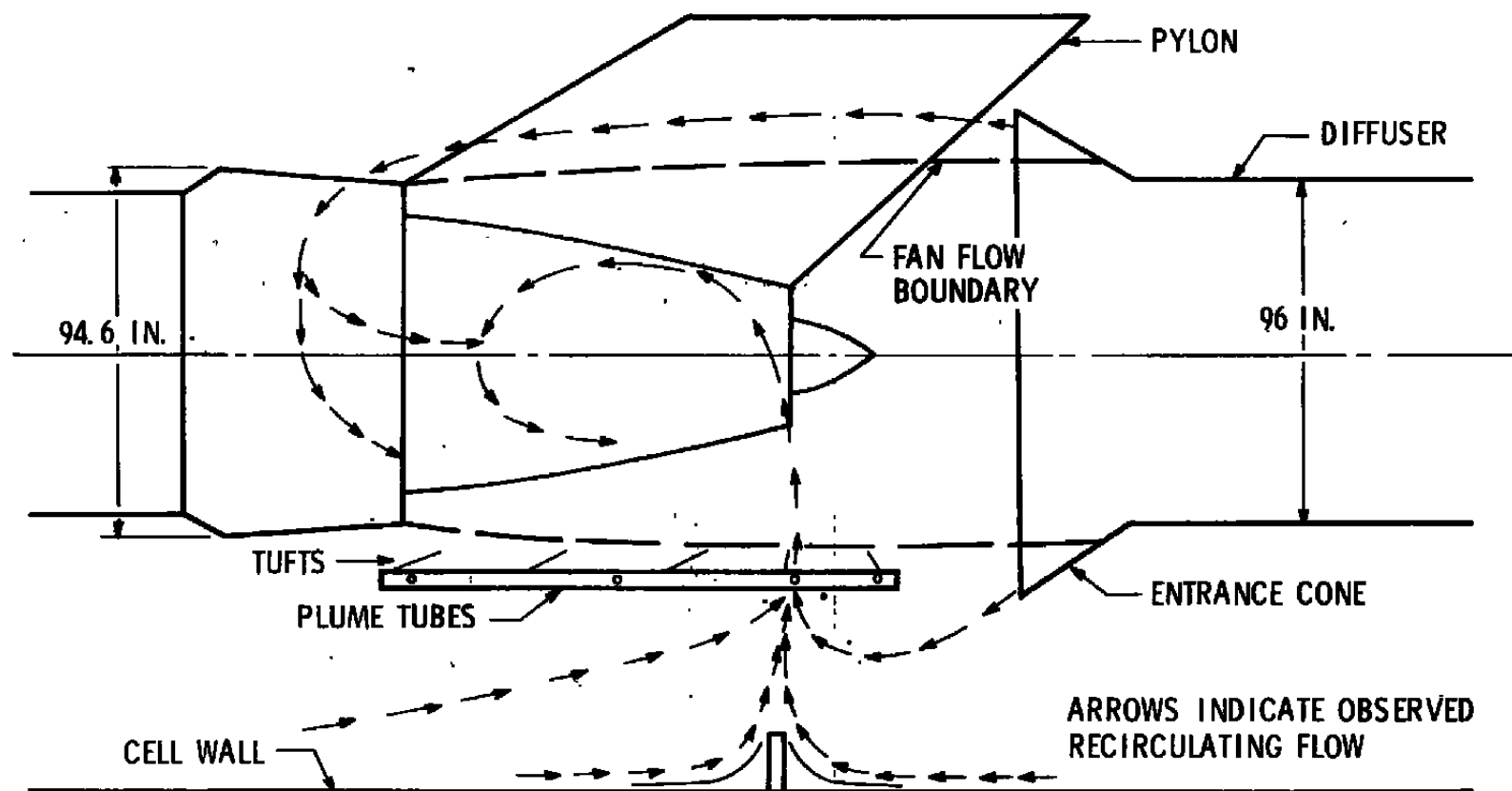


Figure 1. Engine/cell configuration and observed recirculation patterns—CF-50 Engine installed in J-2.

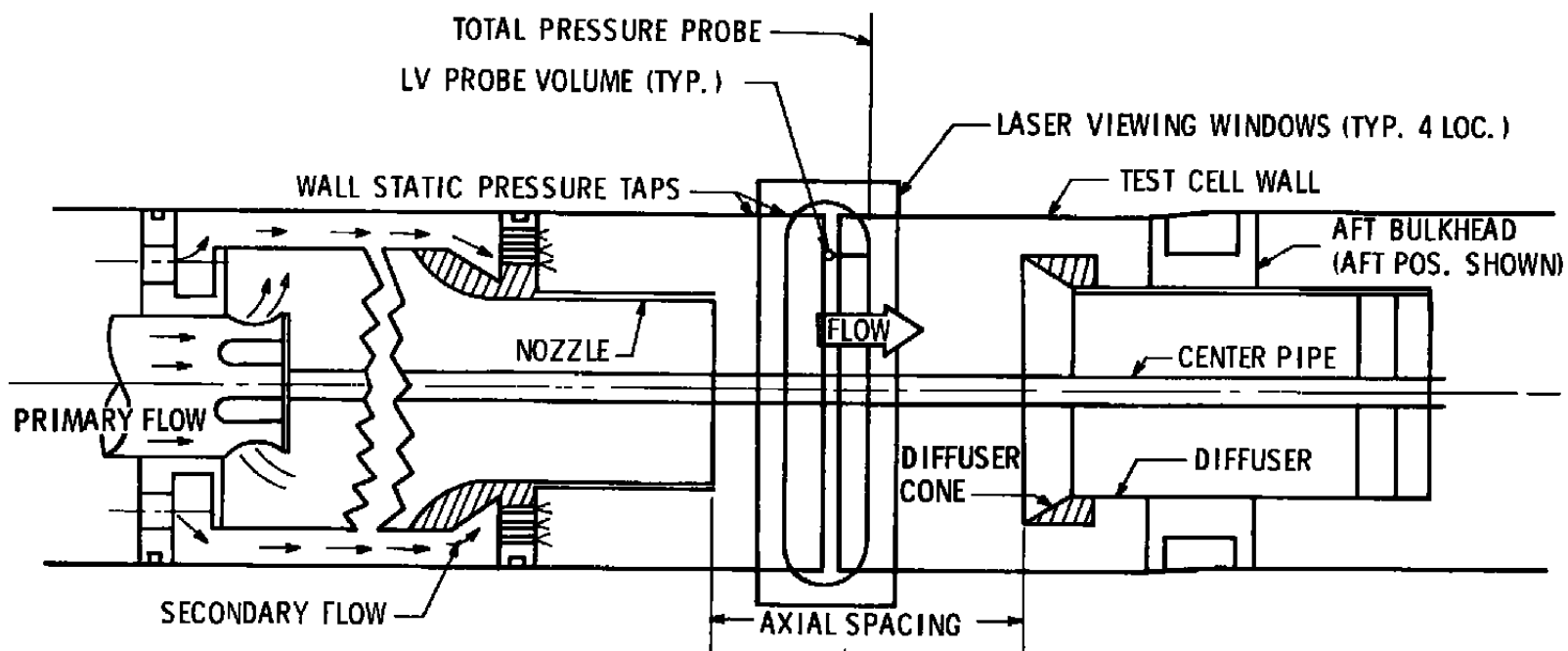


Figure 2. Recirculation model-expansion cone off.

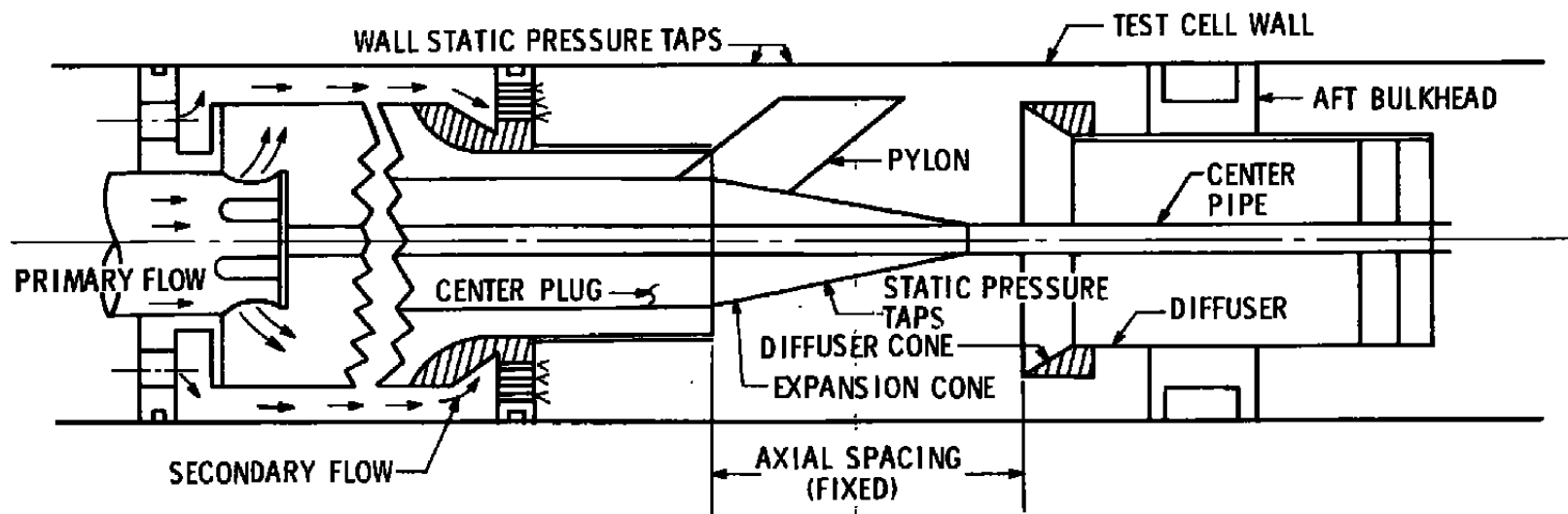


Figure 3. R1A1 recirculation model-expansion cone on.

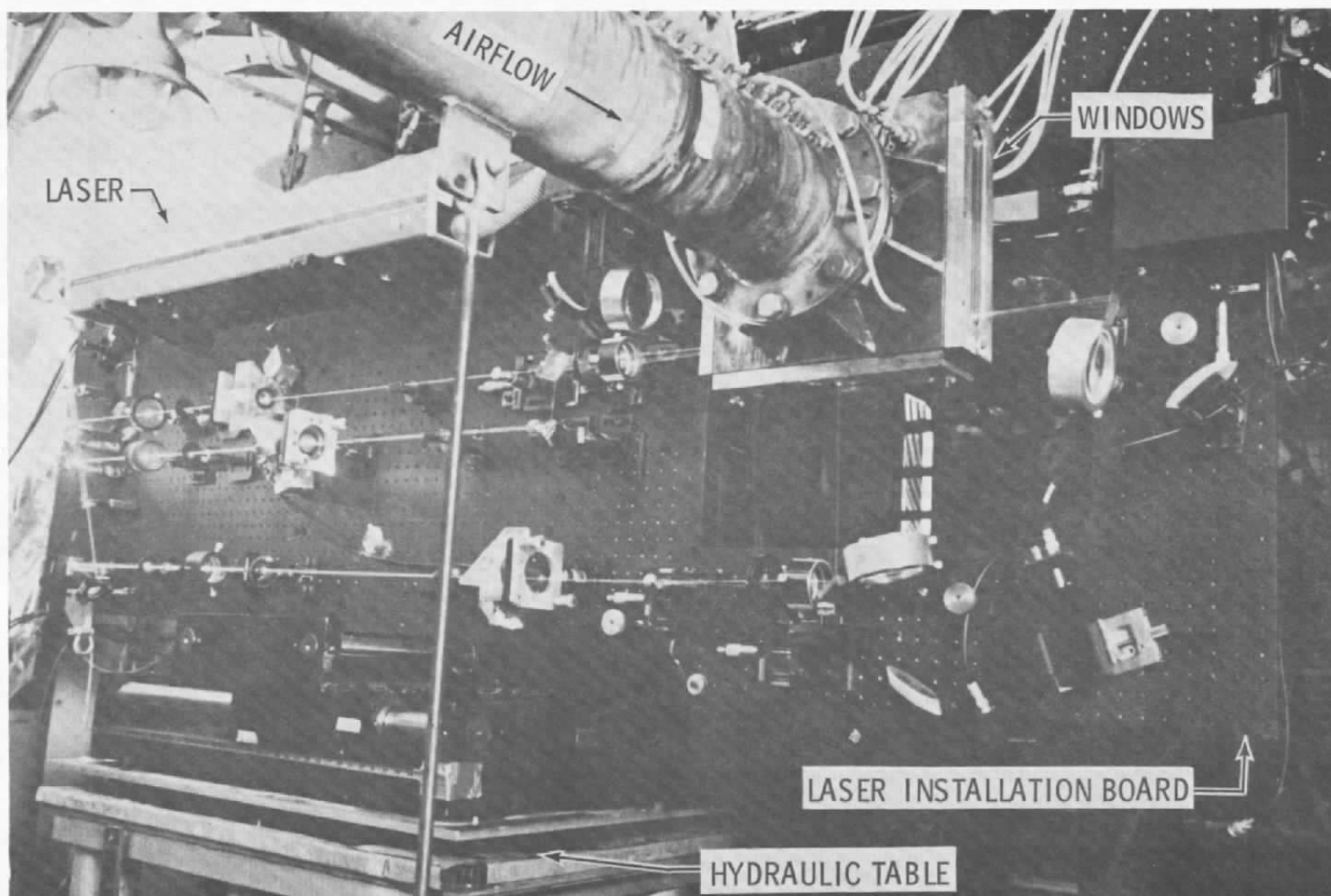


Figure 4. R1A1 laser velocimetry system and test cell.

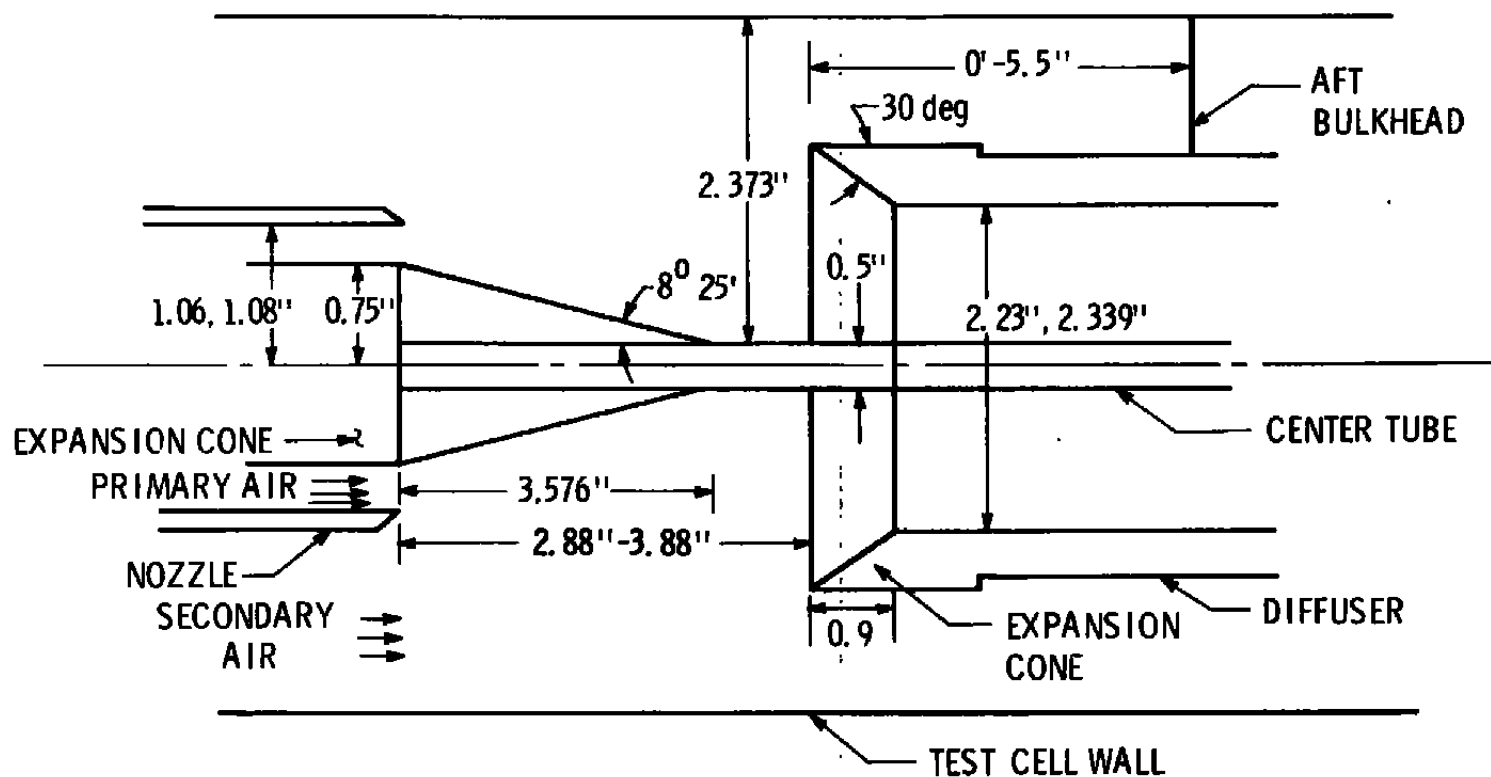


Figure 5. R1A1 model dimensions.

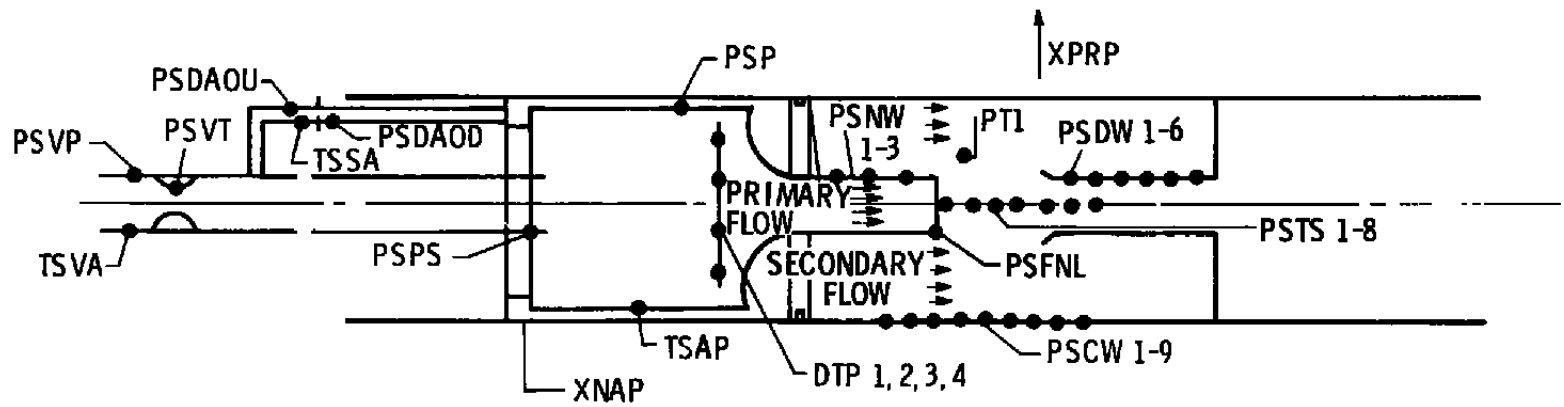


Figure 6. Instrumentation schematic.

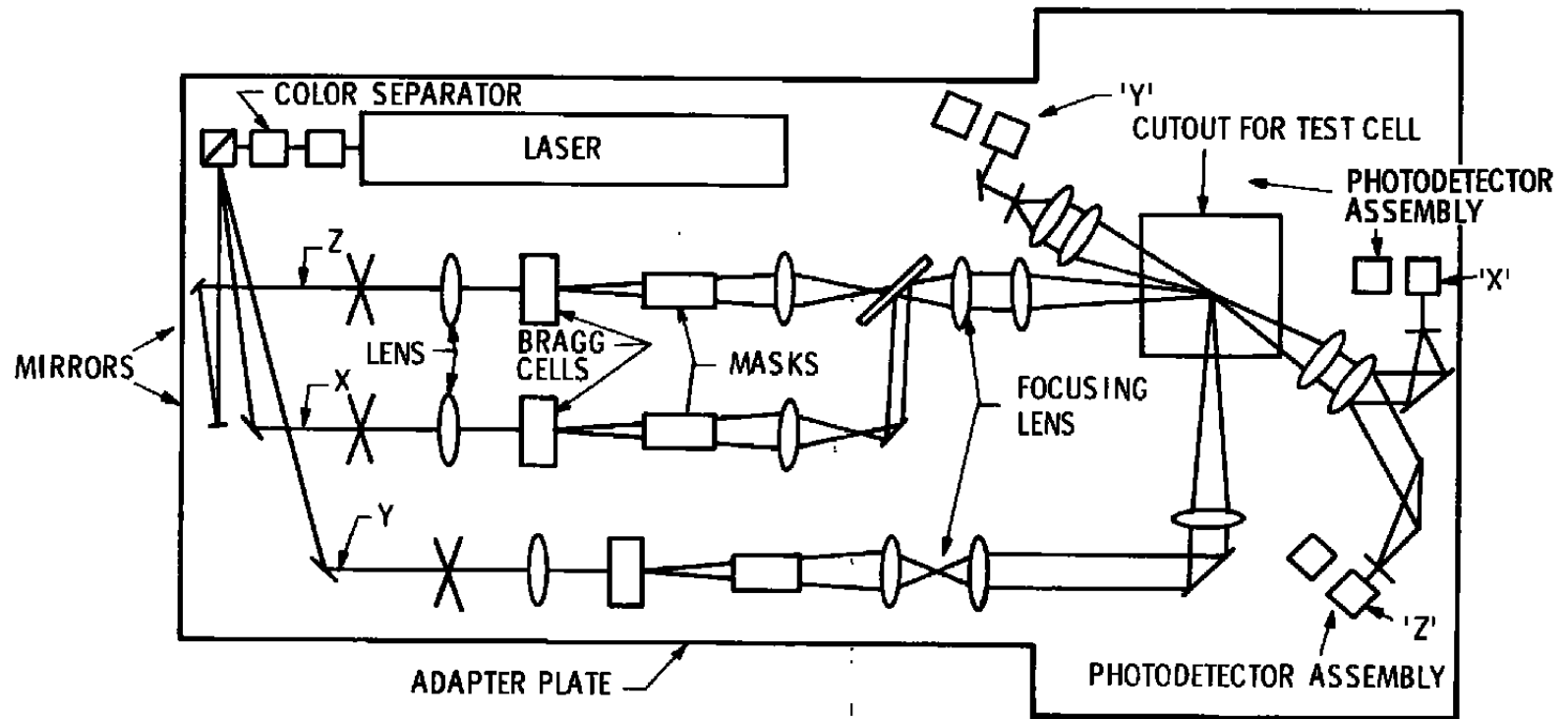


Figure 8. 3-Axis laser velocimetry schematic.

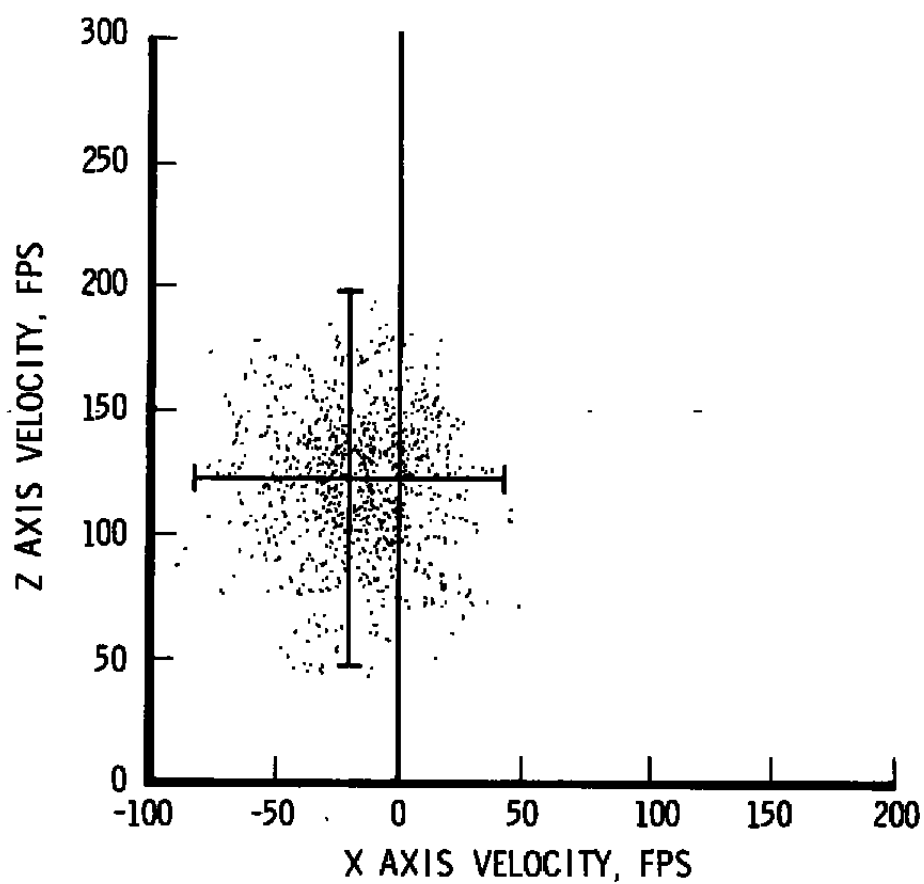


Figure 9. Velocity scatter plot with processor "beating."

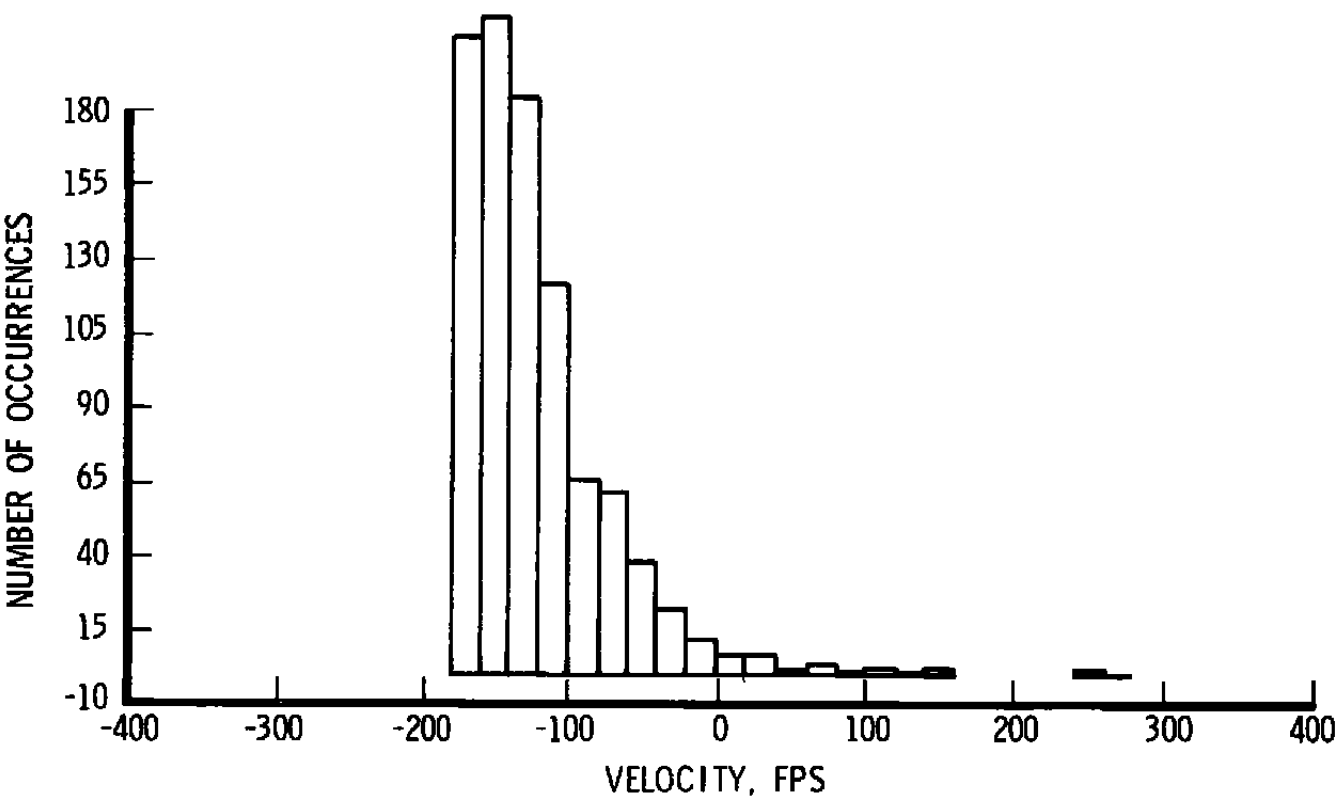


Figure 10. Skewed histogram.

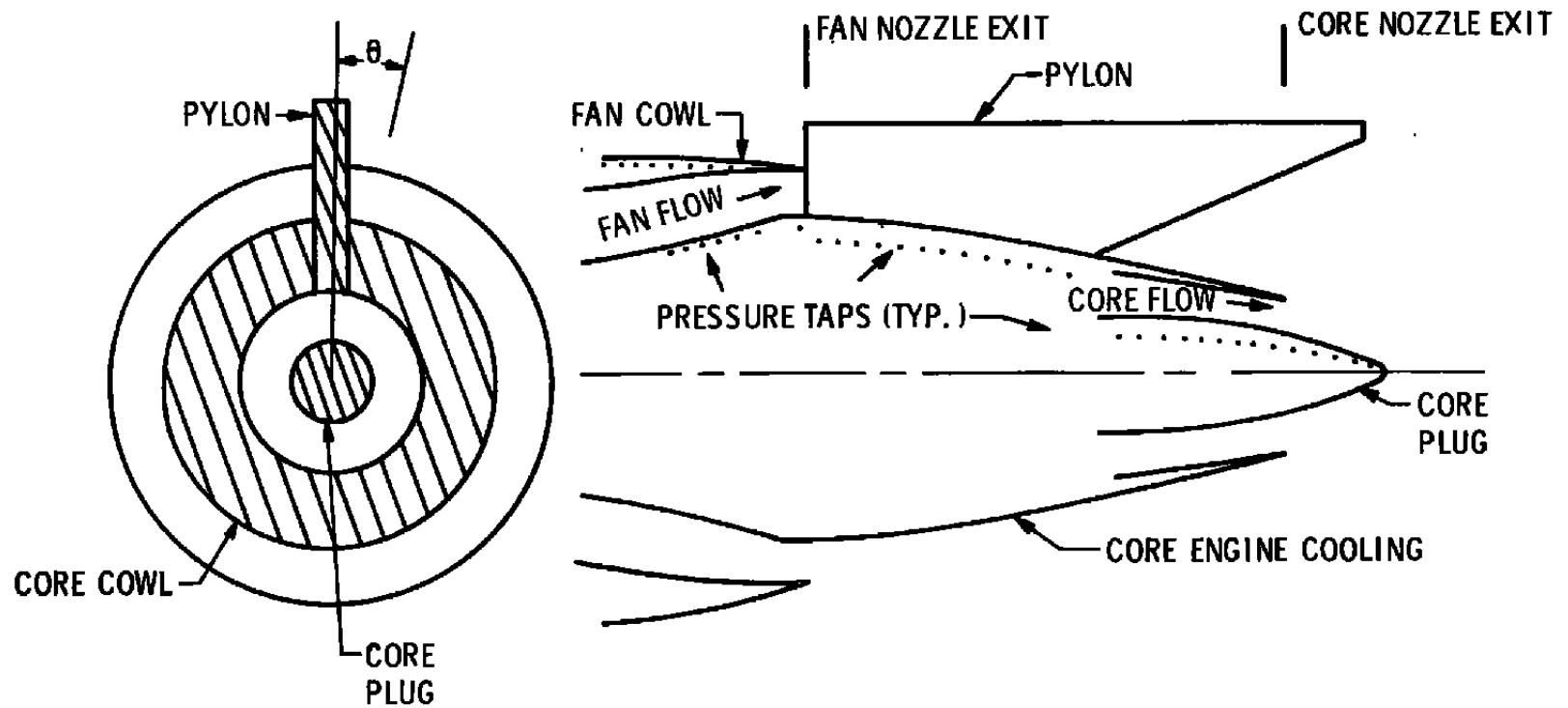


Figure 11. Typical turbofan engine schematic.

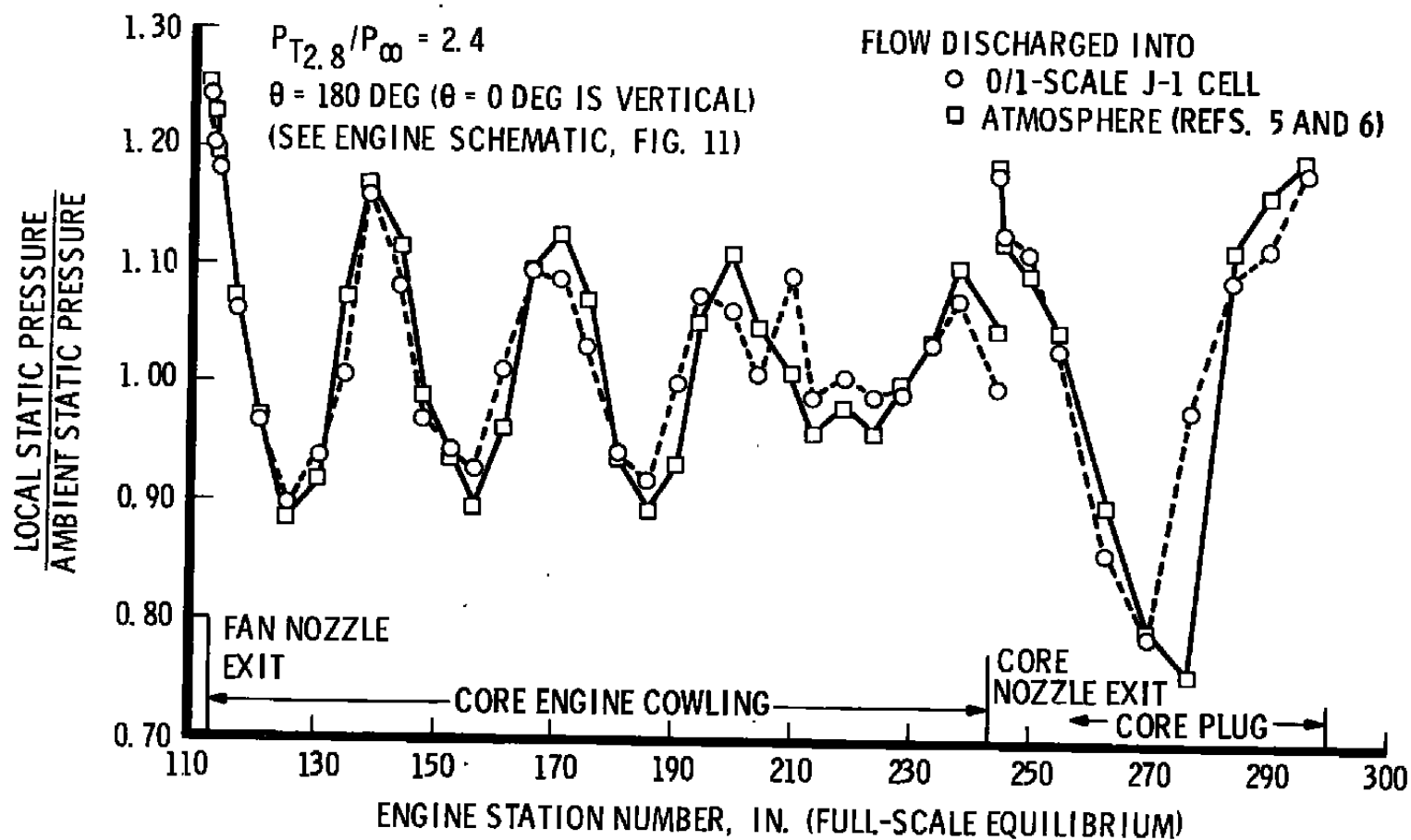


Figure 12. External static pressure distributions core engine cowl and plug 1/10-scale TF39.

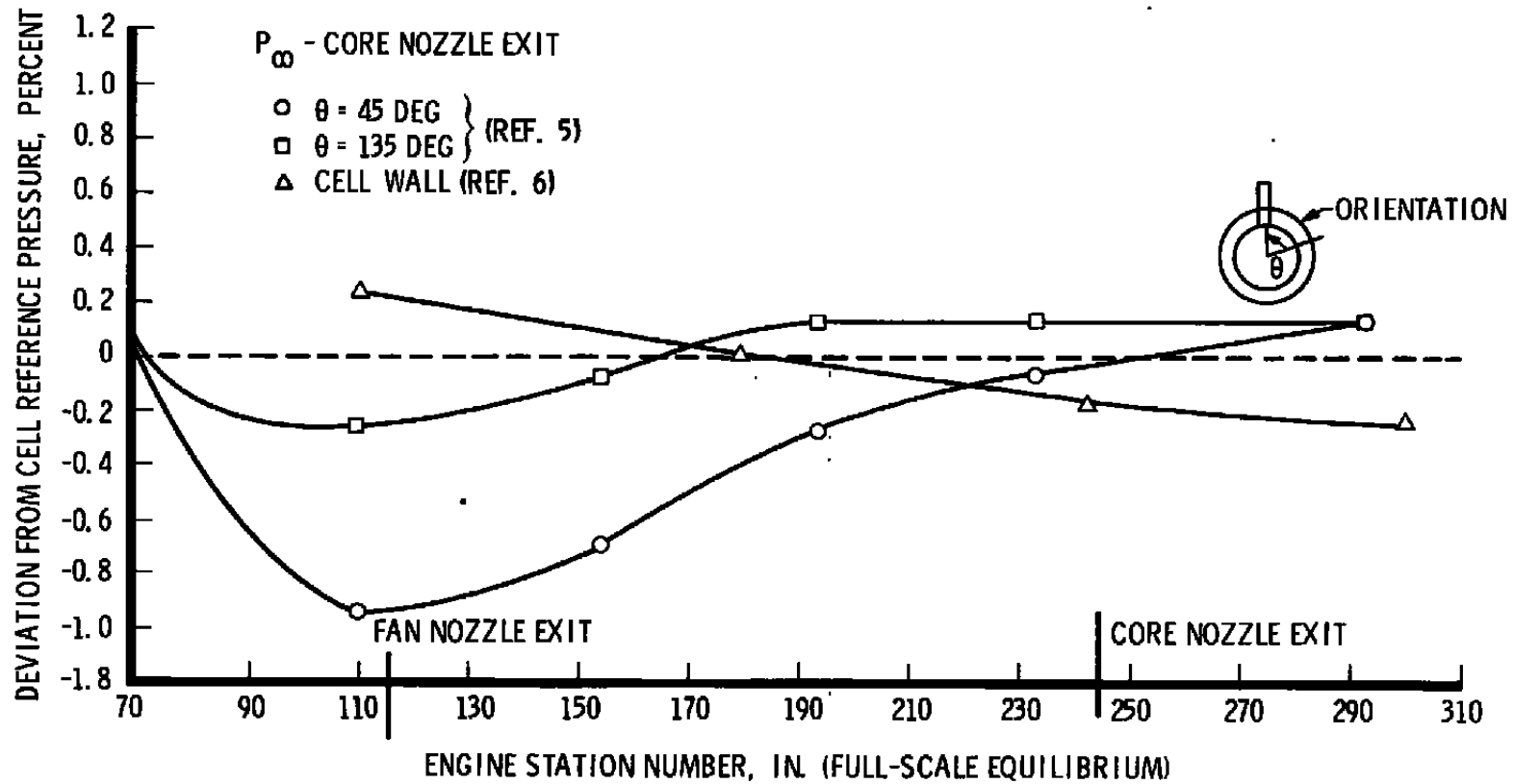


Figure 13. External static pressure distributions.

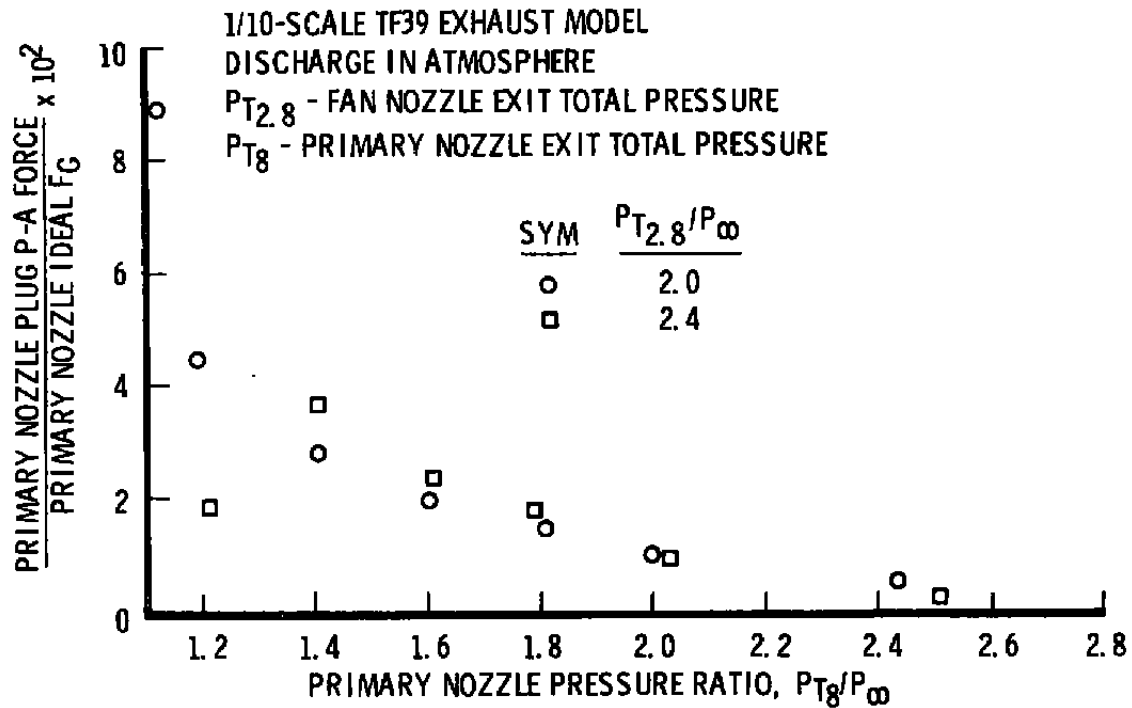


Figure 14. External pressure area force on primary nozzle plug-1/10-scale TF39 exhaust model-atmosphere.

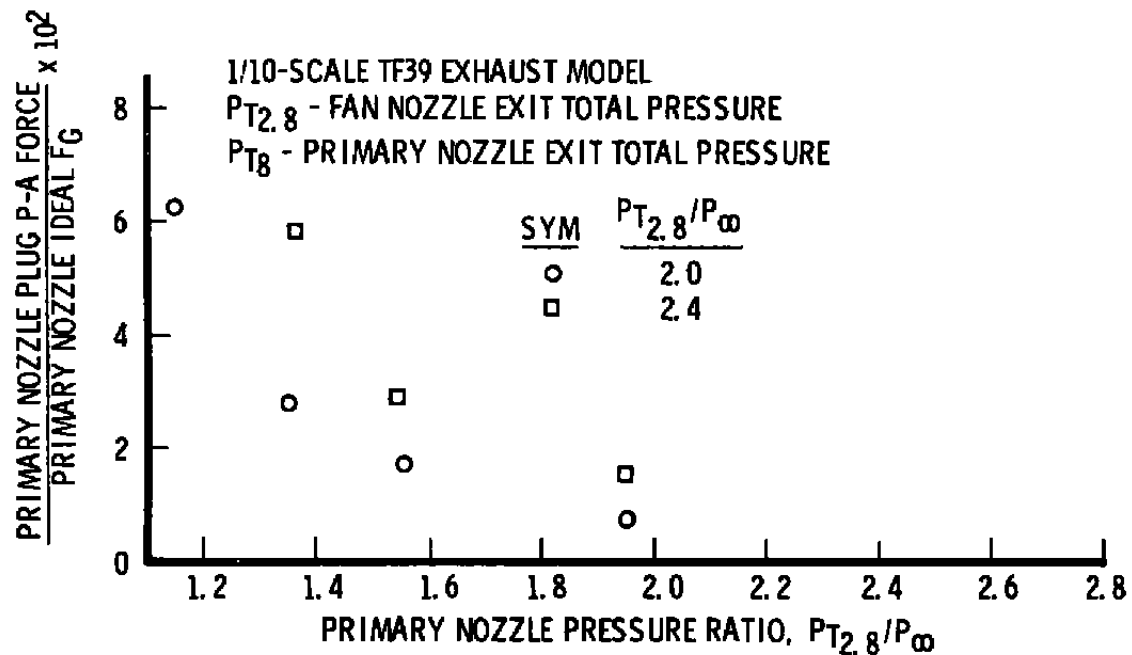


Figure 15. External pressure area force on primary nozzle plug-1/10-scale TF39 exhaust model-J-1.

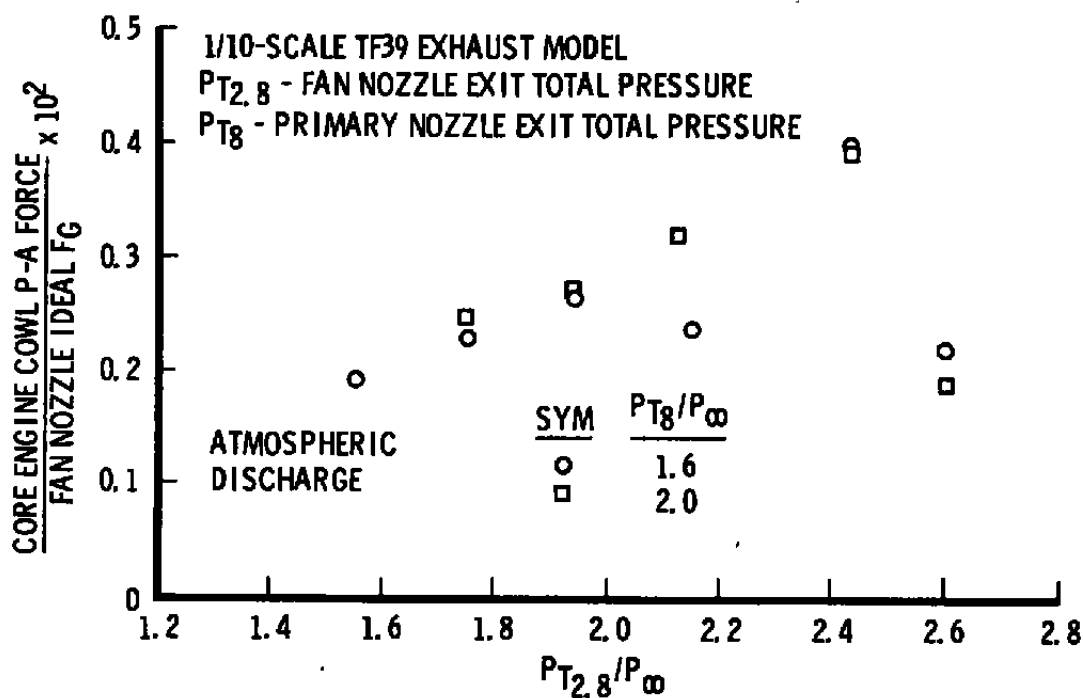


Figure 16. External pressure area force on core engine cowl-1/10-scale TF39 model-J-1.

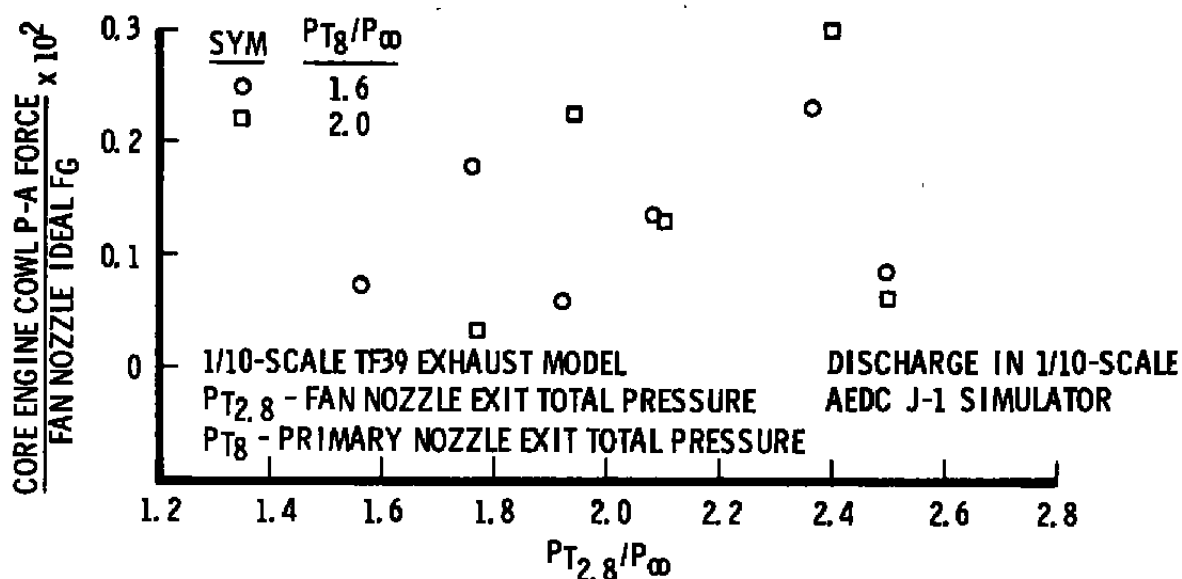


Figure 17. External pressure area force on core engine cowl-1/10-scale TF39 model-J-1.

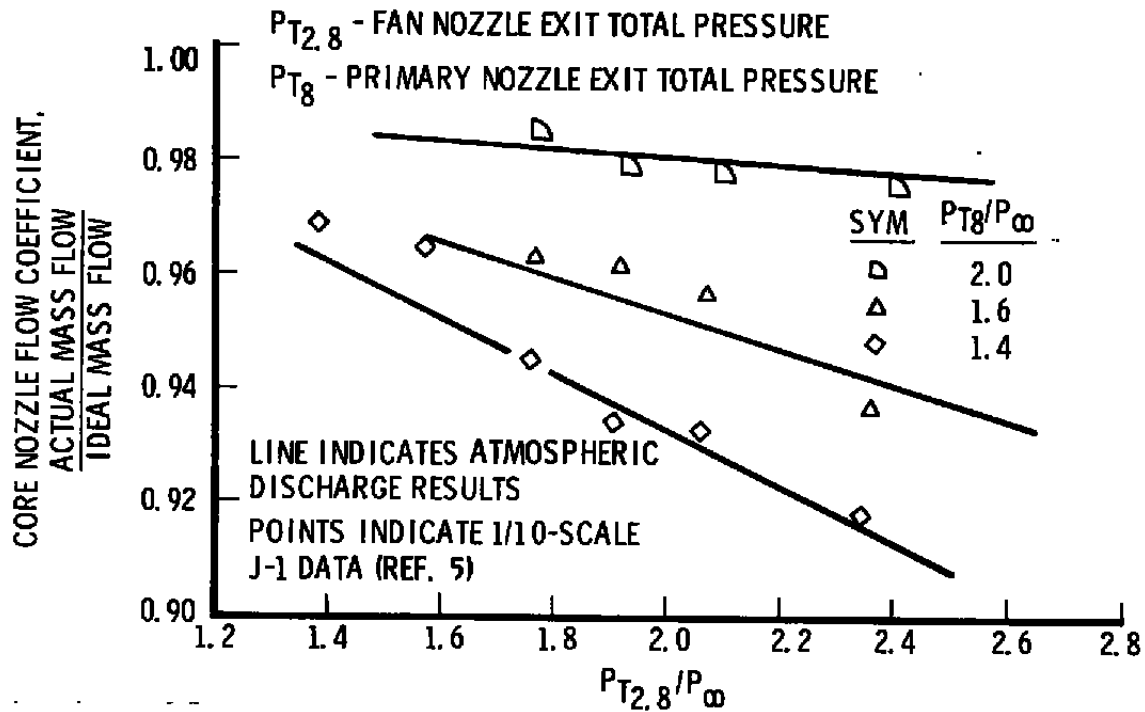


Figure 18. Primary nozzle flow coefficient C_{FB} versus fan nozzle pressure ratio, $P_{T2.8}/P_{\infty}$.

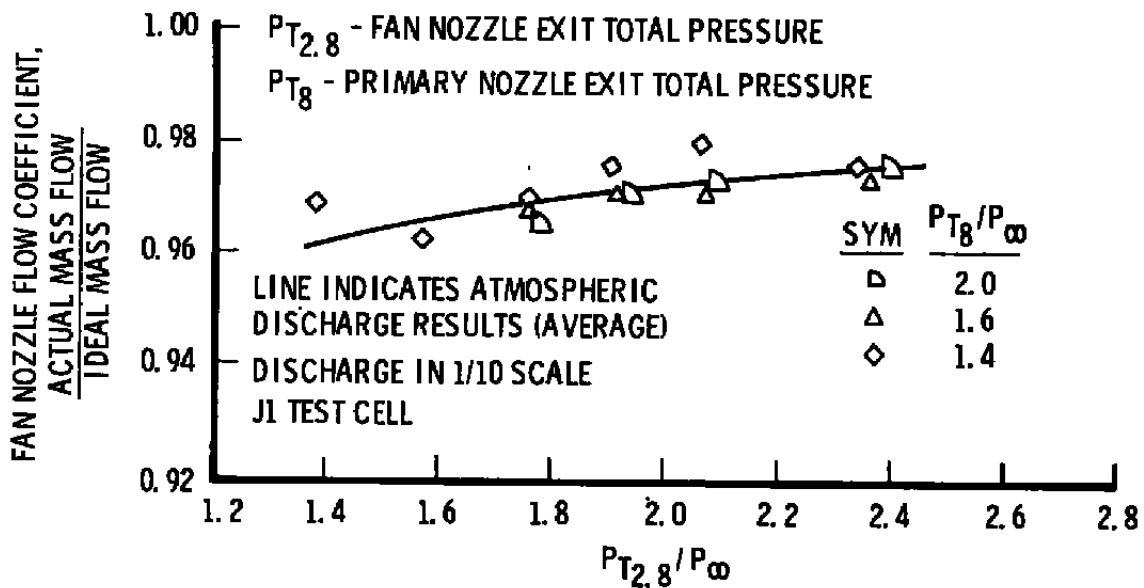


Figure 19. Fan nozzle flow coefficient $C_{F2.8}$ versus fan nozzle pressure ratio, $P_{T2.8}/P_{\infty}$.

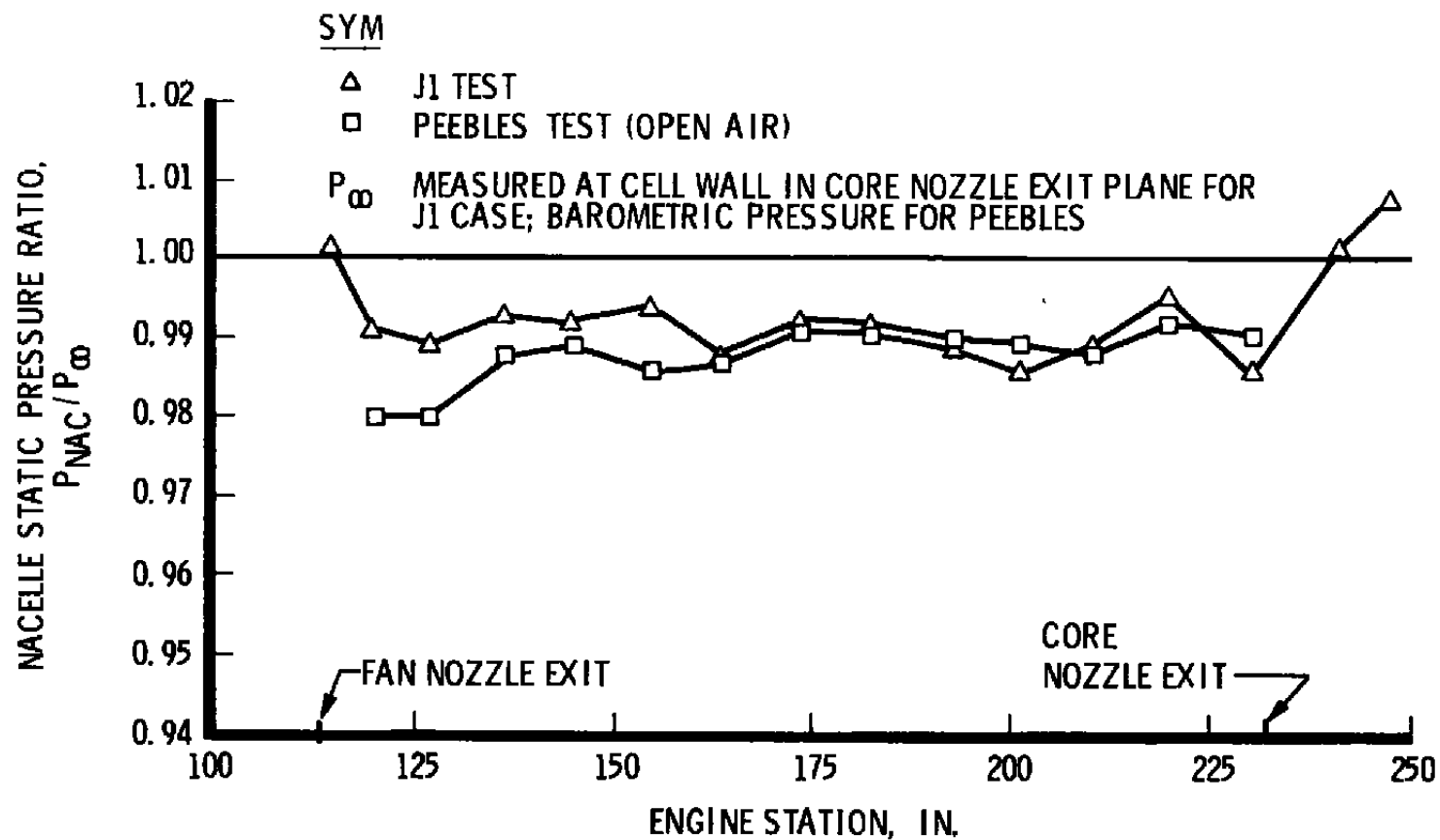


Figure 20. TF39 engine nacelle static pressure axial distribution.

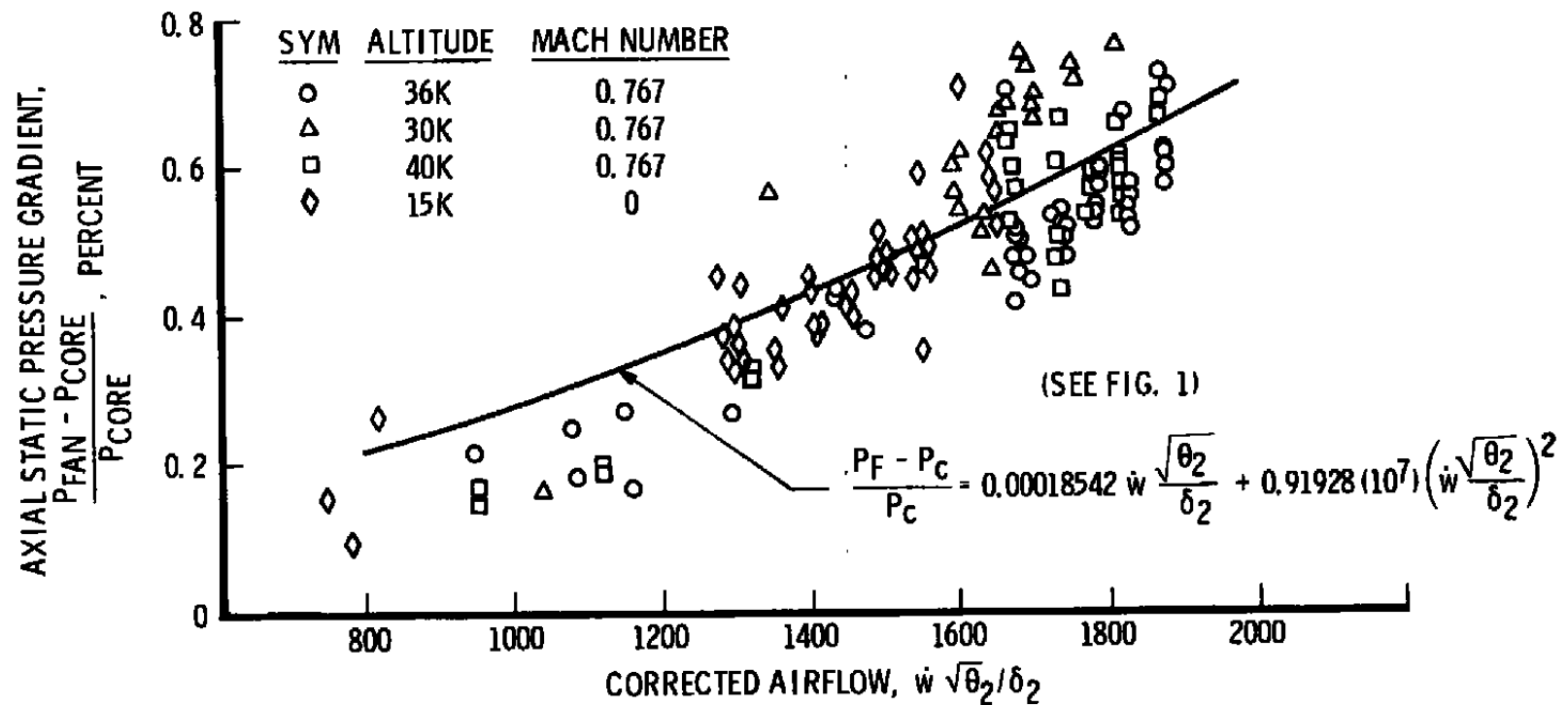


Figure 21. TF39 cell wall axial pressure gradient variation.

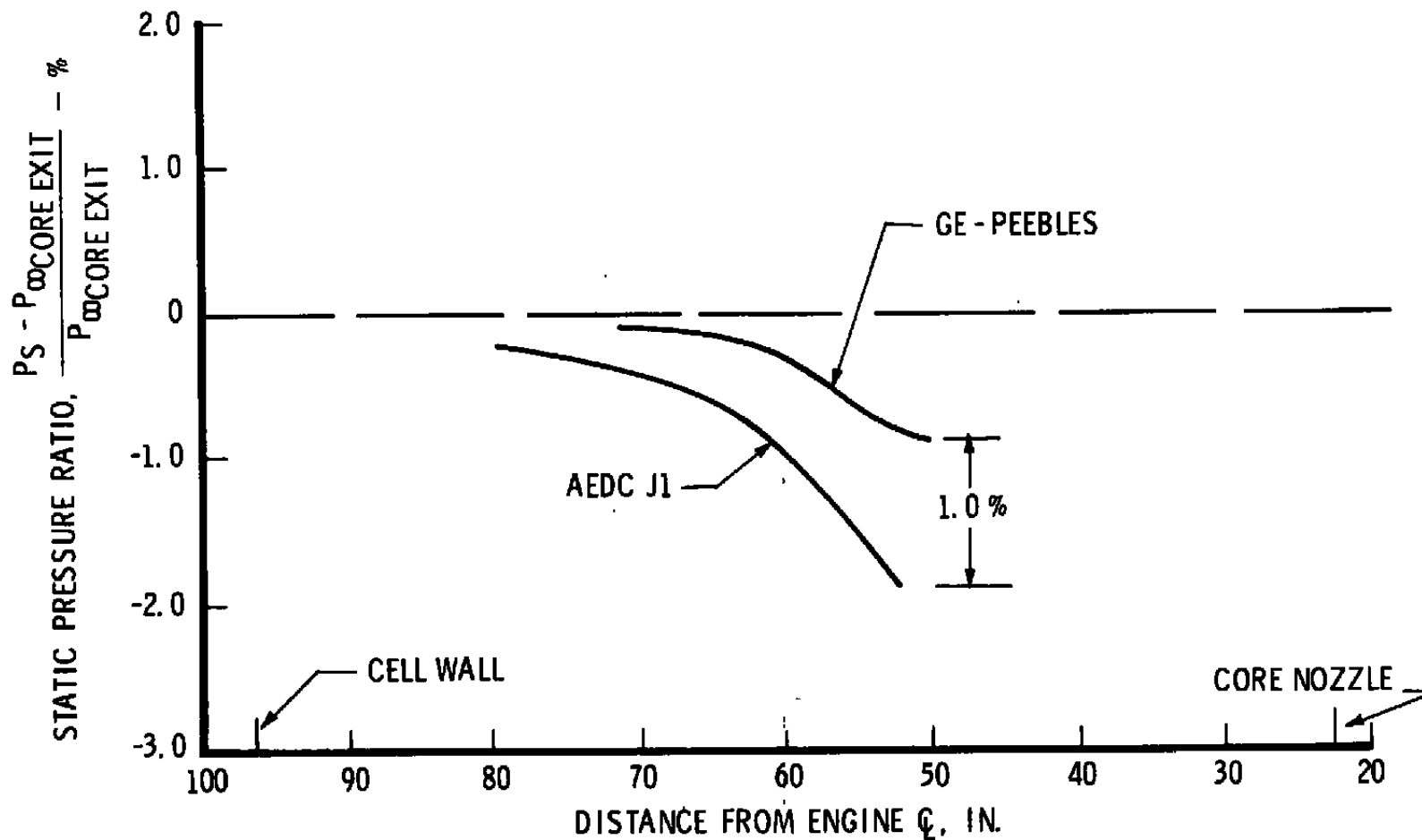


Figure 22. TF39 cell pressure radial gradient-core nozzle plane.

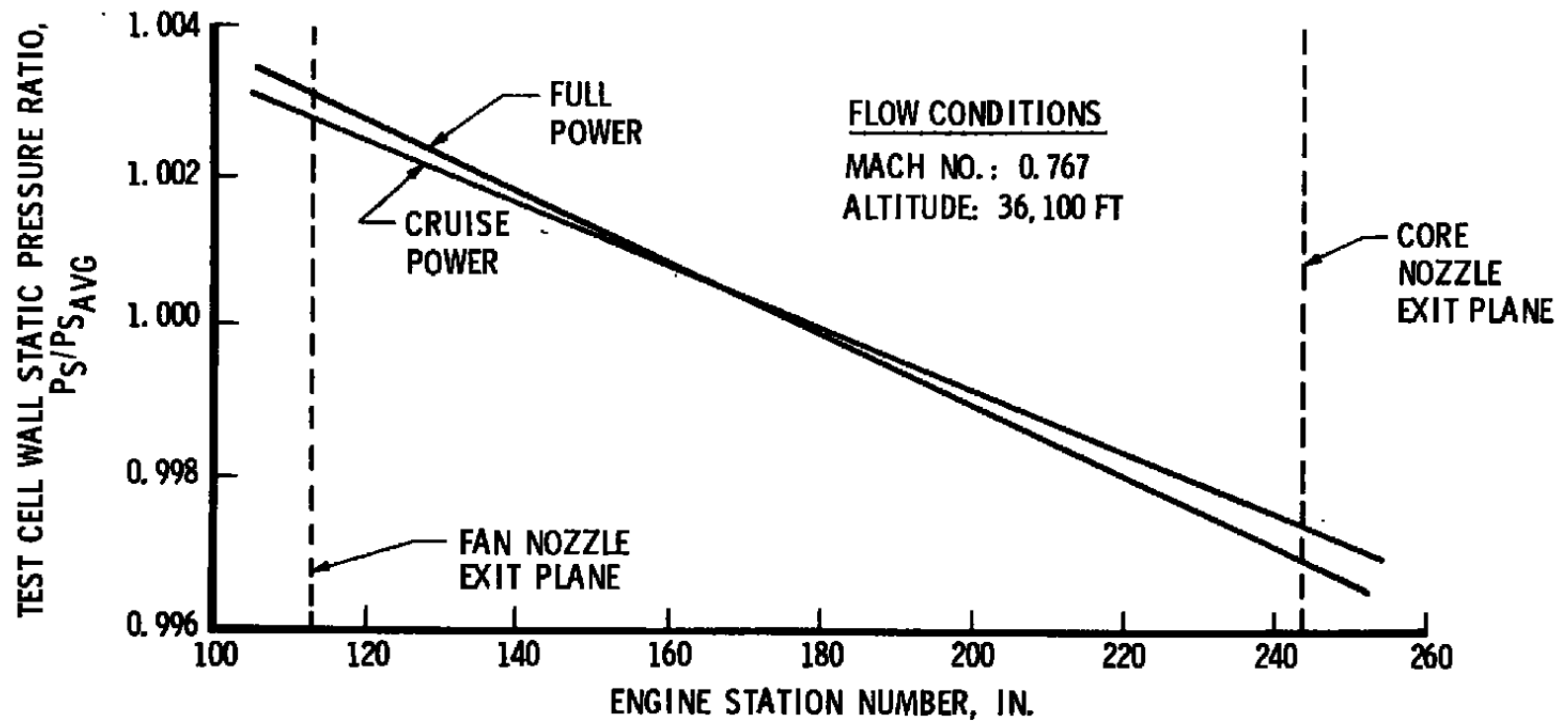


Figure 23. TF39 engine in J-1-net cell wall axial static pressure variation.

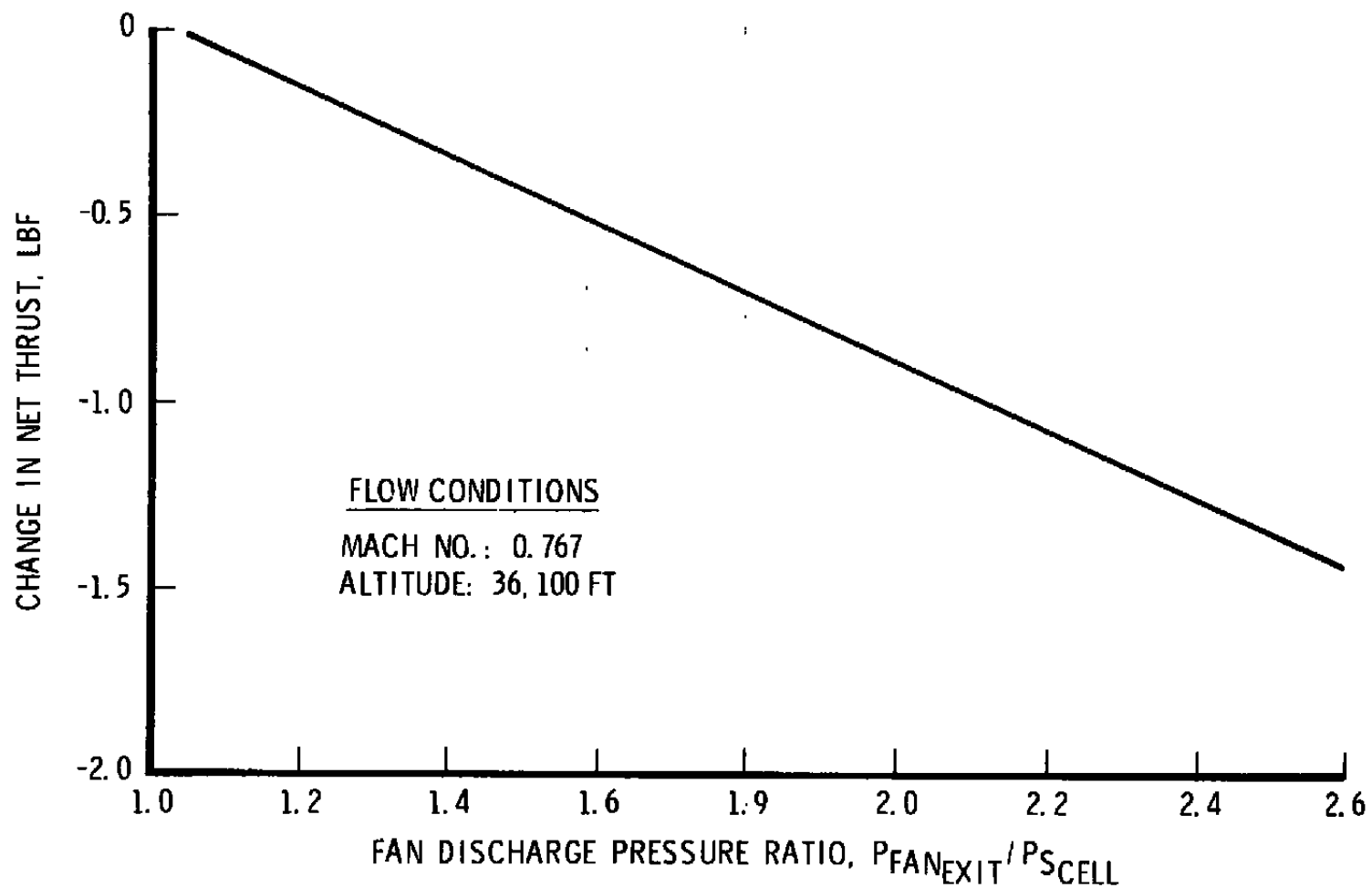


Figure 24. TF39 thrust correction for cell effects.

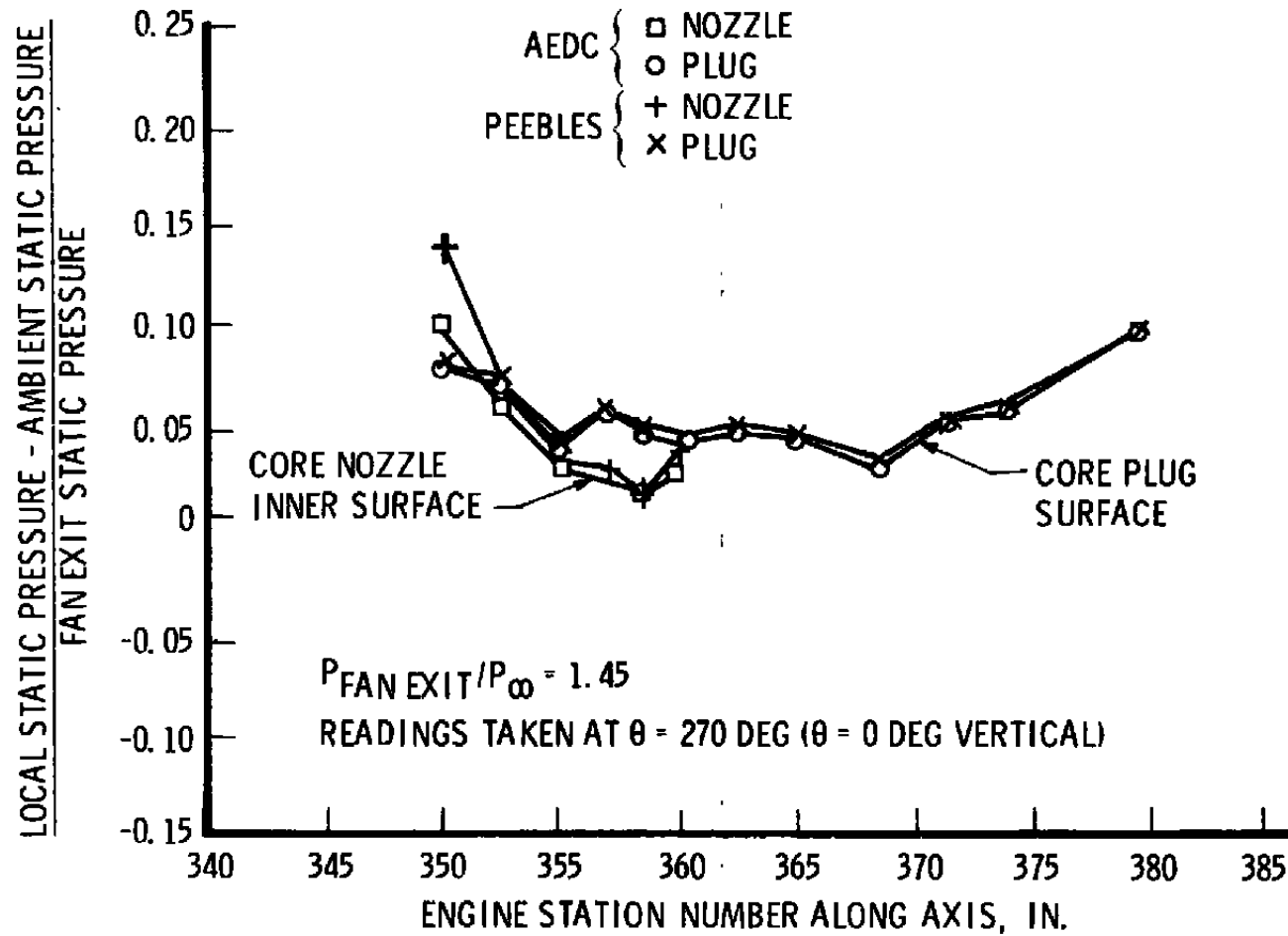


Figure 25. CF6-50 core nozzle pressure profiles.

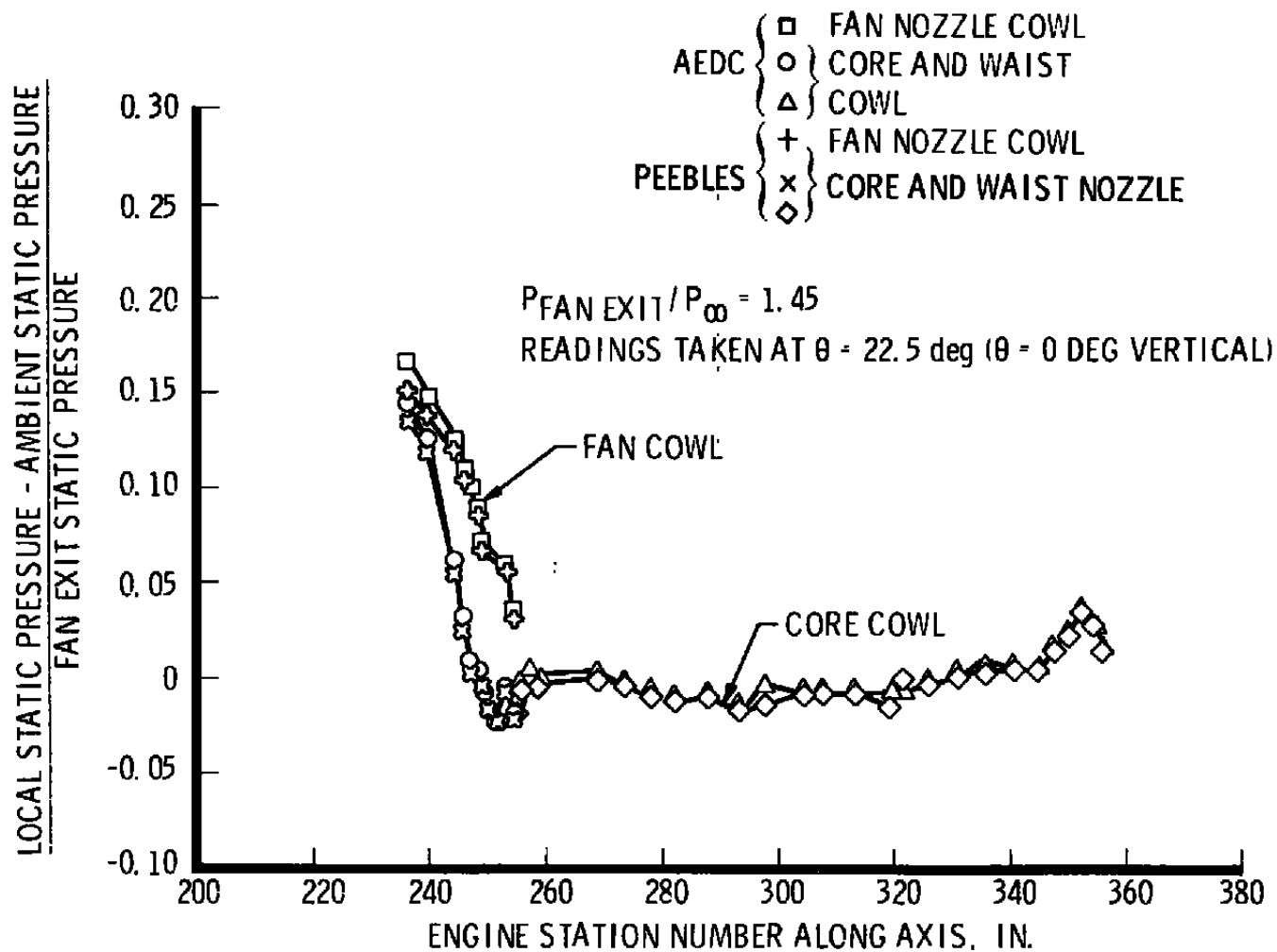


Figure 26. CF6-50 core and fan cowl pressure profiles.

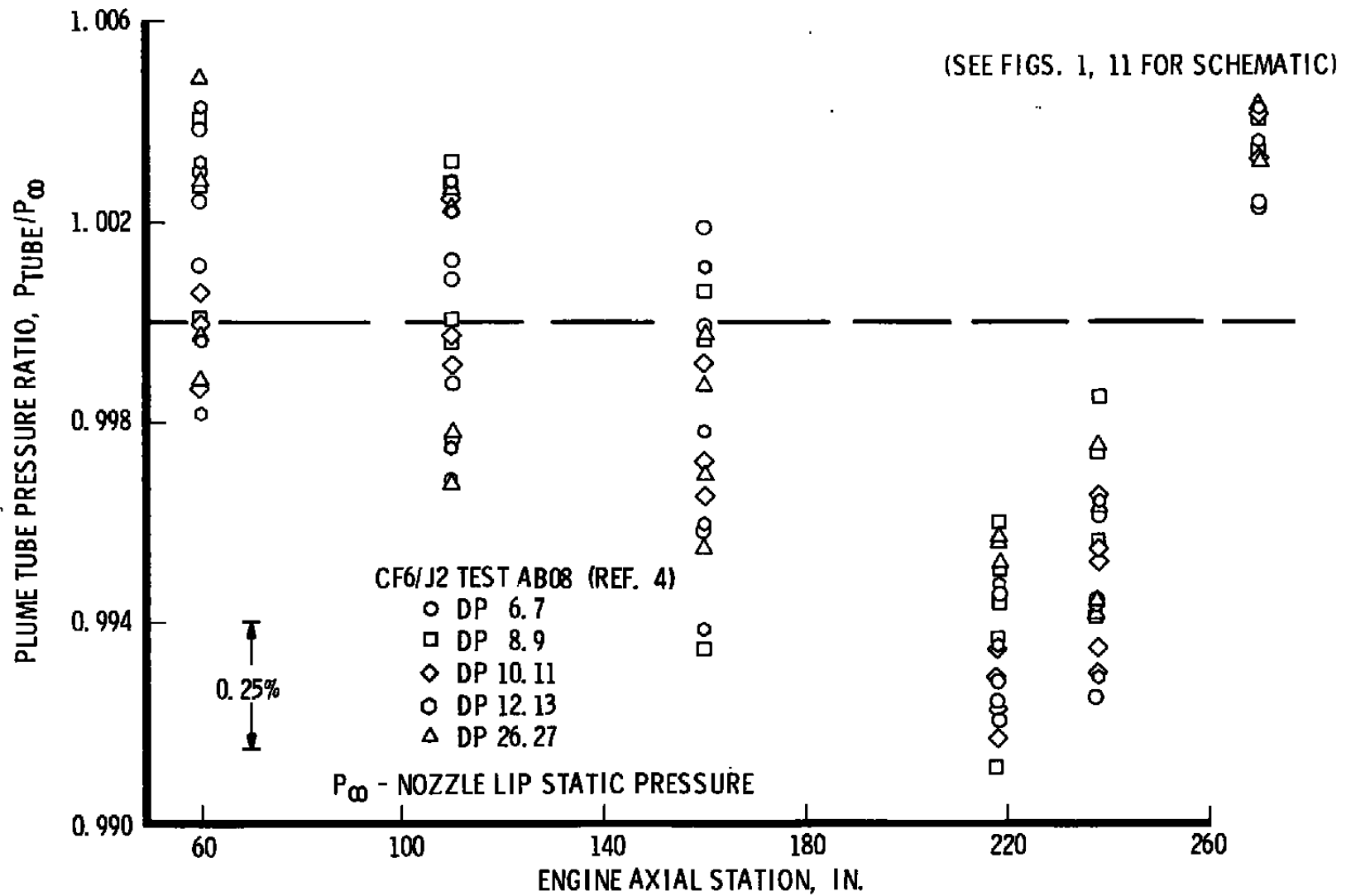


Figure 27. CF6/J-2 plume tube static pressure profiles.

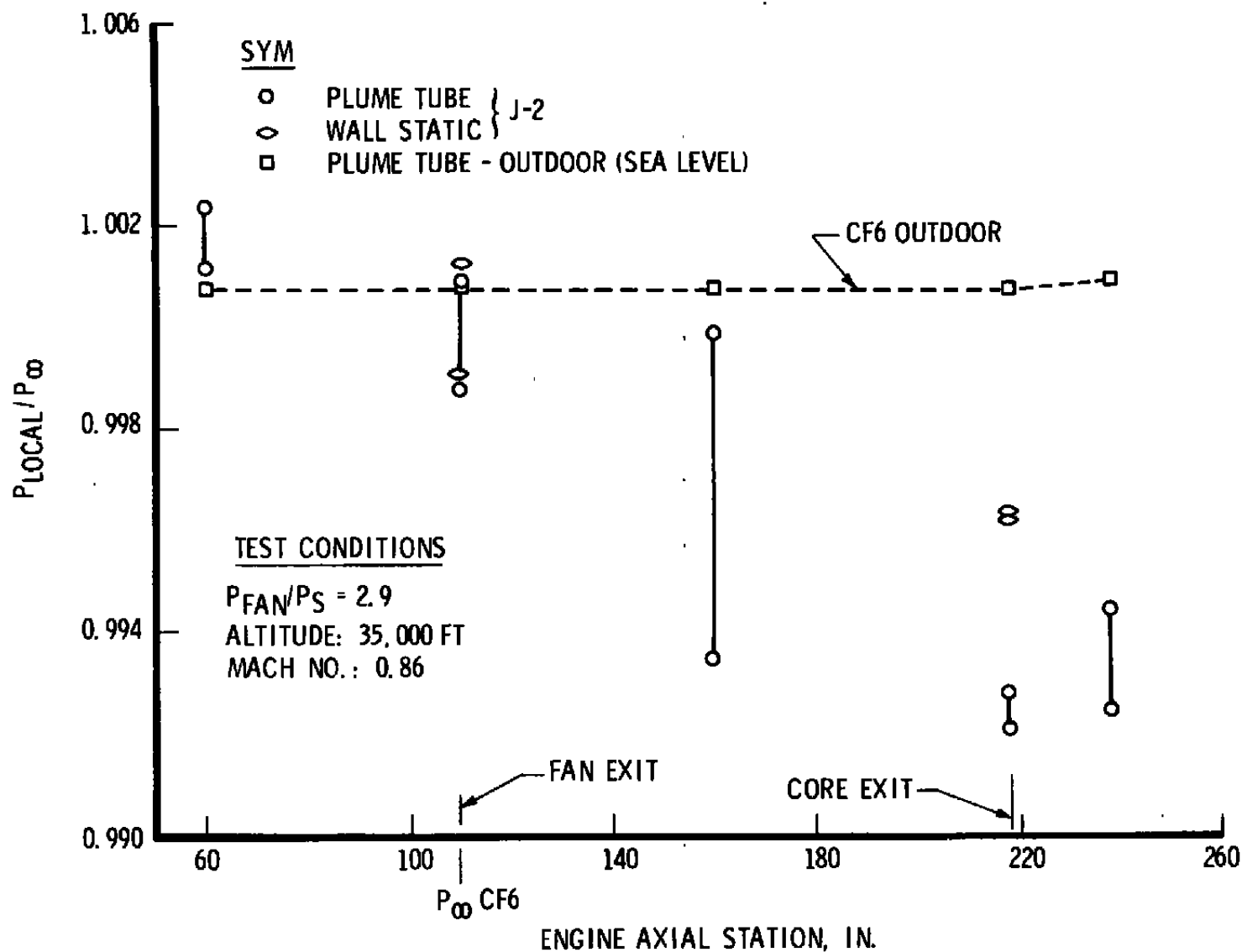


Figure 28. CF6-50 pressure profile-altitude to sea-level comparison.

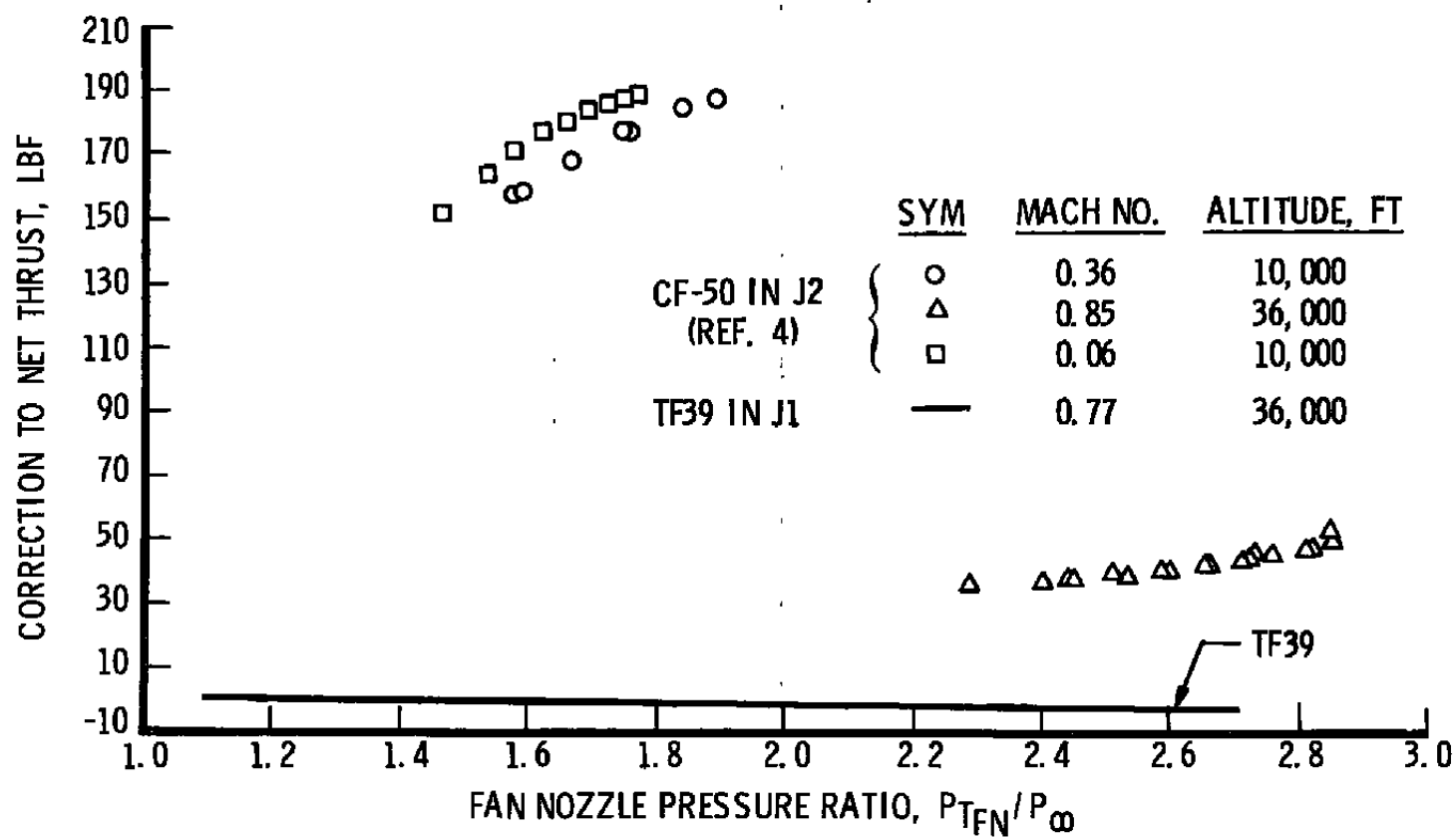


Figure 29. Comparison of recirculation induced net thrust corrections for TF39 and CF6-50 engines at AEDC.

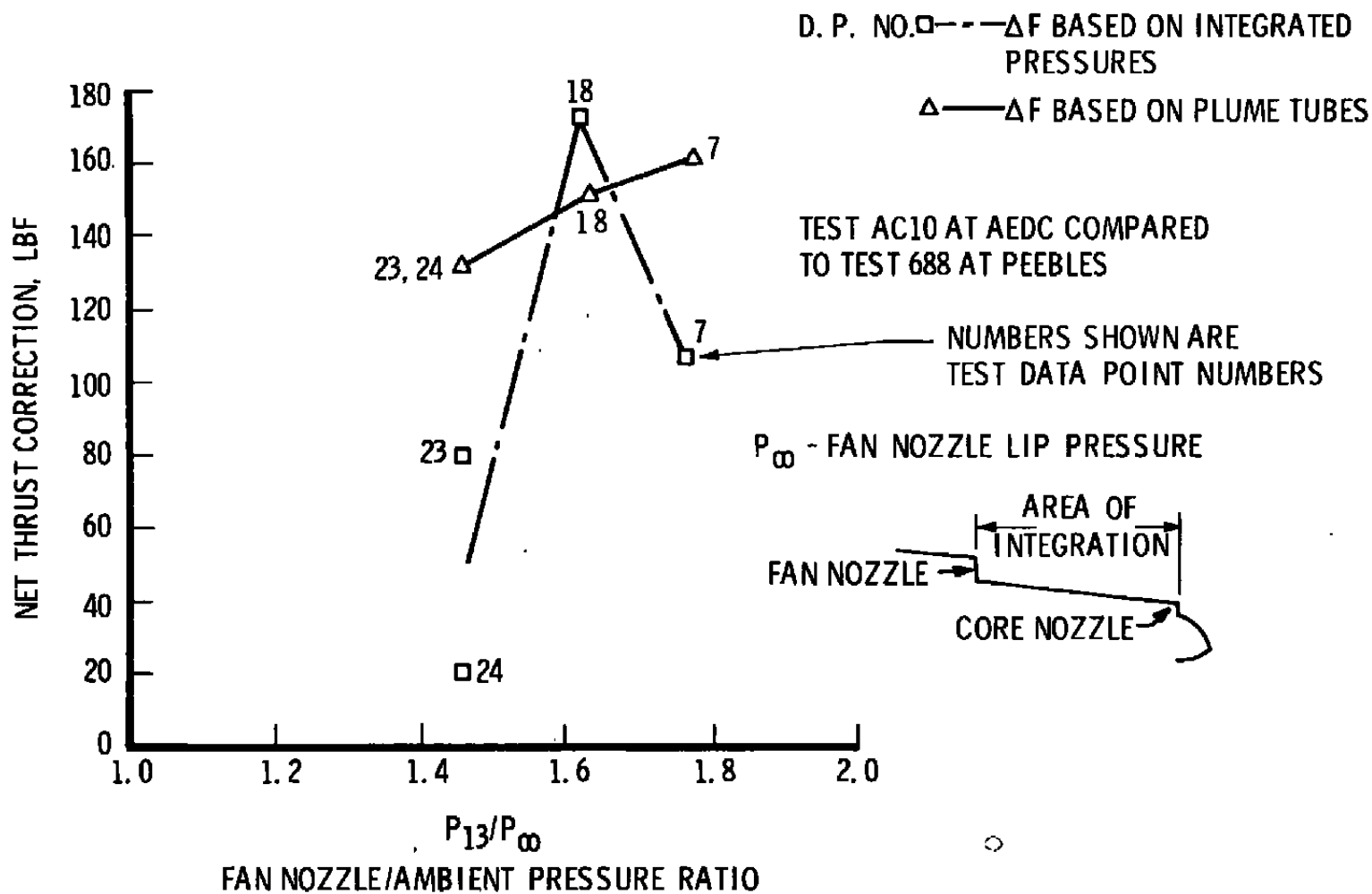


Figure 30. CF6-50 fan cowl net thrust correction versus fan pressure ratio.

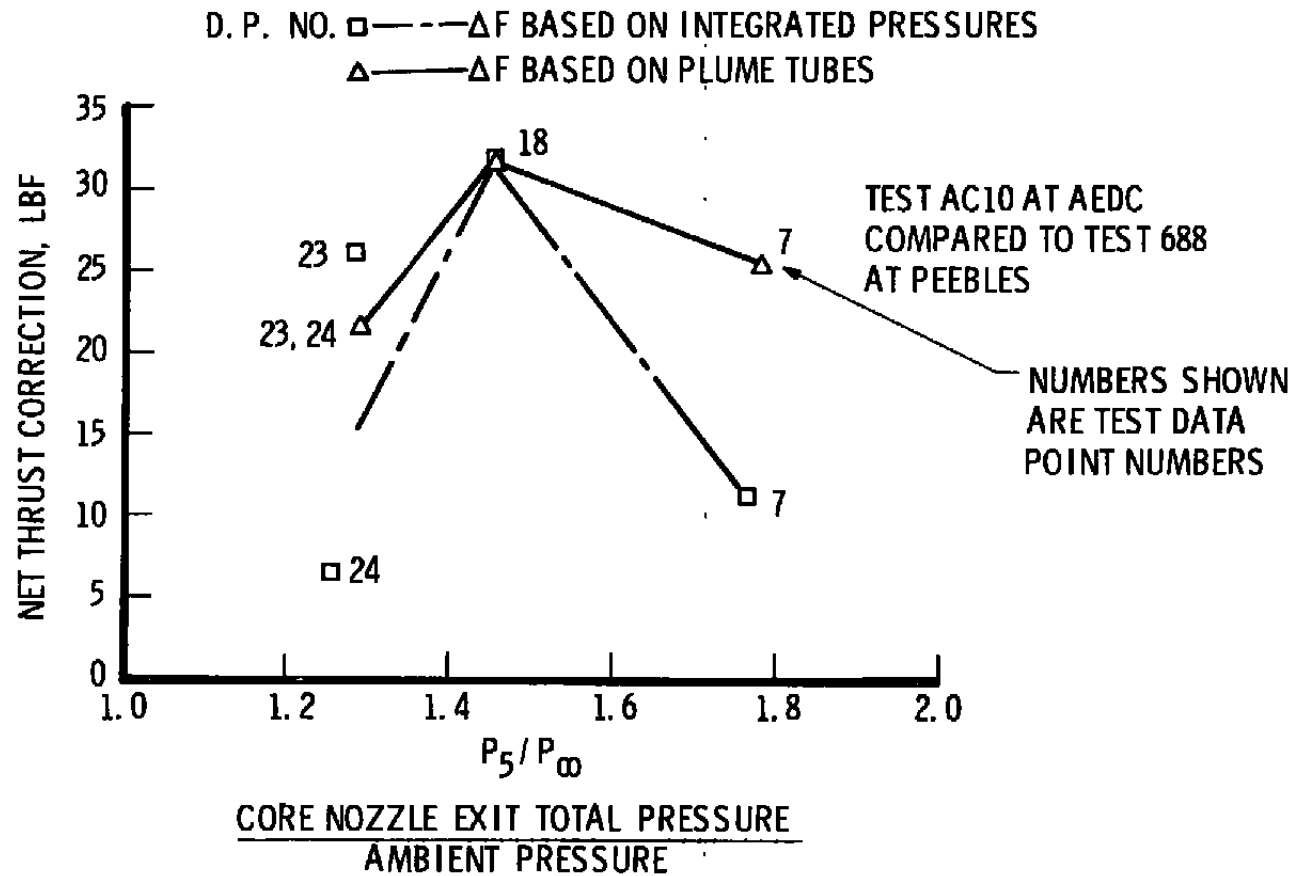
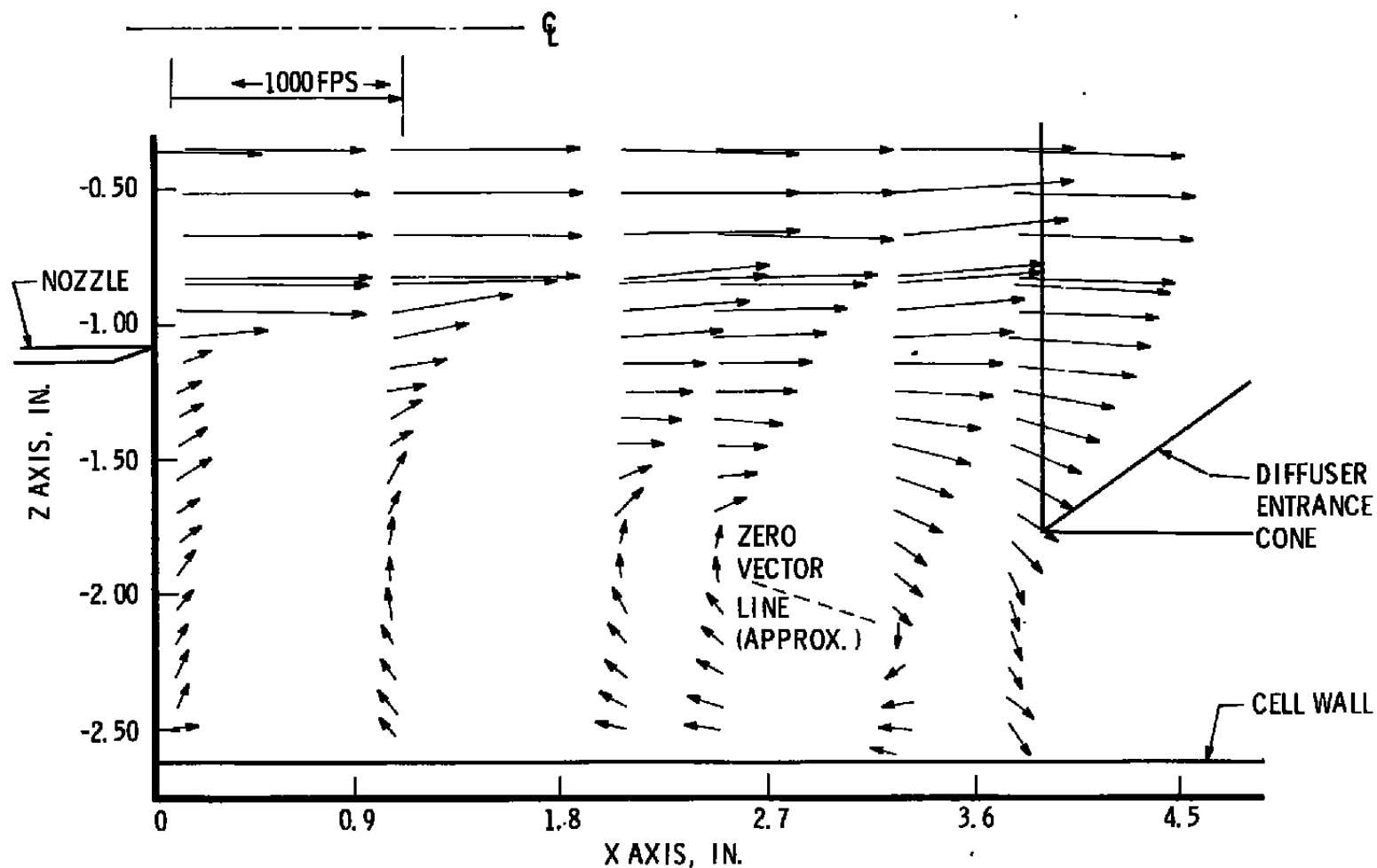
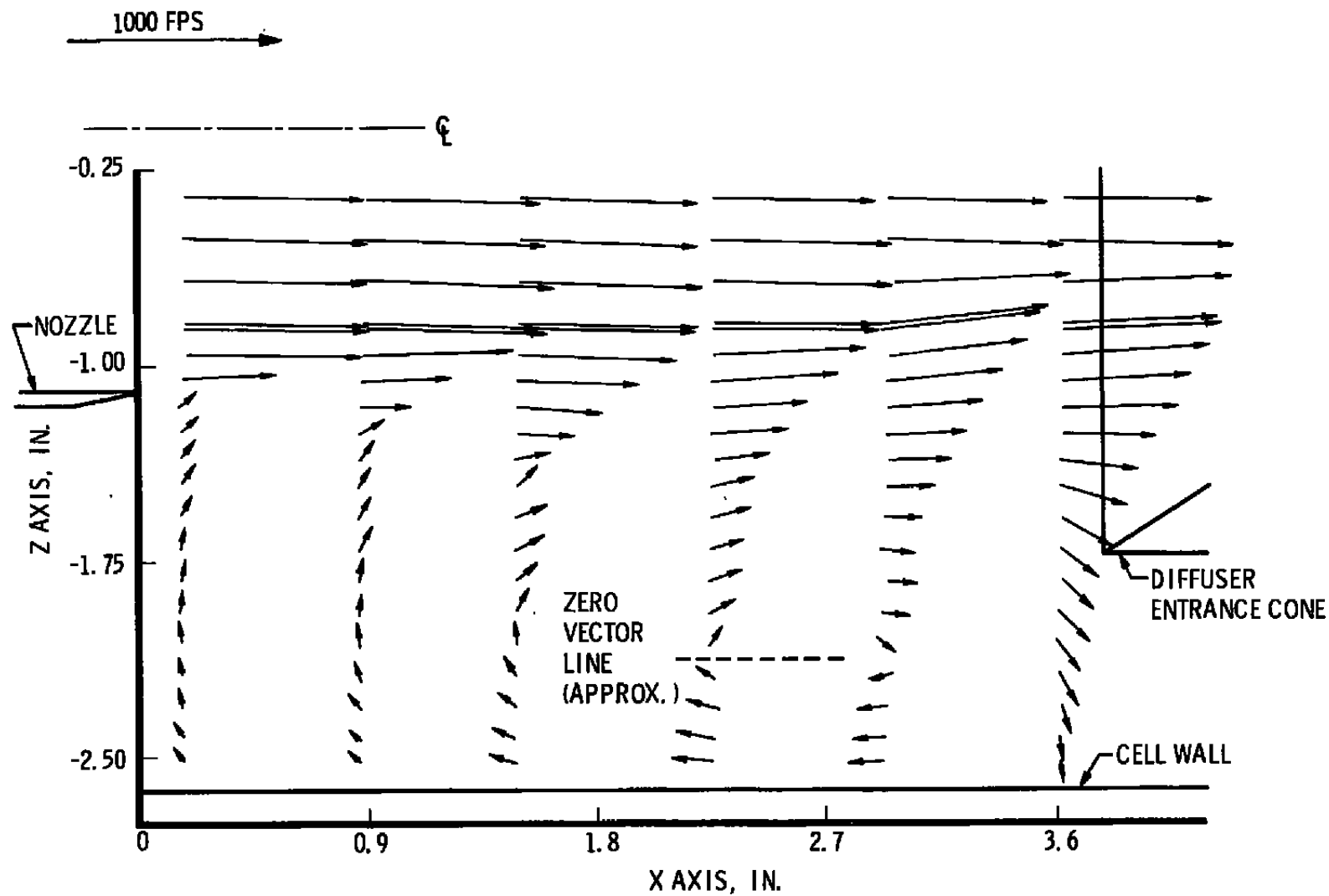


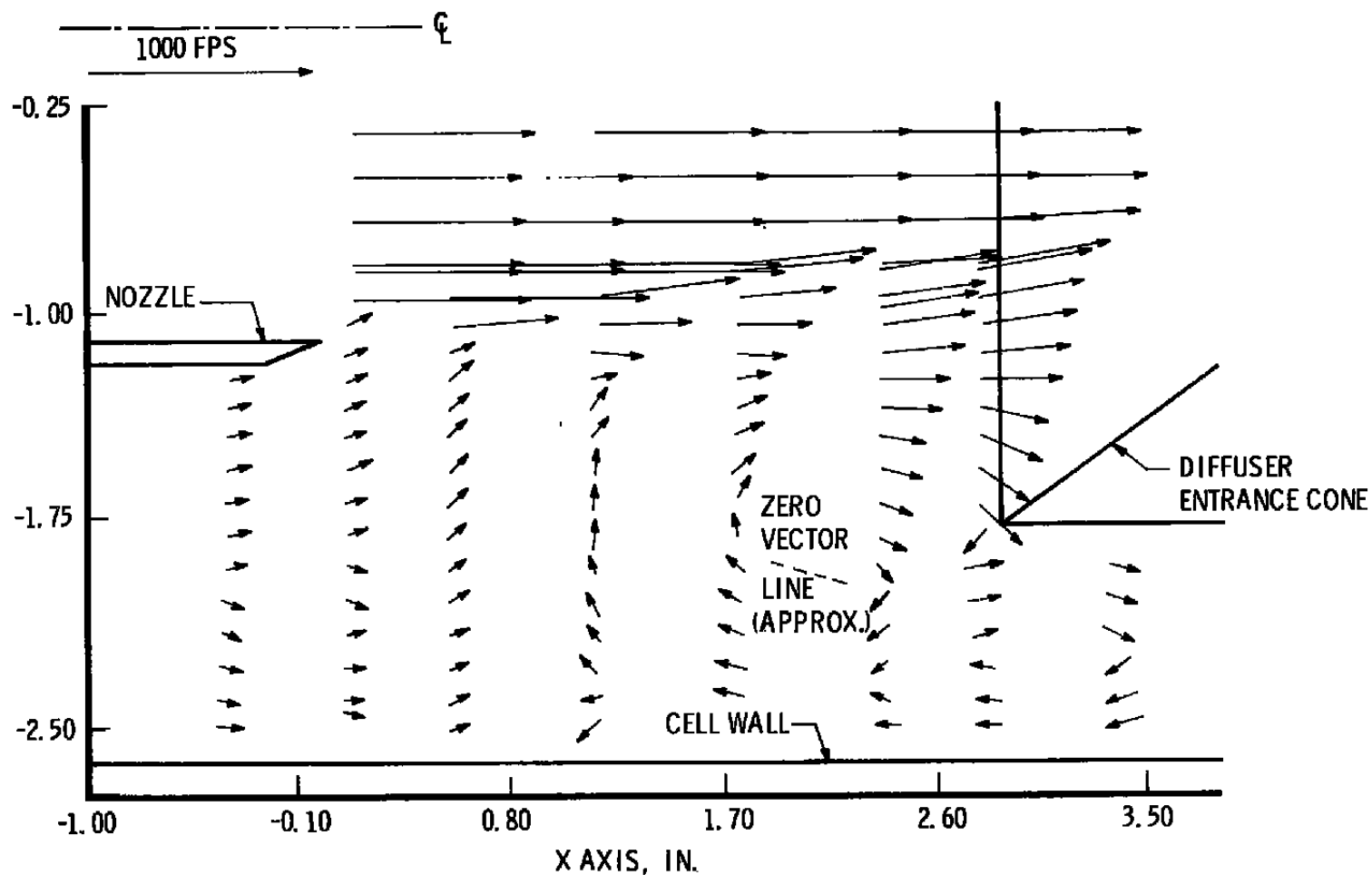
Figure 31. CF6-50 core plug net thrust correction versus core nozzle pressure ratio.



a. Large diffuser (Test Matrix No.1) spacing = 3.88 in.
 Figure 32. AEDC subscale model-axisymmetric (no expansion cone)
 flow-field velocity vectors.



b. Small diffuser (Test Matrix No. 8) spacing = 3.88 in.
Figure 32. Continued.



c. Large diffuser (Test Matrix No. 3) spacing = 2.88 in.
Figure 32. Concluded.

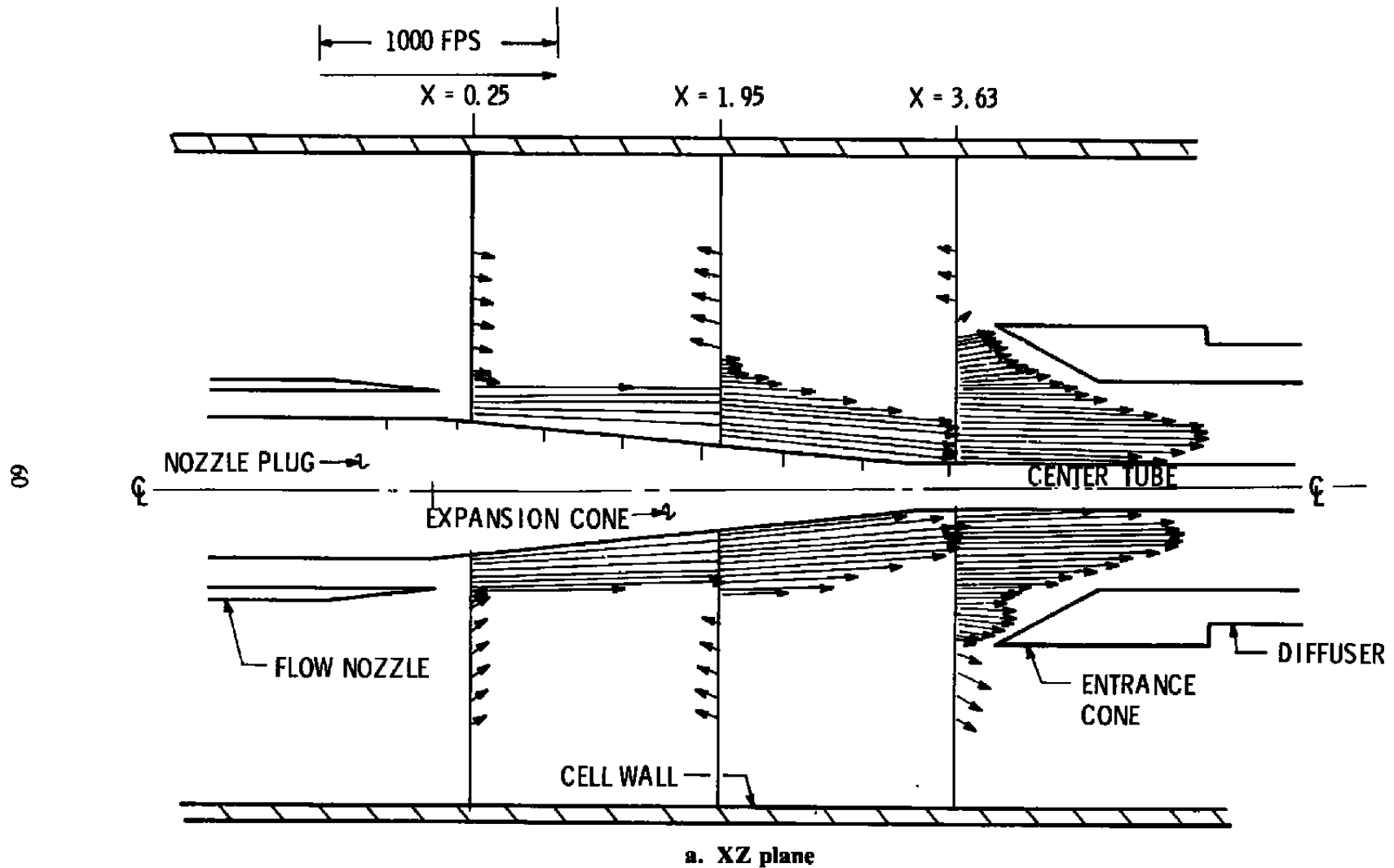
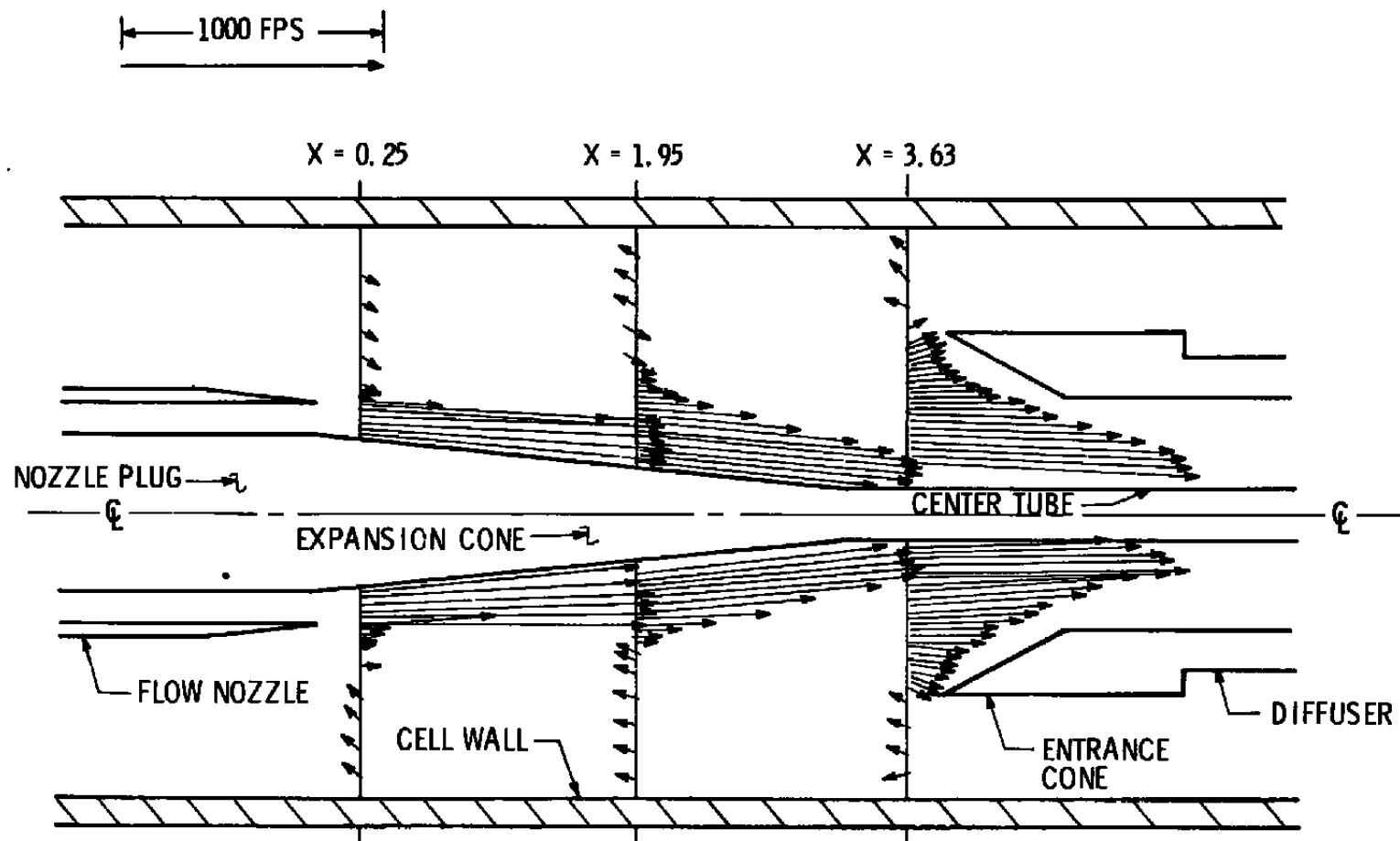
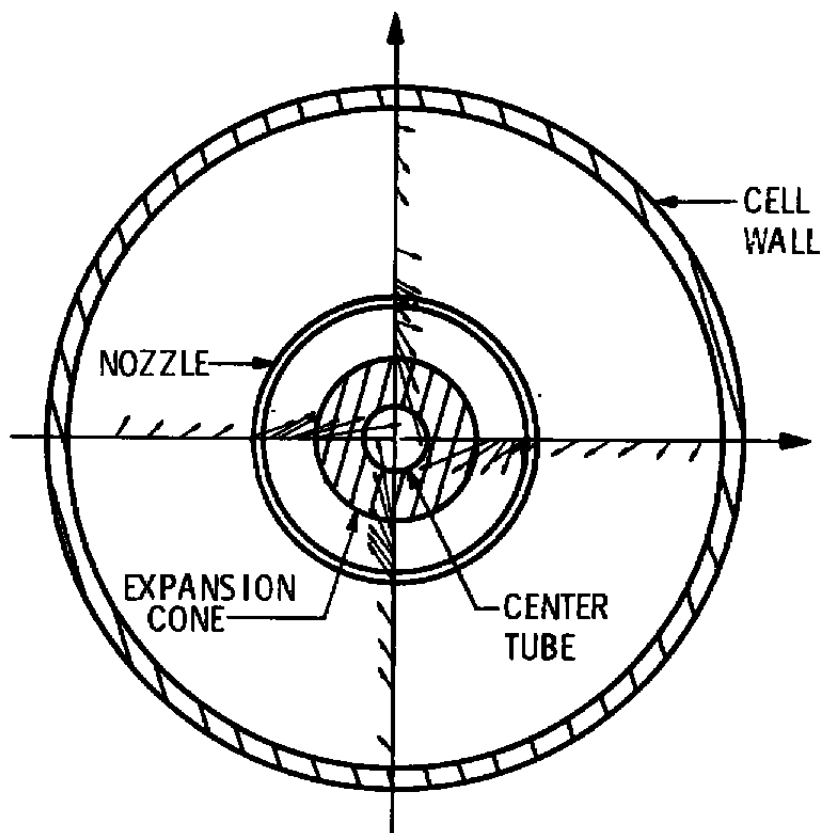


Figure 33. AEDC subscale model-axisymmetric case, $Pt = 10.2$
flow-field velocity vectors.

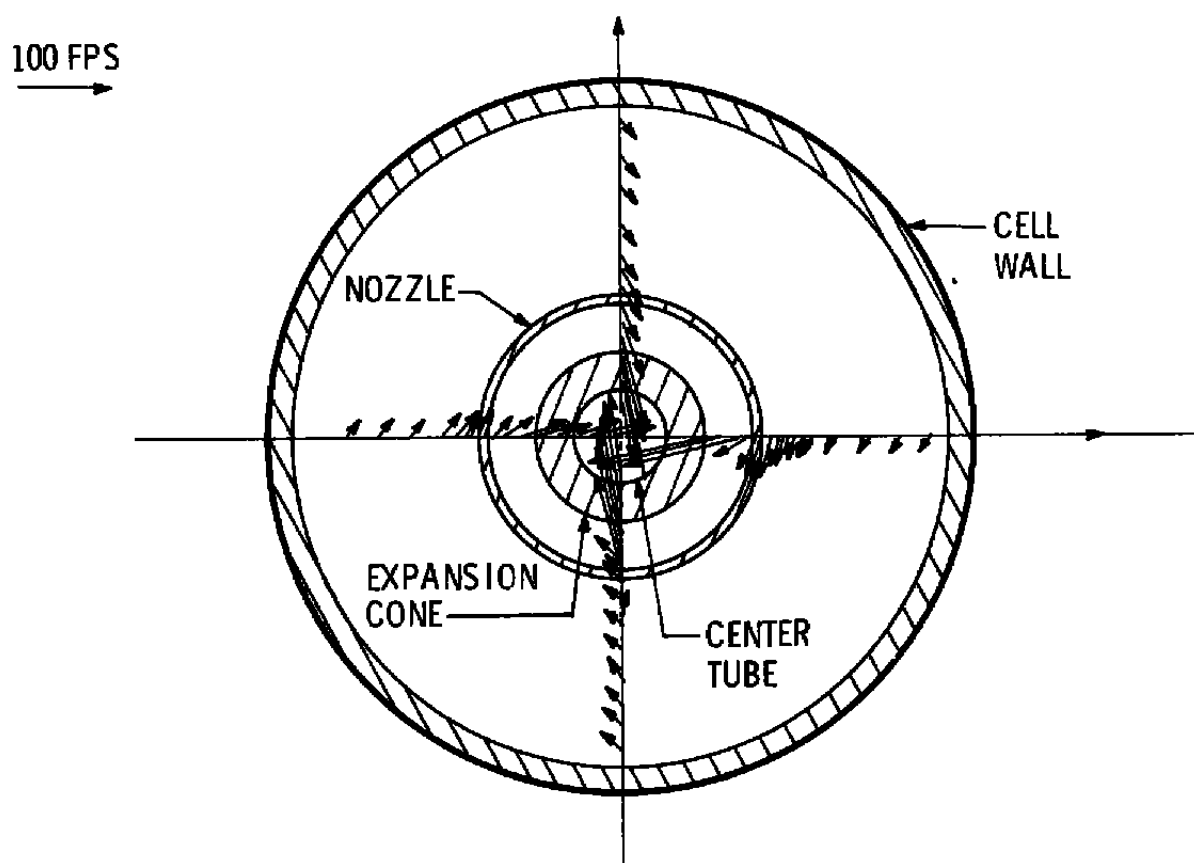


b. XY plane
Figure 33. Continued.

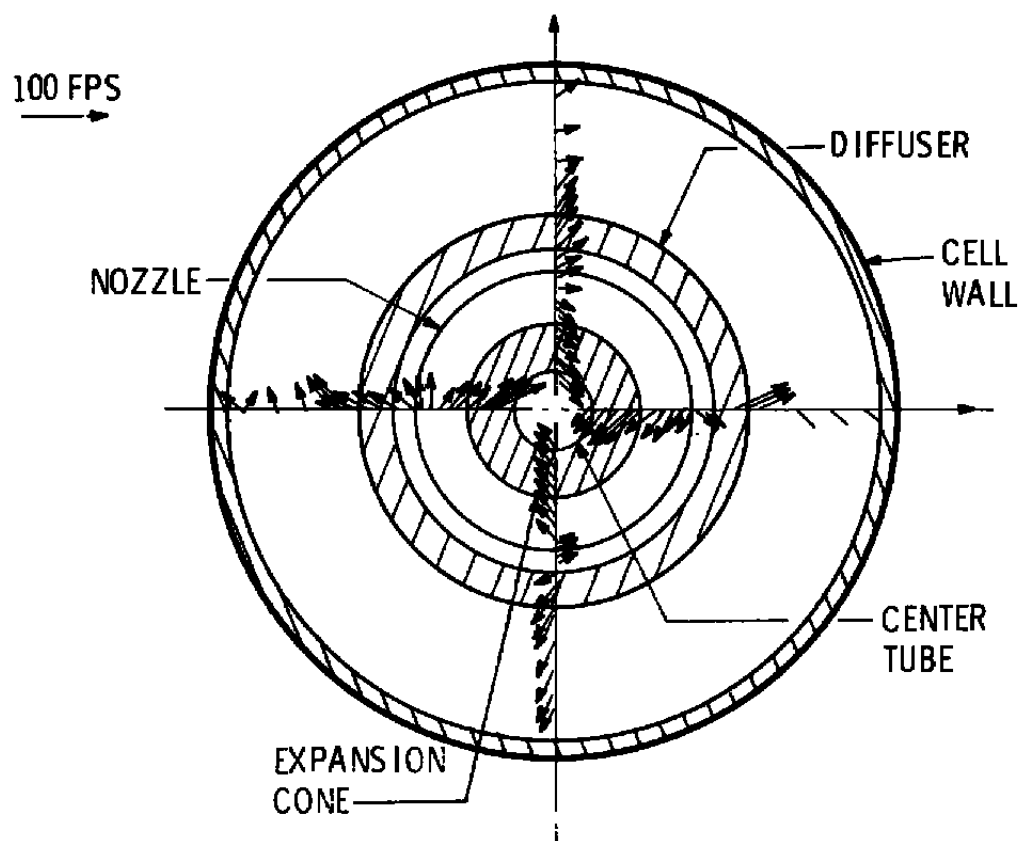
100 FPS
→



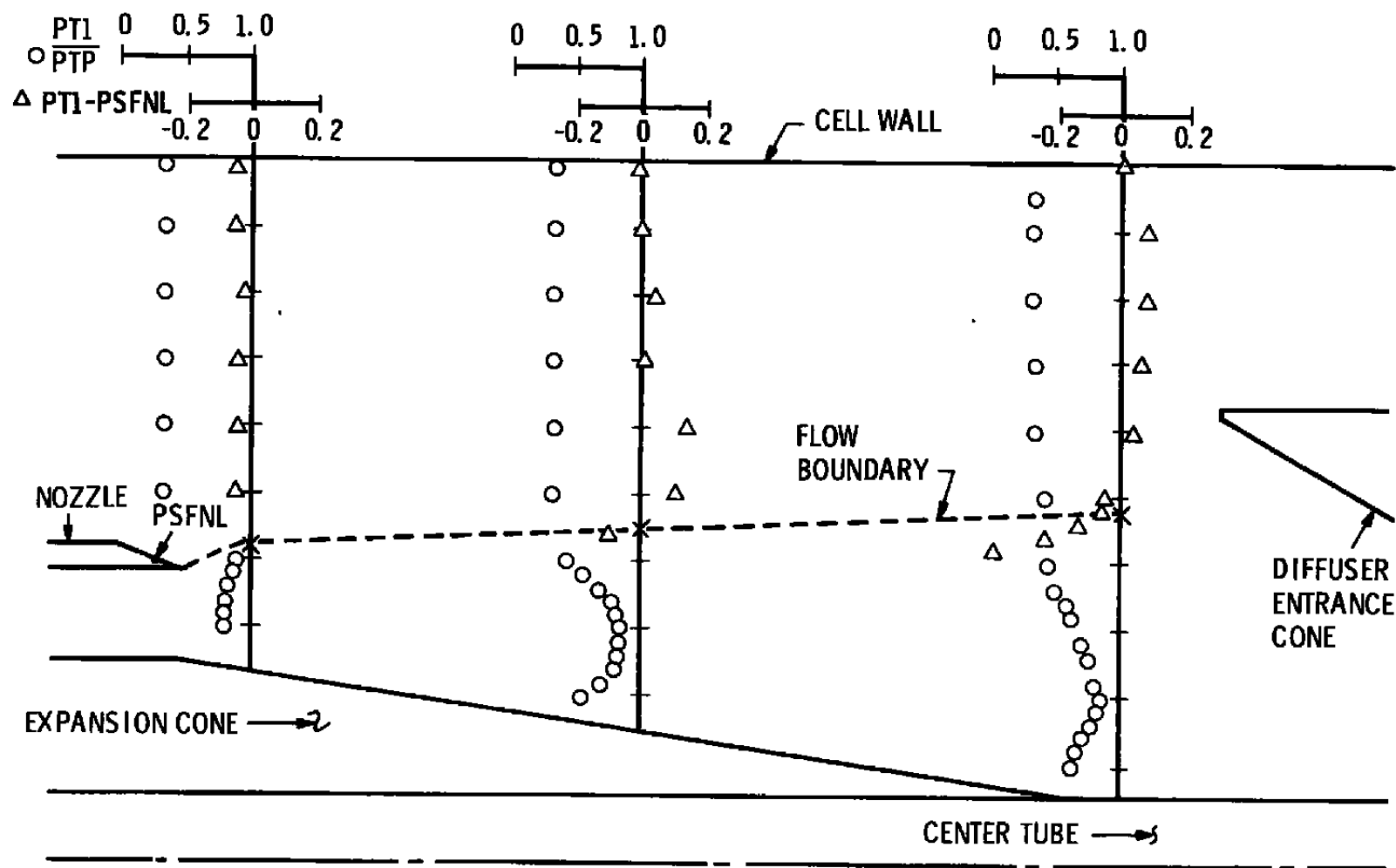
c. Y-Z plane left ($X = 0.25$) plane
Figure 33. Continued.



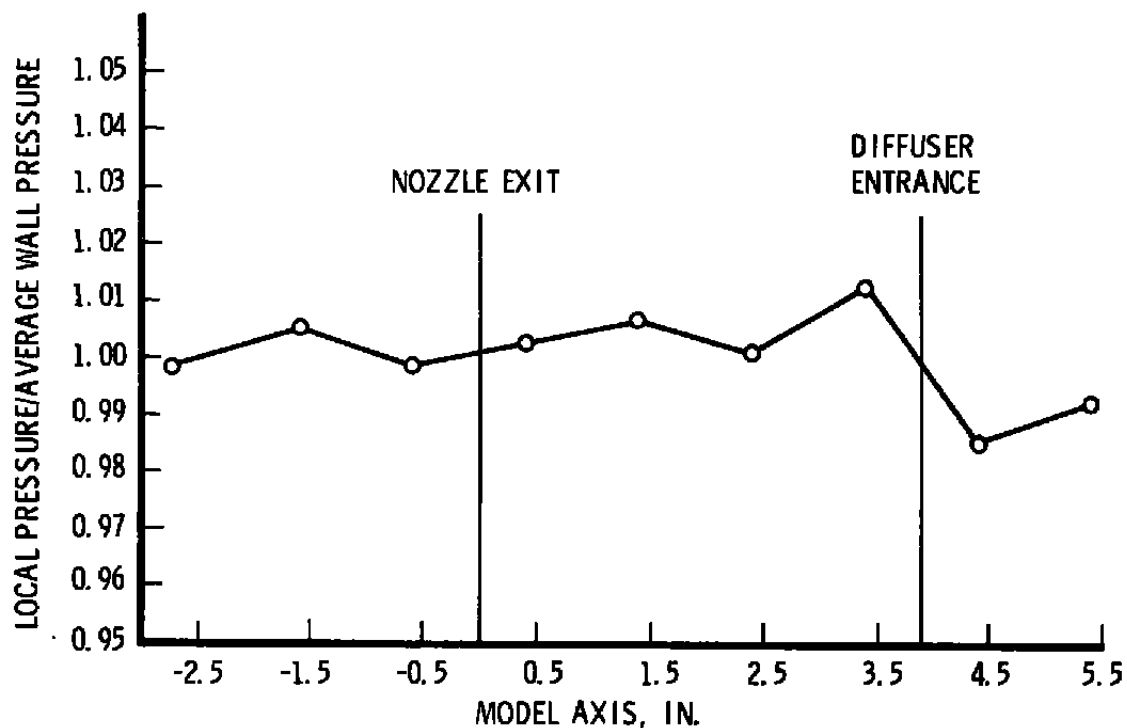
d. Y-Z plane mid ($X = 1.95$) plane
Figure 33. Continued.



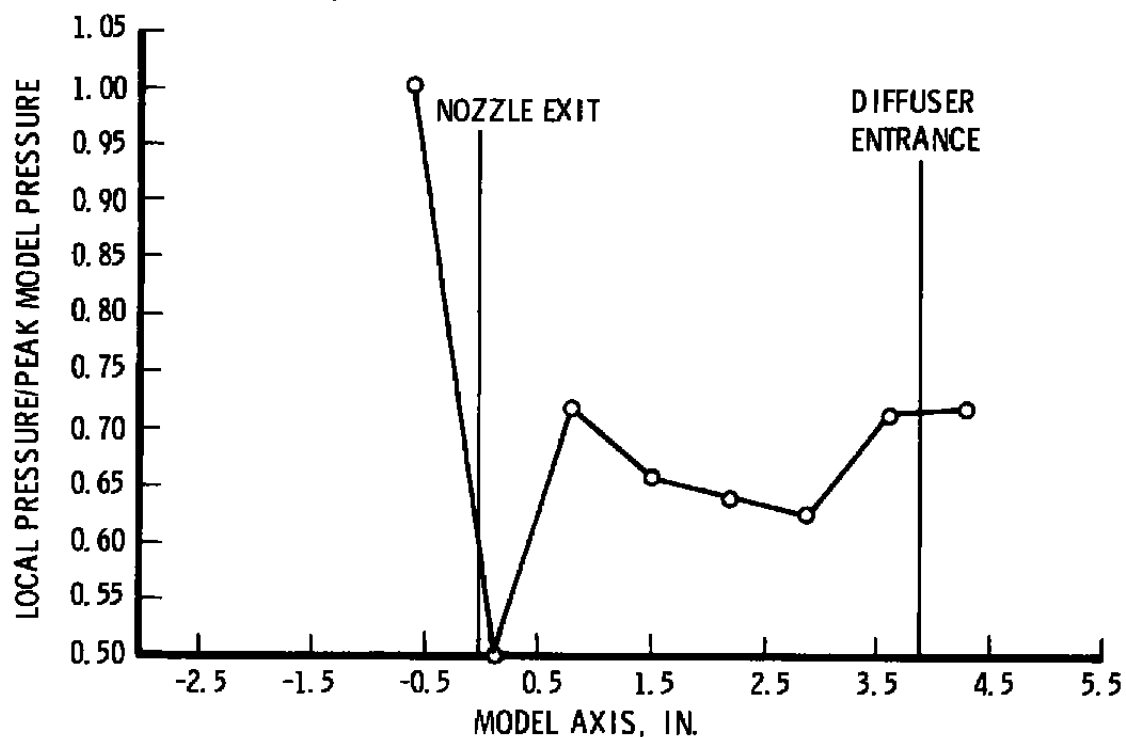
e. YZ plane aft (diffuser entrance) plane
Figure 33. Continued.



f. Total pressure profiles
 Figure 33. Continued.



g. Axial cell wall static pressure profiles



h. Axial model surface static pressure profiles

Figure 33. Concluded.

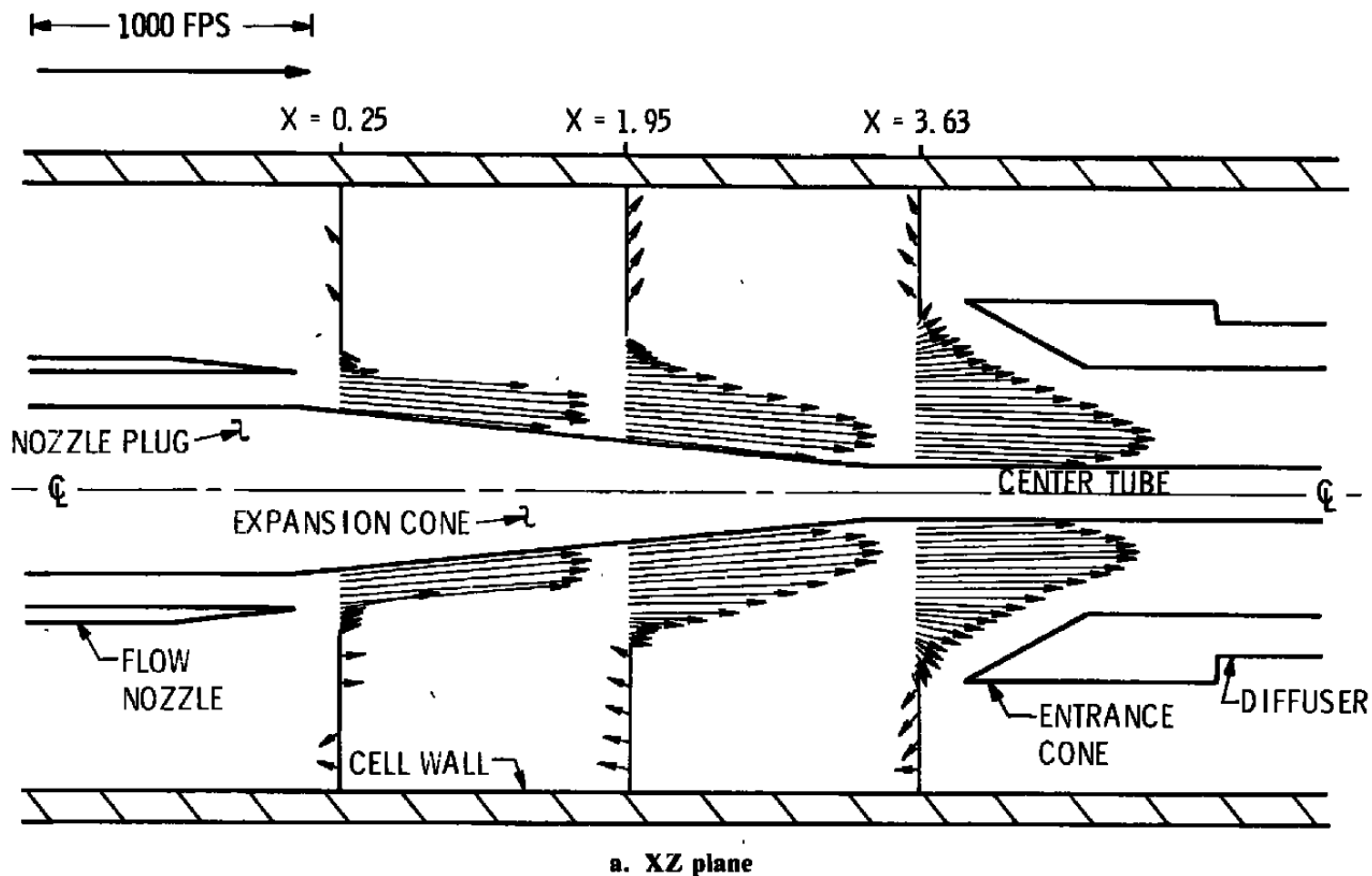
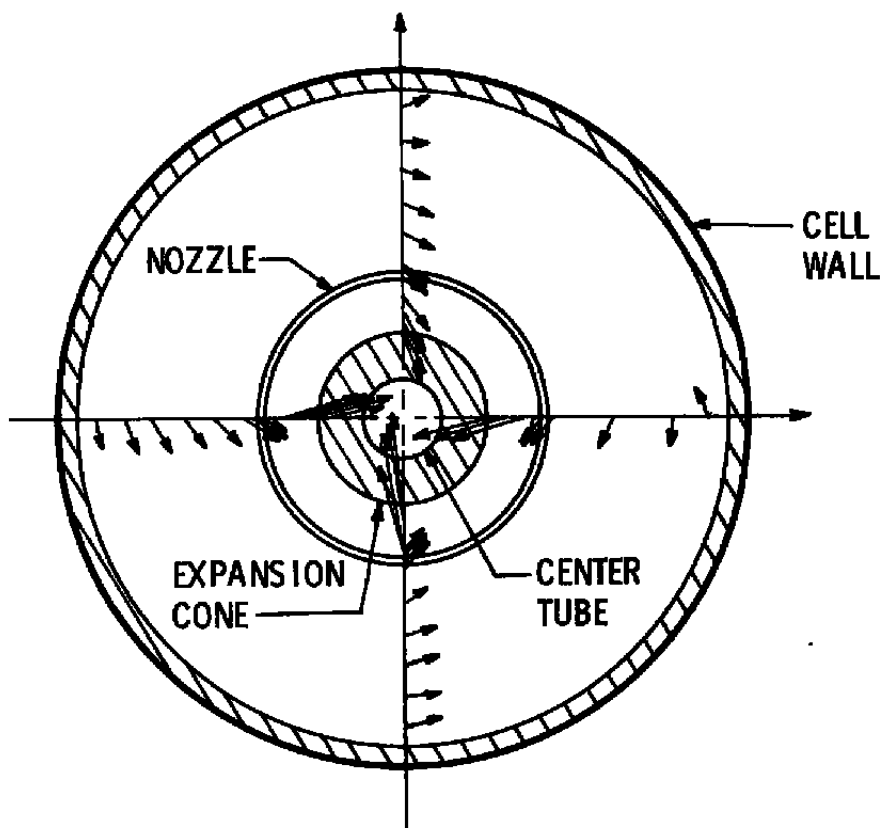
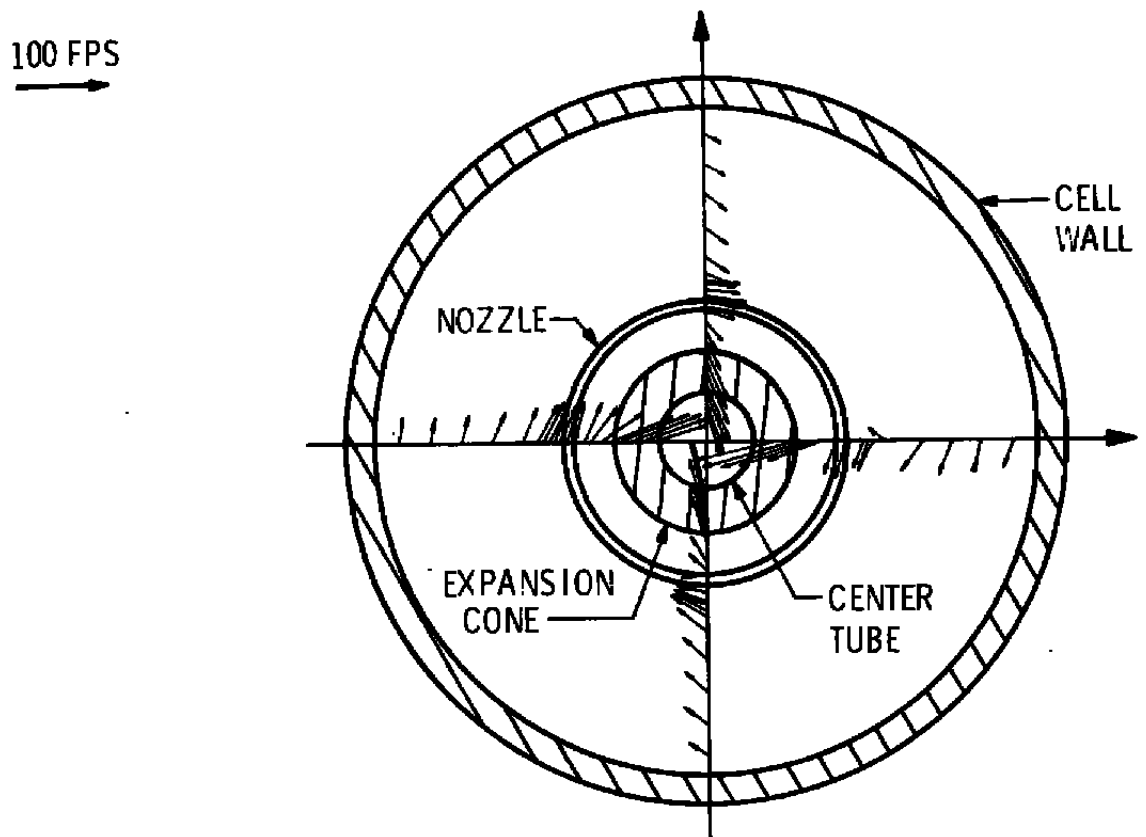


Figure 34. AEDC subscale model-axisymmetric case, $Pt = 19.2$
flow-field velocity vectors.

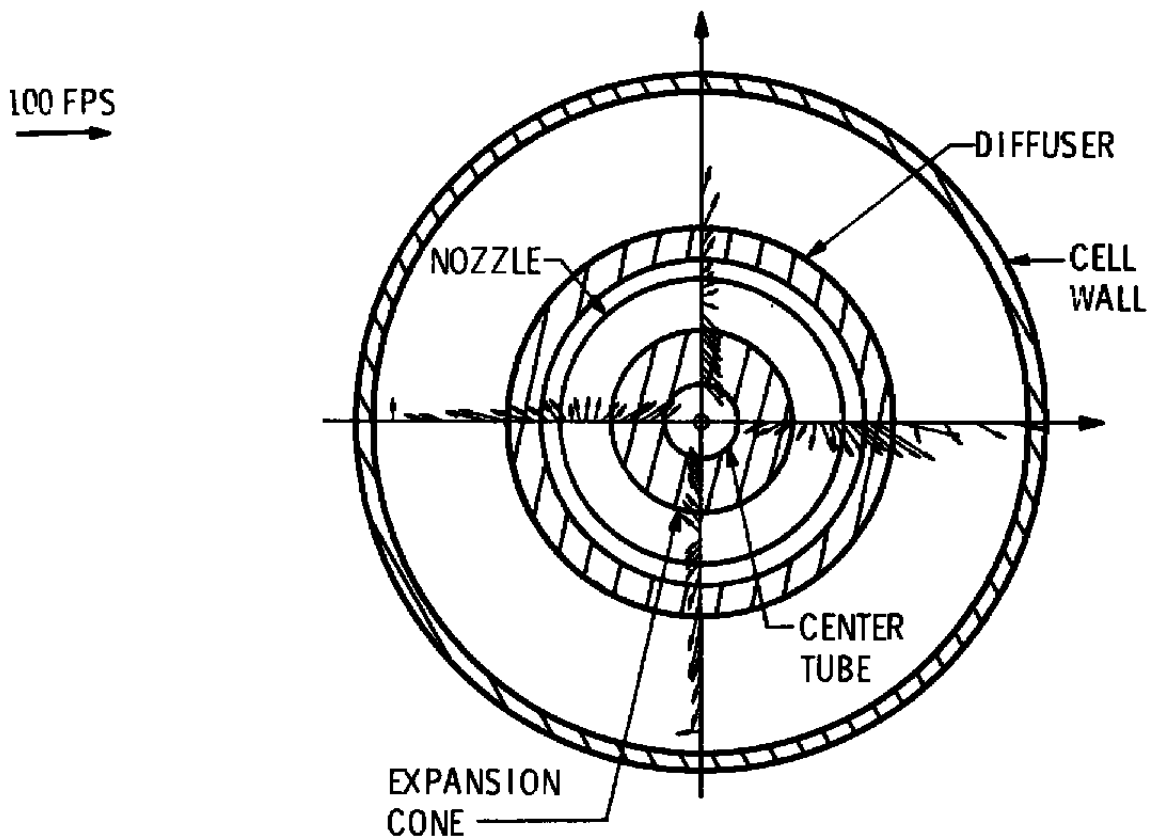
100 FPS
→



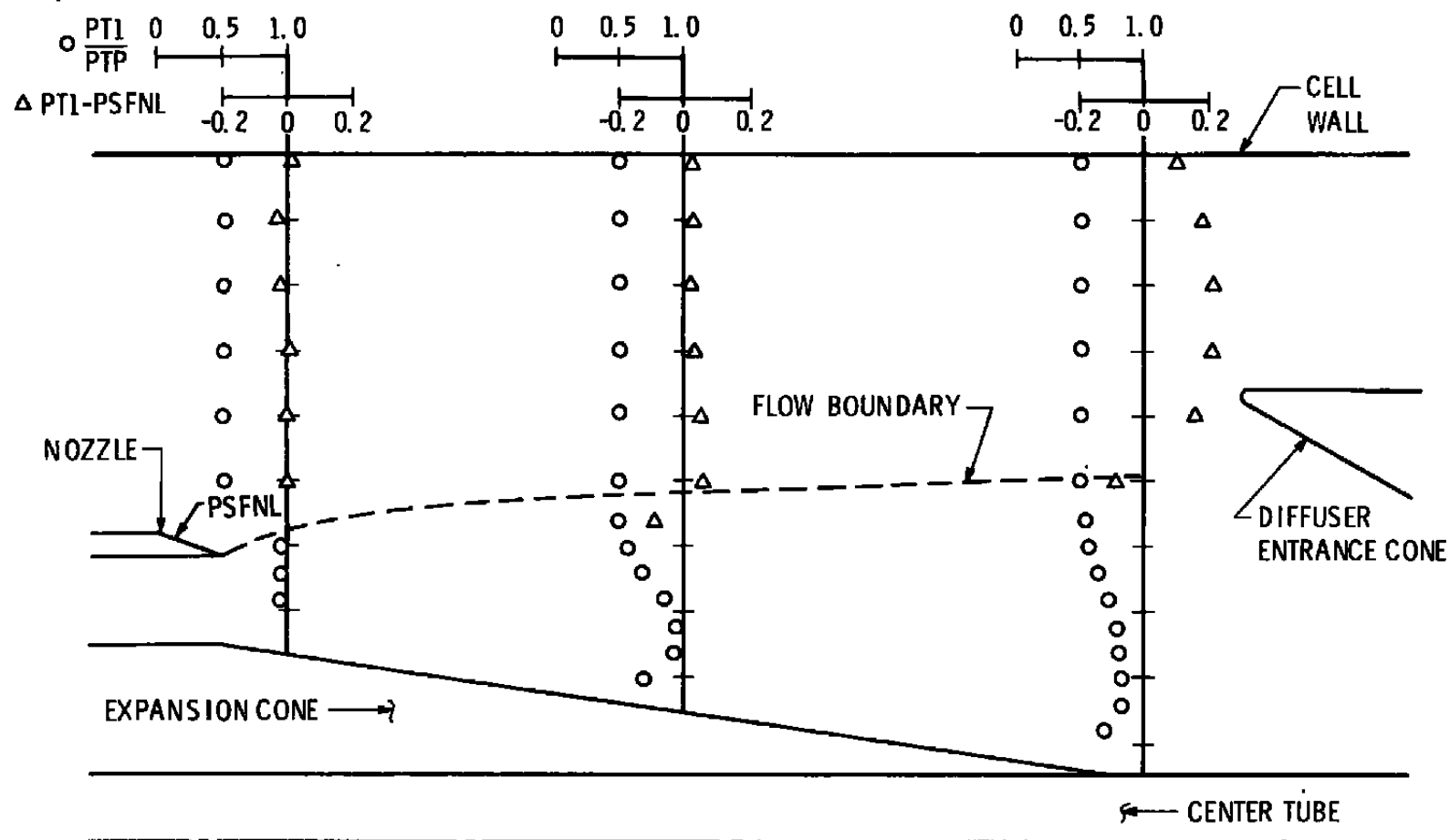
b. YZ plane left ($X = 0.25$) plane
Figure 34. Continued.



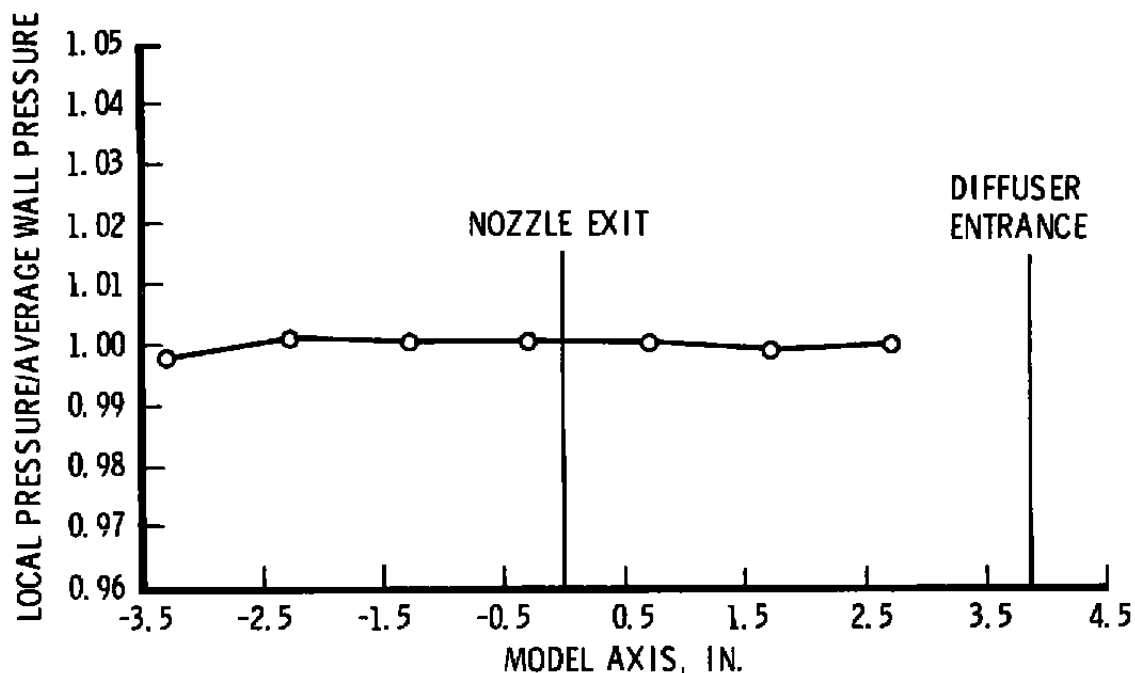
c. YZ middle ($X = 1.95$) plane
Figure 34. Continued.



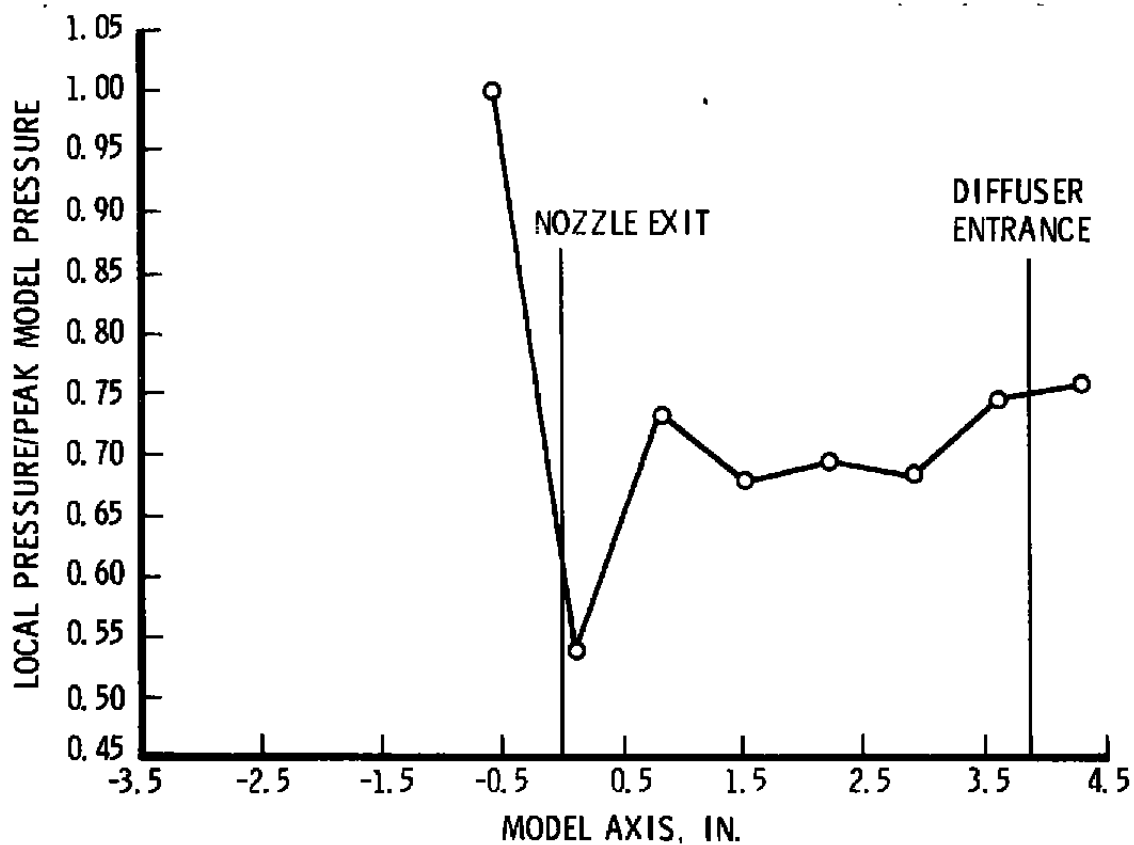
d. Y-Z right ($X = 3.63$) plane
Figure 34. Continued.



e. Total pressure profiles
 Figure 34. Continued.



f. Axial wall static pressure profiles



g. Axial model surface static pressure profiles

Figure 34. Concluded.

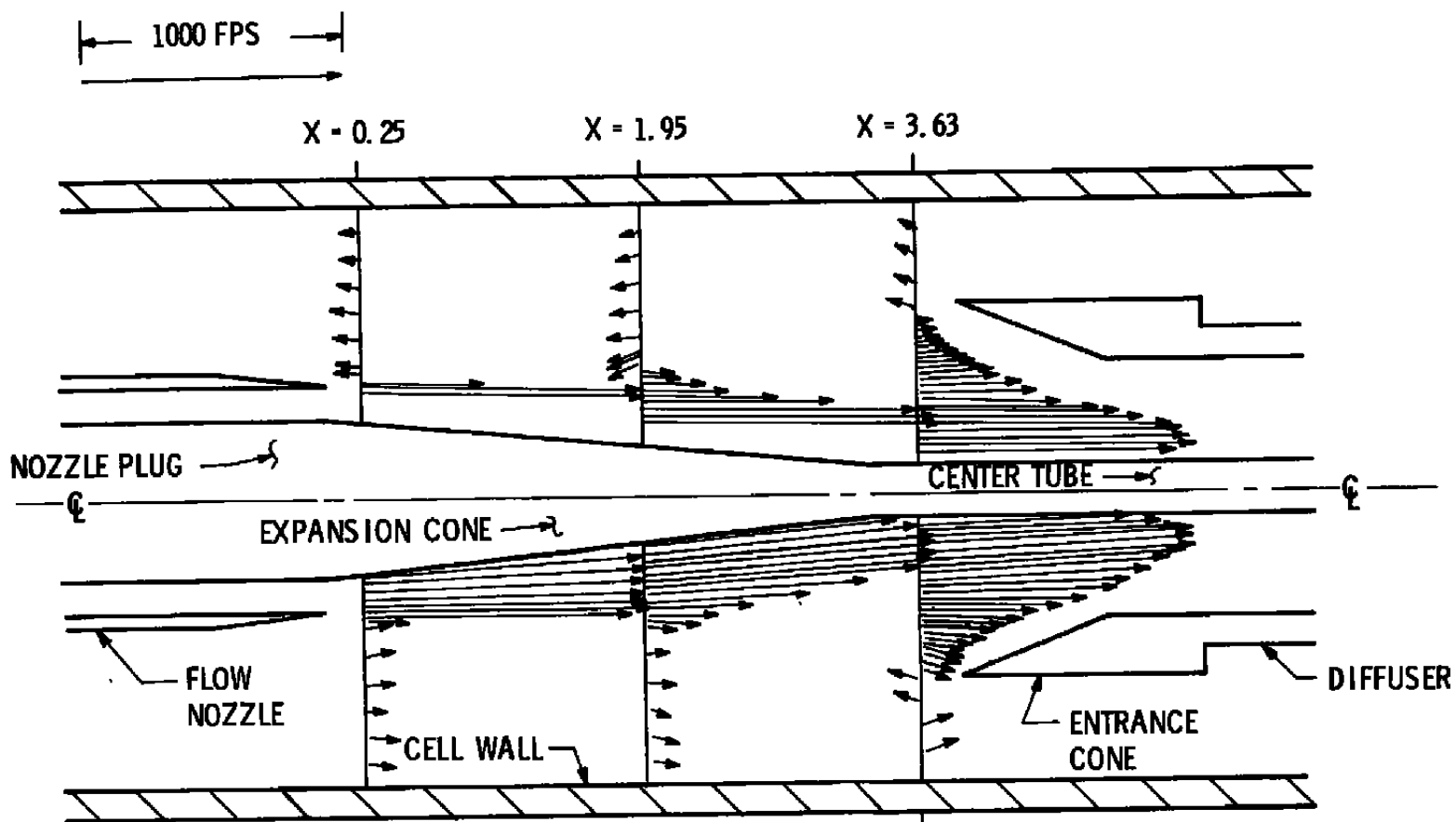
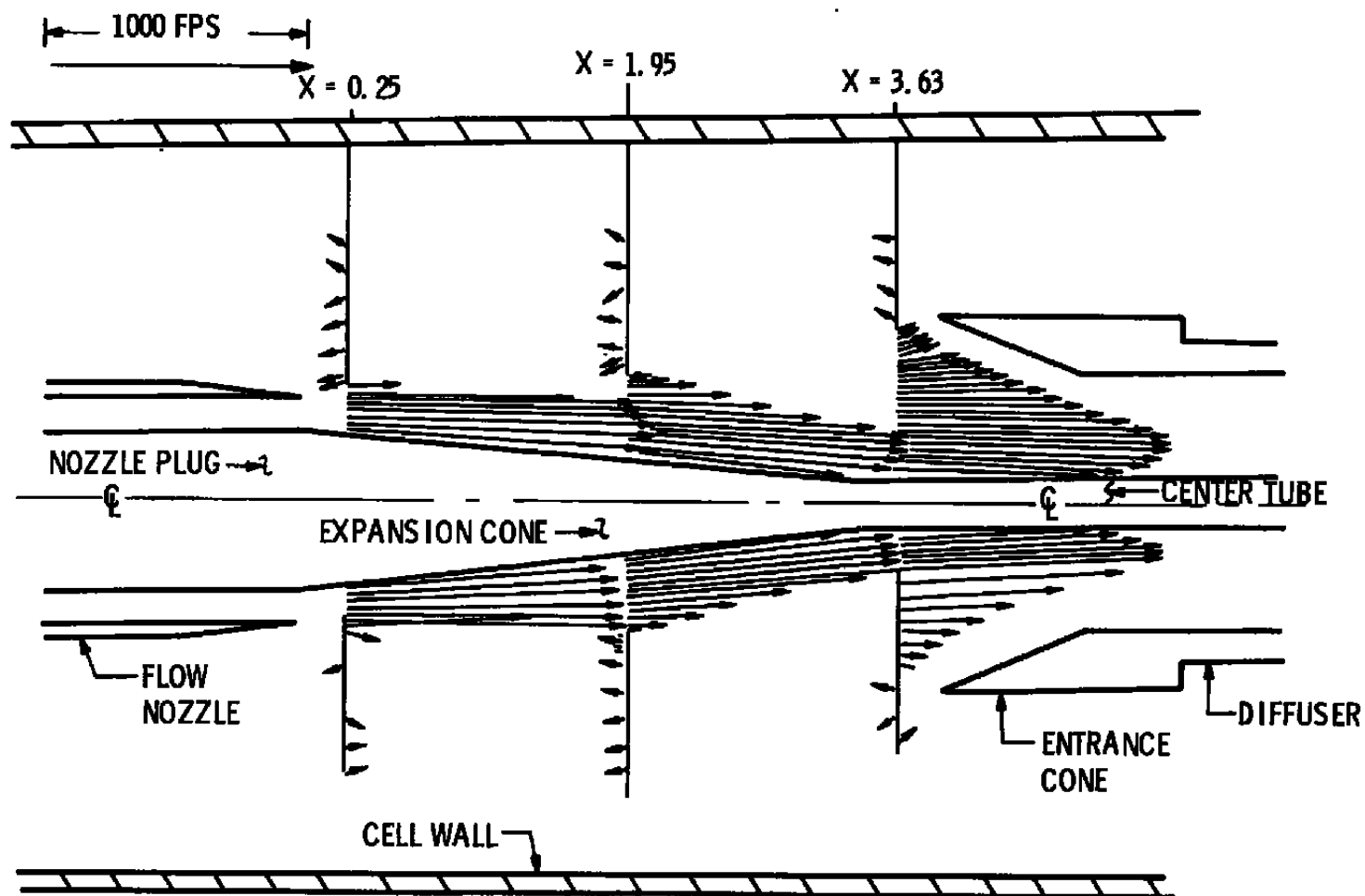
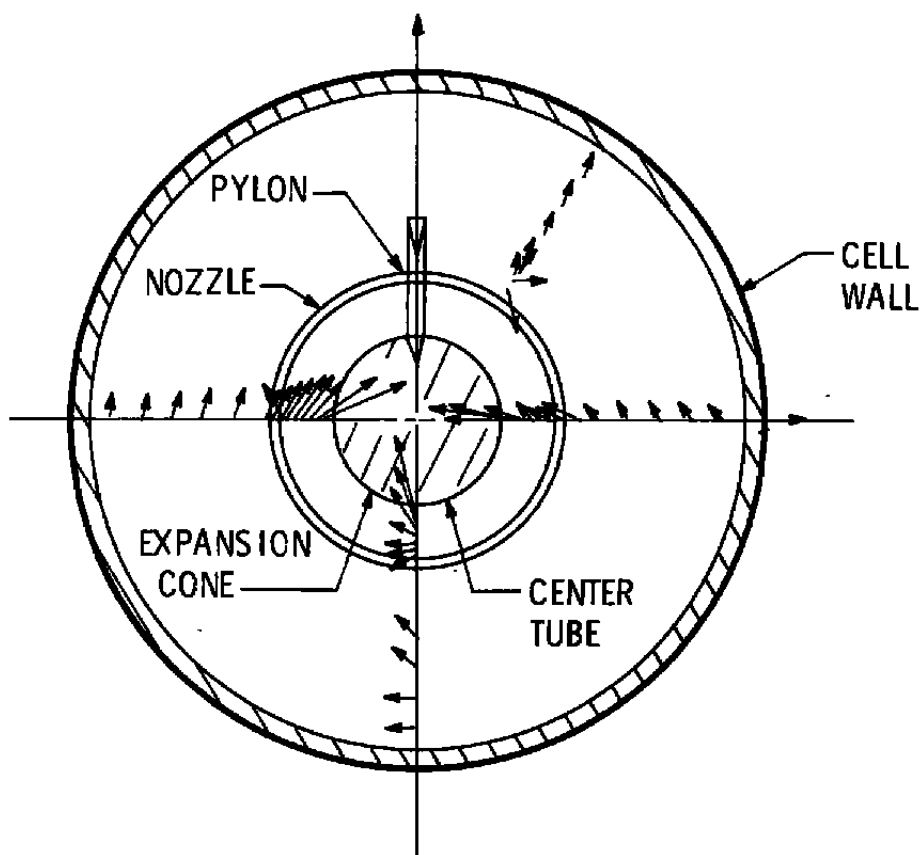


Figure 35. AEDC subscale model-pylon on case, PTP = 10.2
flow-field velocity vectors.



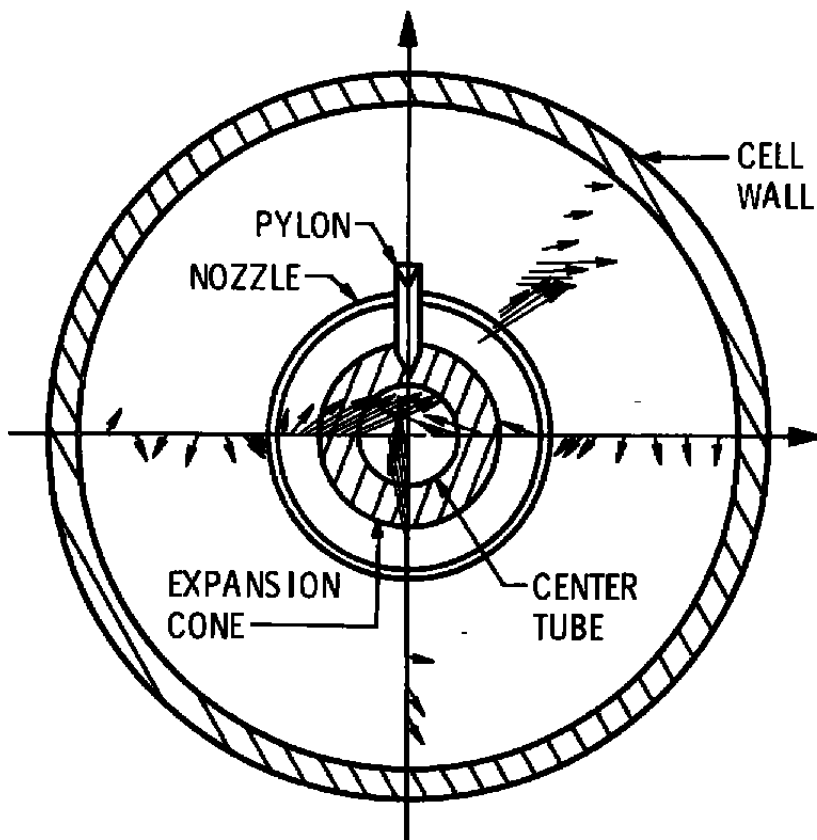
b. XY plane
Figure 35. Continued.

100 FPS
→

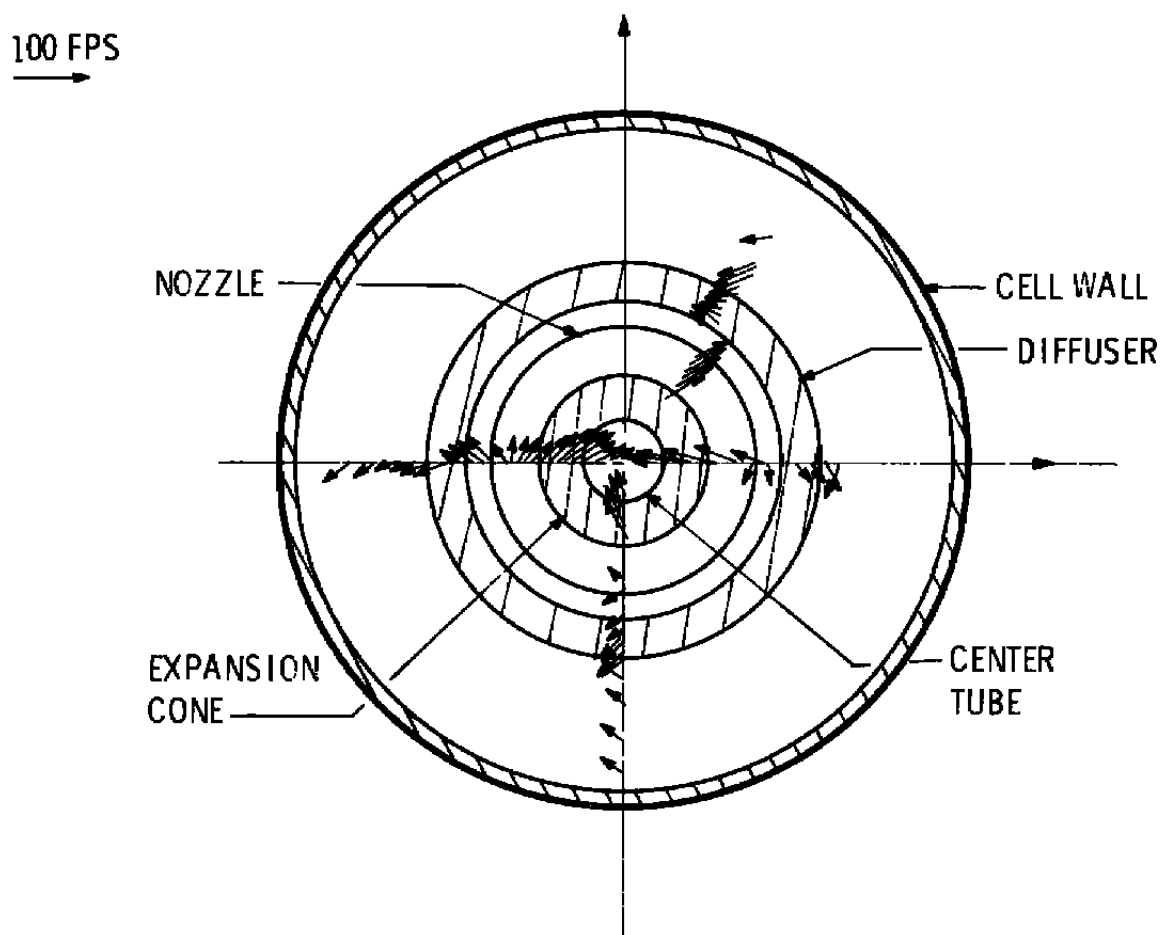


c. YZ left ($X = 0.25$) plane
Figure 35. Continued.

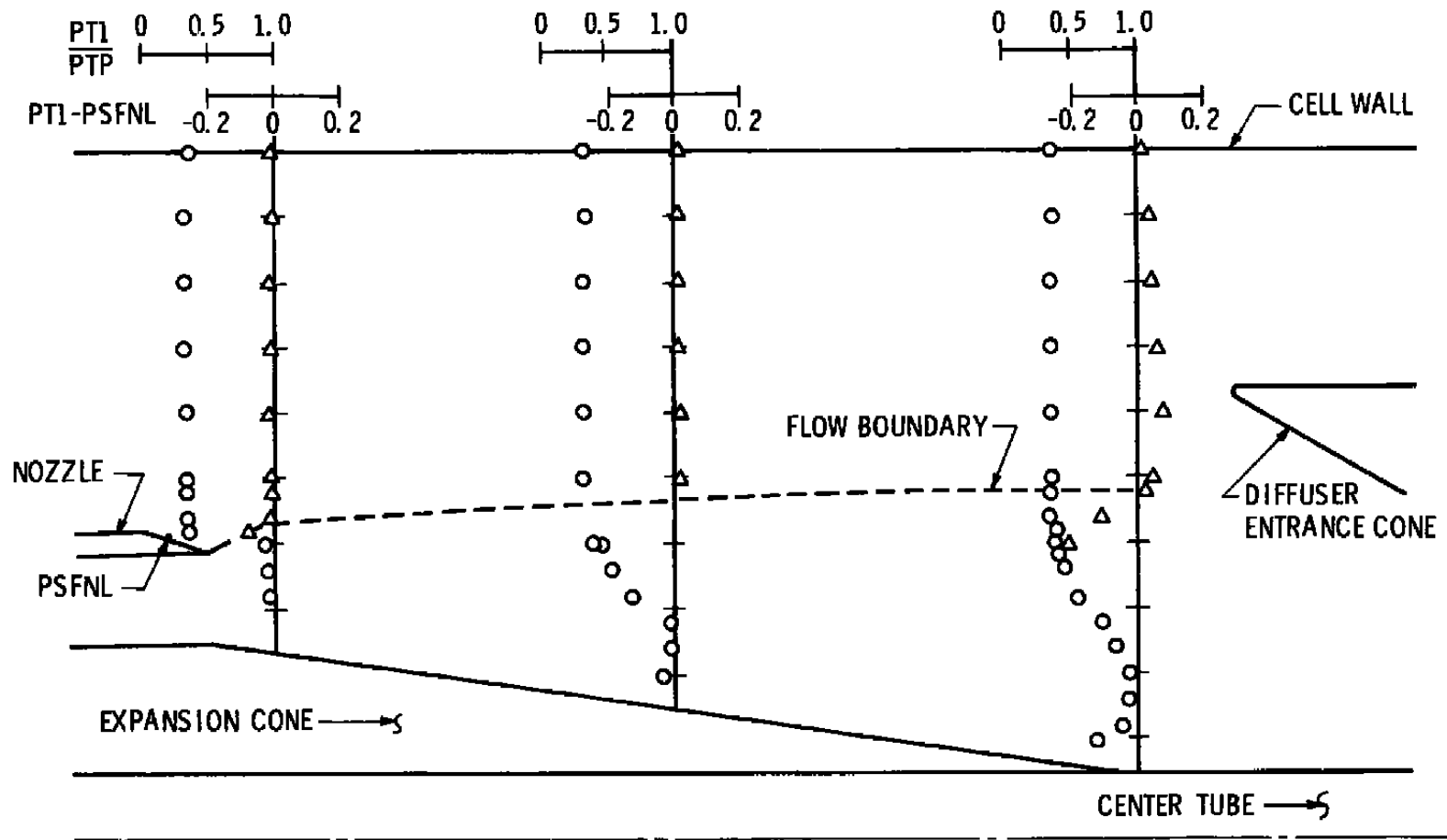
100 FPS
→



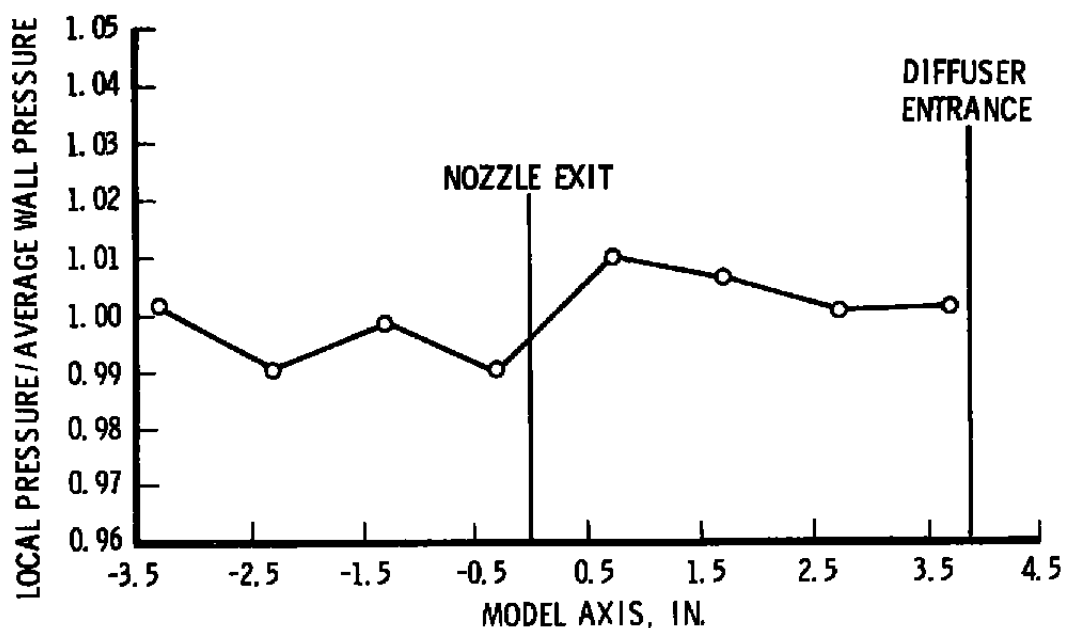
d. YZ middle ($X = 1.95$) plane
Figure 35. Continued.



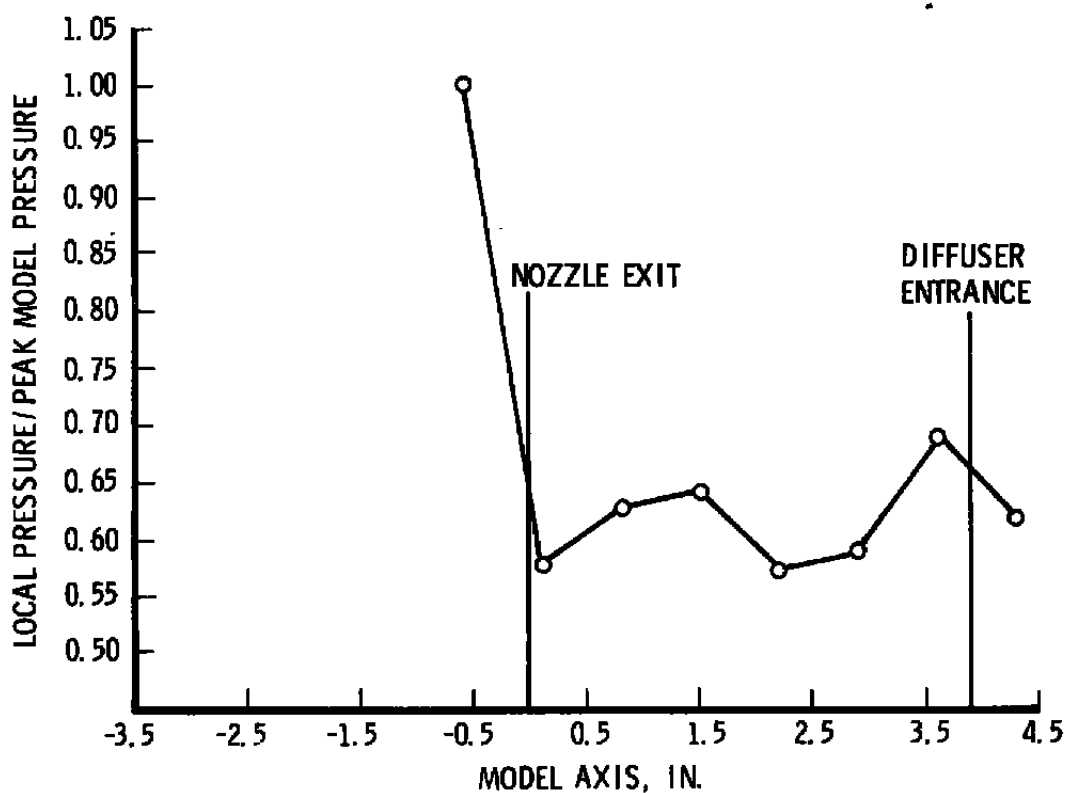
e. YZ right ($X = 3.63$) plane
Figure 35. Continued.



f. Total pressure profiles
Figure 35. Continued.



g. Axial cell wall static pressure profiles



h. Axial model surface static pressure profiles

Figure 35. Concluded.

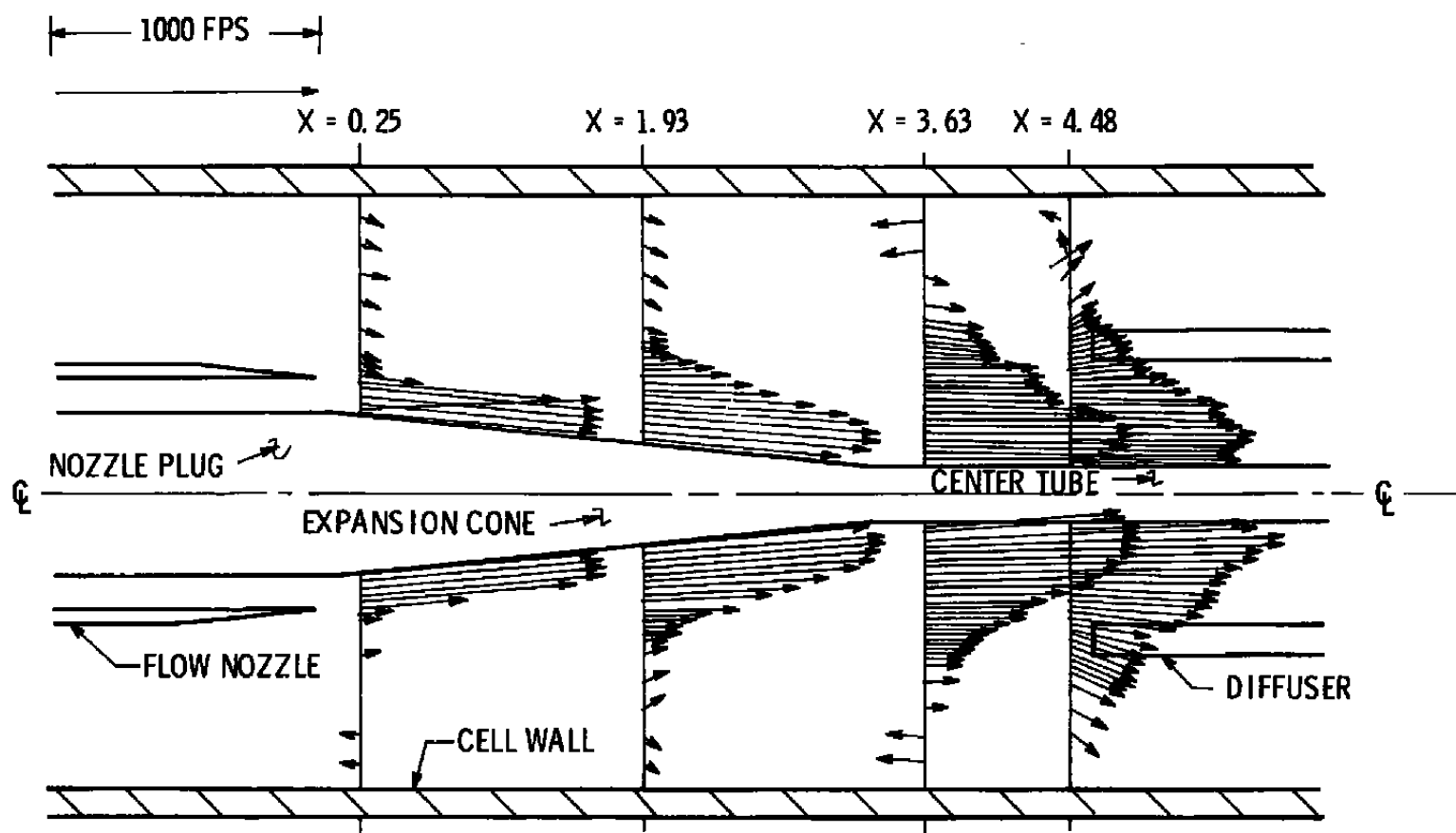


Figure 36. AEDC subscale model-pylon on, entrance cone off, flow-field velocity vectors.

Table 1. Instrumentation
a. Summary

Symbol	Designation	Range	Recorded On
PT1	Probe Total Pressure	5-50 psia	Individual Channel
PSDW1	Diffuser Wall Static Pressure	2-20 psia	Amps
PSDW2			
PSDW3			
PSDW4			
PSDW5			
PSDW6			
PSTS1	Tube Surface Static Pressure		
PSTS2			
PSTS3			
PSTS4			
PSTS5			
PSTS6			
PSTS7			
PSTS8			
PSNW1	Nozzle Wall Static Pressure		
PSNW2			
PSNW3			
PSPS	Supply Plenum Static Pressure		Individual Channel
PSP	Plenum Static Pressure	10-100 psia	
PSED	Exhaust Duct Static Pressure	2-20 psia	

**Table 1. Instrumentation
a. Concluded**

Symbol	Designation	Range	Recorded On
PSCW1	Cell Wall Static Pressure	2-15 psia	Amps
PSCW2	↓	↓	↓
PSCW3			
PSCW4			
PSCW5			
PSCW6	↓	↓	↓
PSVP	Venturi Plenum Static Pressure	50-500 psia	Individual Channel
PSVT	Venturi Throat Static Pressure	25-250 psia	↓
PSFNL	Flow Nozzle Lip Static Pressure	2-20 psia	
PTP	Plenum Total Pressure	3-30 psia	
XPRP	Probe Radial Position	-2.5 + 2.5 in.	
PNAP	Nozzle Assembly Axial Position	0-40 in.	
PTP-1	Plenum Total Pressure	3-30 psia	Amps
PTP-2	↓	↓	↓
PTP-3			
PTP-4	↓	↓	↓
TSAP	Plenum Air Temperature	-50°-200°F	Individual Channel
TSVA	Venturi Air Temperature	↓	↓
TSSA	Secondary Air Temperature	↓	↓
PSDAU	Upstream Sec Air Orifice Pressure	7-70 psia	
PSDAD	Downstream Sec Air Orifice Pressure	↓	↓
PSCW7	Cell Wall Static Pressure	2-15 psia	Amps
PSCW8	↓	↓	↓
PSCW9	↓	↓	↓

**Table 1. Instrumentation
b. Uncertainties**

Parameter Designation	Steady State							Range		Type of Measuring Device	Type of Recording Device	Method of System Calibration
	Precision Index (S)			Bias (B)		Uncertainty** ± (B + 1.95(S))						
	Percent of Reading	Unit of Measurement	Degree of Freedom	Percent of Reading	Unit of Measurement	Percent of Reading	Unit of Measurement	Amplitude	Frequency			
PT-1	0.15	psia		1.056	psia	1.356	psia	5 to 50 psia	≤ to 10 Hz	Bonded Strain-Gage-Type Pressure Transducer.	Sequential Sampling, Milli-volt-to-Digital Converter and Magnetic Tape Storage Data Acquisition System.	Resistance Shunt Based on the Standards Laboratory Determination of Transducer Applied Sensitivity for Applied Pressure versus Resistance Shunt Equivalent Pressure Relationship.
PT-1	0.10	psia		0.71	psia	0.91	psia	10 to 50 psia	≤ to 10 Hz			
PT-1	0.15	psia		1.056	psia	1.356	psia	5 to 50 psia	≤ to 10 Hz			
PSDW-1-6 PSDW-1-3 PSCW-1-9	0.15	psia		1.060	psia	1.36	psia	2 to 20 psia	≤ to 10 Hz			
PSDW-1-6 PSDW-1-3 PSCW-1-9	0.10	psia		0.717	psia	0.917	psia	4 to 20 psia	≤ to 10 Hz			
PSDW-1-6 PSDW-1-3 PSCW-1-9	0.15	psia		1.060	psia	1.36	psia	2 to 4 psia	≤ to 10 Hz			
PSCW-1-9 PSFNL	0.15	psia		1.063	psia	1.363	psia	1.5 to 15 psia	≤ to 10 Hz			
PSCW-1-9 PSFNL	0.10	psia		0.733	psia	0.933	psia	3 to 15 psia	≤ to 10 Hz			
PSCW-1-9 PSFNL	0.15	psia		1.063	psia	1.363	psia	1.5 to 3 psia	≤ to 10 Hz			
PTP	0.15	psia		1.058	psia	1.358	psia	3 to 30 psia	≤ to 10 Hz			
PTP	0.1	psia		0.713	psia	0.913	psia	6 to 30 psia	≤ to 10 Hz			
PTP	0.15	psia		1.058	psia	1.358	psia	3 to 6 psia	≤ to 10 Hz			
XPRP	0.15	in.		1.25	in.	1.55	in.	± 2.5 in.	≤ to 10 Hz	Rotary Potentiometer Transducer		In-place Measurement of Physical Dimensions versus Transducer Output for Each Test
XNAP	0.15	in.		0.10	in.	0.45	in.	0 to +40	≤ to 10 Hz			

* REFERENCE: Thompson, J. W. and Abernethy, R. B. et al. "Handbook Uncertainty in Gas Turbine Measurements." AEDC-TR-73-5, February 1973.

** U is Calculated at the Low End of the Amplitude for Each Range and Should be Better with Increased Amplitude.

1. Bonded Strain-Gage-Type Pressure Transducer.
2. Sequential Sampling Millivolt-to-Digital Converter and Magnetic Tape Storage Data Acquisition System.
3. Resistance Shunt Based on the Standards Laboratory Determination of Transducer Sensitivity for Applied Pressure versus Resistance Shunt Equivalent Pressure Relationship.
4. Rotary Potentiometer Transducer.
5. In-Place Measurement of Physical Dimensions versus Transducer Output for Each Test.

Table 2. Configurations

1. Nozzle-Diffuser Spacing - Variable	2.88 to 3.88 in. for Phase I
Nozzle-Diffuser Spacing - Fixed	3.88 in. for Phase II
2. Two Diffuser Sizes	Large, 2.339-in. diam (101.5 in. Full Scale) Small, 2.23-in. diam (96 in. Full Scale)
3. Entrance Cone	On or Off
4. Aft Bulkhead Position	Fwd (Lip of Diffuser, No Entrance Cone) Aft (5.5 in. Aft of Entrance Cone Lip)
5. Pylon	On or Off
6. Nozzle Size	Std. (2.16-in. diam) with Pylon On Alt (2.14-in. diam) with Pylon Off
7. Expansion Cone	On or Off
8. Model Rotation	Four Radials (0 or 45, 90, 180, and 270 deg, Depending on Configuration)

Table 3. Test Conditions

Condition No.	Plenum Total Pressure, psia	Altitude, ft	Mach Number	Cell Pressure, psia	Primary Mass Flow, lb/sec	Venturi Pressure, psia
1	11	35K	0.86	3.42	0.88	< 275
2	12.3	25K	0.65	5.45	0.99	< 320
3	21.1	10K	0.36	10.10	1.69	< 530

Notes: Condition No. 1 Based on CF6 Test AB08-7 in Propulsion Test Cell J-2

Condition No. 2 Based on CF6 Test AB08-87 in Propulsion Test Cell J-2

Condition No. 3 Based on CF6 Test AC10-25 in Propulsion Test Cell J-2

Secondary Flow Fixed at Five Percent of Primary Flow Rate

Table 4. R1A1 Test Conditions and Configurations

Phase	Test Matrix Number	Flow Condition	Spacing, in.	Diffuser Size	Bulkhead Position	Secondary Flow, Percent	Entrance Cone	Pylon	Expansion Cone
I ↓	1	1	3.88	LARGE	AFT	5	ON	OFF	OFF
	2	3	3.88	↓	↓	↓	↓	↓	↓
	3	1	2.88	↓	↓	3	↓	↓	↓
	4	2	↓	↓	↓	↓	↓	↓	↓
	5	3	↓	↓	↓	↓	↓	↓	↓
	6	1	3.88	↓	FWD	5	OFF	↓	↓
	7	2	3.88	↓	↓	↓	↓	↓	↓
	8	1	3.88	SMALL	AFT	3	ON	↓	↓
	9	2	↓	↓	↓	↓	↓	↓	↓
	10	3	↓	↓	↓	↓	↓	↓	↓
	11	1	3.88	↓	FWD	↓	OFF	↓	↓
	12	2	↓	↓	↓	↓	↓	↓	↓
	13	3	↓	↓	↓	↓	↓	↓	↓
II ↓	14	1, 3	3.88	↓	AFT	5	ON	↓	ON
	15	↓	↓	↓	↓	↓	↓	↓	↓
	16	↓	↓	LARGE	↓	↓	↓	↓	↓
	17	↓	↓	↓	↓	↓	↓	ON	↓
	18	↓	4.78	↓	↓	↓	OFF	↓	↓

APPENDIX

It is possible, assuming that the axial cell wall pressure gradients can be directly imposed on the engine surface and by careful selection of the location of the cell reference static pressure measurement station, to eliminate or reduce the effect on engine performance caused by the axial cell wall pressure gradients. The adverse gradient on one side of the cell pressure station can be offset by the favorable gradient on the other side. This compensation leads to a technique involving the use of measured cell pressure gradients and component projected areas (cowling, pylon, etc.), along with careful selection of cell pressure measurement location, to correct measured engine surface static pressures and adjust measured in-cell net thrust for cell effects. This adjustment requires choosing the cell reference static pressure to ensure that the integral of the pressure gradient measured at the cell wall along the engine axis is zero. The thrust correction for the TF39 engine is given as

$$\Delta F = \int_A^B (P_{SO} - P_{SO}(x)) dA$$

where P_{SO} is the reference static pressure, and $P_{SO}(x)$ is the static pressure at any point along the engine cowl. If P_{SO} can be selected such that

$$\int_A^{1/2} (P_{SO}(X) - P_{SO}) dA = \int_{1/2}^B (P_{SO} - P_{SO}(X)) dA$$

where A and B represent the forward and aft extremes of the engine cowling, respectively, then the effect of the pressure gradient would be zero, since it will be accounted for by the other pressure-area terms in the thrust equation.